9-3-2013

Significance of nanosilica incorporation in type G oil well cement pastes

Andrew Griffin

SIGNIFICANCE OF NANOSILICA INCORPORATION IN TYPE G OIL WELL CEMENT PASTES

BY

ANDREW SETH GRIFIFN

B.S. CIVIL ENGINEERING

UNIVERSITY OF NEW MEXICO, 2010

THESIS

Submitted in Partial Fulfillment of the
Requirements for the Degree of

Master of Science

Civil Engineering

The University of New Mexico
Albuquerque, New Mexico

July, 2013

SIGNIFICANCE OF NANOSILICA INCORPORATION IN

TYPE G OIL WELL CEMENT PASTES

By

Andrew Seth Griffin

B.S., Civil Engineering, University of New Mexico, 2010

M.S., Civil Engineering, University of New Mexico, 2013

ABSTRACT

Emergent interest in advanced hydrocarbon exploration and geological carbon dioxide (CO_2) sequestration has brought about a requisite for improving existing oil well cementing materials and understanding the macro and microstructural characterization mechanisms of oil well cement (OWC). OWC slurries have stringent performance requirements, including low viscosity, rapid strength development, low permeability and enhanced degradation resistance. Preliminary research work showed that nanosilica is capable of reducing OWC porosity and therefore is was thought that nanosilica incorporation may have potential to improve the aforementioned performance requirements.

In this research, Type G OWC paste specimens produced with water to binder (*w/b*) ratio of 0.45 and incorporating 0, 1 and 3% nanosilica by weight of cement are hydrated for 28 days under two conditions, ambient room condition (20 ˚C with 0.1 MPa pressure) and an elevated oil well simulated condition (80 ˚C with 10 MPa pressure). Macroscale mechanical characterization of the hardened cement pastes was investigated

using axial compression, rapid chloride-ion penetration test (RCPT), and axial degradation/damage progression analysis and quantification after carbonic acid exposure testing. Degradation testing was performed by simulating conditions of geosequestration in a sandstone formation at a depth of roughly 1 km. These conditions were created by bubbling CO_2 into a heated vessel containing 0.5 M NaCl (brine) to produce the carbonic acid. This newly produced composition was then pumped into the bottom of a heated reactor containing the freshly cured specimens creating the sandstone formation condition exposure. This process was sustained for 28 days with subsequent monitoring of constant temperature (50 ˚C) and pH (5).

Slices of the cylindrical cement specimen were taken periodically, during and after 28 days of exposure, in order to quantify the OWC degradation progression. The compressive strength and modulus of elasticity of the specimens was examined prior, during and after exposure and damage metric was computed to quantify OWC degradation progress with time in a carbonated brine environment. The macroscale results showed that addition of 1% nanosilica can significantly limit OWC degradation in carbonated brine environments and enhance the accompanying performance requirements. Furthermore, microstructural characterization of the OWC specimens with and without nanosilica, before and after exposure, was performed using nanoindentation, the Brunauer-Emmett-Teller (BET) N2 theory and Barrett-Joyner-Halena (BJH) method, X-ray diffraction (XRD) analysis and ^{29}Si magnetic spinning angle (MAS) using nuclear magnetic resonance (NMR). Microstructural characterization experiments were performed in order to adequately explain the results of the macroscale experiments and reinforce the stated hypothesis.

DEDICATION

I dedicate this work to my family and fiancée. Thank you for all your encouragement, support and love. And to my Dad, who is no longer with me, thank you for instilling your discipline and perseverance toward excellence within me which made me the man that I am today. This pursuit would be meaningless without all of your love.

ACKNOWLEDGMENTS

First and foremost, I want to extend the upmost gratitude to my Master's thesis advisor and committee chair Dr. Mahmoud Reda Taha for his direction, reassurance, fortitude and confidence throughout this research and throughout my graduate program.

I would like to acknowledge the Defense Threat Reduction Agency (DTRA) for funding my assistantship and this research. This research would not be possible without the support.

I would also like to recognize my committee members Dr. Arup Maji and Dr. Muhammad Kalimur Rahman for their valuable comments and suggestions throughout my work as a graduate student.

A special thanks to my friend Dr. Jun Kim for his hard work and expertise, and to my friends Sherif Hassan Aboubakr, Sherif Dagash and Tony Campos for their help in all the Laboratory work and analysis, as well as their formatting guidance and wisdom.

Lastly, a very special thanks to my fiancée and my family who supported and encouraged me throughout my studies and my everyday struggles.

TABLE OF CONTENTS:

List of Figures ..... **ix**

List of Tables ..... **xiii**

Chapter 1 Introduction **1**

1.1 Motivation 1

1.2 Background 2

1.3 Scope of work 2

1.4 Thesis outline 3

Chapter 2 Literature Review **4**

2.1 Introduction 4

2.2 Nanotechnology in Cement 4

Chapter 3 Experimental Investigation **15**

3.1 Introduction 15

3.2 Materials 16

3.3 Experimental Methods 17

3.4 Uniaxial Compression 24

3.5 Rapid Chloride-Ion Penetration Testing (RCPT) 27

3.6 Degradation due to Carbonated Brine Exposure 30

3.7 Nanoindentation 37

3.8 Brunauer-Emmett-Teller (BET) N2 & Barrett-Joyner-Halenda (BJH) 43

3.9 X-Ray Diffraction Analysis (XRDA) Testing 47

3.9 Nuclear Magnetic Resonance (NMR) Testing 50

Chapter 4 Results and Discussion 56

4.1 Macroscale Characterization 56

4.2 Microstructural Characterization 69

Chapter 5 Recommendations & Conclusions 86

5.1 Summary 86

5.2 Conclusions 89

5.3 Recommendations 91

Appendix A – RCPT Analysis Matlab Code 92

Appendix B – Constants (Taylor 1987) 92

Appendix C – Isotherms & Corresponding BET Plots 93

References 99

List of Figures

Figure 1.1 Chevron Corp.'s Kern River oil field in Bakersfield, California 1

Figure 2.1 Feldman-Sereda model of C-S-H (cf. [Alizadeh, 2009]) 7

Figure 2.2 The globules like model of C-S-H by Jennings (cf.[Alizadeh, 2009]) 8

Figure 2.3 Connectivity of silicate tetrahedral showing Q_1 (single connectivity), Q_2 (dual connectivity) and Q_3 (triple connectivity) (triangles represent silicate tetrahedral) 8

Figure 2.4 DMA results showing the significance of C/S ratio on the modulus of elasticity of C-S-H [Alizadeh, 2009] 9

Figure 2.5 Sol-gel process by condensation explaining reversible and irreversible condensation and their significance to C-S-H 10

Figure 2.6 Description for interlayer water loss between case "a" and case "b" and its effect of the level of silicate polymerization [Alizadeh, 2009] 11

Figure 3.1 AEROSIL® 380 16

Figure 3.2 Standard paddle mixer 18

Figure 3.3 Flowability mold and table (side and plan view) 19

Figure 3.4 1% nanosilica incorporation 150% flow 20

Figure 3.5 3% nanosilica incorporation 34% flow 20

Figure 3.6 Fabricated specimen molds (1" diameter, 2" depth) 21

Figure 3.7 Hardened specimens after demolding 22

Figure 3.8 Elevated curing reactor set-up 23

Figure 3.9 Pressure vessel close-up and schematic 23

Figure 3.10 Cylindrical specimens top end preparation 24

Figure 3.11 Uniaxial compression test system set-up 25

Figure 3.12 RCPT specimen mounted in testing cells 28

Figure 3.13 RCPT complete system setup 29

Figure 3.14 Degradation testing specimen conditioning setup 31
Figure 3.15 Degradation testing conditioning chamber open 31
Figure 3.16 Schematic of set-up and flow through degradation testing system 32
Figure 3.17 Degradation testing set-up (left) reactor set-up (right) 33
Figure 3.18 Degradation testing setup 34
Figure 3.19 Specimens after degradation testing side view (left) top view (right) 35
Figure 3.20 Example of slices taken for degradation progression determination 36
Figure 3.21 Example of degradation progression and measurement taken 36
Figure 3.22 Polishing apparatus for preparation on nanoindentation samples 37
Figure 3.23 (a) Nanoindentation components and (b) loading and unloading during nanoindentation to extract elastic behavior 38
Figure 3.24 Hardened porcelain mortar and pestle (left) prepared fine powder (right) ... 43
Figure 3.25 BET N2 physisorption testing system 44
Figure 3.26 Description of XRD technique using Bragg's law 47
Figure 3.27 Rigaku SmartLab XRD testing system 48
Figure 3.28 Cryomagnet for NMR spectroscopy 51
Figure 4.1 Uniaxial compressive strength comparisons (ambient curing) 56
Figure 4.2 Uniaxial compressive strength comparisons (elevated curing) 57
Figure 4.3 Axial stress-axial strain relationships for each specimen type 58
Figure 4.4 Axial stress-axial strain relationships (ambient curing) 59
Figure 4.5 Axial stress-axial strain relationships (elevated curing) 59
Figure 4.6 Static modulus of elasticity comparison (ambient curing) 60
Figure 4.7 Static modulus of elasticity comparison (elevated curing) 60
Figure 4.8 Current versus time for each specimen type 62

Figure 4.9 Charge passing per specimen type 63

Figure 4.10 Uniaxial compressive strengths after degradation testing 64

Figure 4.11 Uniaxial compressive strengths before and after degradation testing 64

Figure 4.12 Stress-strain curves after degradation 65

Figure 4.13 Static modulus of elasticity comparison before and after degradation 66

Figure 4.14 Degradation progression comparisons 67

Figure 4.15 Degradation progression for the specimen types 68

Figure 4.16 Loading-indentation depth of cement paste showing creep during dwell period. Experiments showing kinking at intermediate loading (0.18 mN) which can be used to determine the toughness of cement paste [Reinhart et al., 2010] 69

Figure 4.17 Nitrogen adsorption/desorption isotherm neat specimen type (ambient curing) 72

Figure 4.18 BET N2 plot neat specimen type (ambient curing) 72

Figure 4.19 Calculated specific surface area for each specimen type 73

Figure 4.20 Pore size distribution for each specimen type 74

Figure 4.21 Comparison of XRD Spectra of the Hardened Cement Pastes Incorporating 0%, 1% and 3% Nanosilica (Ambient Curing) 76

Figure 4.22 Comparison of XRD Spectra of the Hardened Cement Pastes Incorporating 1% and 3% Nanosilica (Ambient Curing) 77

Figure 4.23 Comparison of XRD Spectra of the Hardened Cement Pastes Incorporating 0%, 1% and 3% Nanosilica (Elevated Curing) 77

Figure 4.24 Comparison of XRD Spectra of the Hardened Cement Pastes Incorporating 1% and 3% Nanosilica (Elevated Curing) 78

Figure 4.25 Effects of Curing Conditions on Microstructural Compositions by XRD Spectra of the Hardened Cement Pastes without Nanosilica 79

Figure 4.26 Effects of Curing Conditions on Microstructural Compositions by XRD Spectra of the Hardened Cement Pastes Incorporating 1% Nanosilica 80

Figure 4.27 Effects of Curing Conditions on Microstructural Compositions by XRD Spectra of the Hardened Cement Pastes Incorporating 3% Nanosilica 80

Figure 4.28 XRDA of OWC specimens after carbonated brine exposure 81

Figure 4.29 ^{29}Si MAS NMR spectra of hardened cement without nanosilica and incorporating 1 % and 3 % nanosilica cured under (a) ambient curing conditions and (b) elevated curing conditions 82

Figure 4.30 Comparison of NMR spectra before and after carbonated brine exposure for OWC specimens (a) G0%N vs. G0%H (b) G1%H and G3%H..... 84

List of Tables

Table 3.1 Exact mixing proportions..... 17

Table 4.1 Microstructural phase fractions from deconvolution on nanoindentation results 70

Table 4.2 Integration of Q^n intensities by deconvolution of ^{29}Si MAS NMR 83

Chapter 1 Introduction

1.1 Motivation

The 2010 fracture of oil wells in the Gulf of Mexico and the ecological impact coupled with the loss of billions of gallons of oil compels research to produce dependable and sustainable cementing materials for oil well operations. Manufacturing sustainable oil wells is a foremost concern for countries with vast oil production like the Kingdom of Saudi Arabia (KSA). The KSA has 267 billion barrels of confirmed oil reserves with 100 major oil and gas fields comprising of over 1500 active oil wells [Kim et al., 2011]. Most of these reserves are relatively deep and sustain elevated temperatures and pressure. The KSA also has the fourth largest global gas reserves of 253 trillion cubic feet. In 2008, crude oil production capability in Saudi Arabia was approximately 11 million barrels/day, and was projected to increase to around 12.5 million barrels/day by the year 2009. Throughout 2008, 87 wells were drilled and Saudi Aramco intended to invest $60 billion in oil and gas projects over the next five years. Several other countries are also beginning to invest in and produce unprecedented amounts of oil output, as seen domestically with production at the highest levels in 15 years. This research was motivated by collaborative research initiated by King Fahd University of Petroleum and Minerals (KFUPM, Saudi Arabia) on identifying the significance of nano silica on the behavior of oil well cement in oil wells. This research collaboration between UNM and KFUPM examines the different aspects of using nanosilica in oil well cementing.

Figure 1.1 Chevron Corp.'s Kern River oil field in Bakersfield, California

1.2 Background

In oil and gas well drilling operations, oil well cement (OWC) slurry is incorporated to assist in the drilling procedure and ultimately becomes the cementing material of the well casing. The composite material formed is responsible for preventing a multitude of unwanted affects which can severely influence the production process. Therefore, demanding performance requirements are imposed on cement slurries used for oil well cementing including, low viscosity, early strength development, low permeability and superior resistance to attack from aggressive fluids. An abundance of current research has been focused on modifying OWC slurries to better comply with the stringent performance requirements [Jupe et al. 2005; Janson, et al. 2007; Lal, et al. 2009], however, only limited results are presented in closed domains. In the past decade, numerous patents have been filed in the region of innovative materials for oil well cementing.

1.3 Scope of work

In this research, macroscale and microstructural experimentation was conducted in order to examine the significance of nanosilica incorporation in Type G OWC pastes. OWC pastes with water to binder ratio (*w/b*) of 0.45 with and without the incorporation of nanosilica contents of 1% and 3% are hydrated for 28 days under two curing conditions: normal room curing conditions of 20 ˚C and 0.1 MPa pressure and elevated oil well simulated curing conditions of 80 ˚C with 10 MPa pressure. Type G OWC was used in this study because it is a common cementing material capable of being implemented from the surface of the oil well bore head all the way down to a depth approximately 2440 m, over a wide range of temperatures and pressures. Investigation of this type of cement becomes important as hydrocarbon exploration reaches greater and greater depths. This is also the type of OWC typically used domestically.

The macroscale mechanical characterization of the hardened cement pastes was investigated using axial compression, rapid chloride-ion penetration test (RCPT), nanoindentation and axial degradation/damage progression analysis and quantification

after exposure to carbonated brine solutions. The above experiments were followed by a series of microstructural characterization tests conducted at the nano/micro-scale. The tests include nanoindentation, specific surface area/pore size distribution analysis using the Brunauer-Emmett-Teller (BET) N2 theory and Barrett-Joyner-Halena (BJH) method, X-ray diffraction (XRD) analysis and ^{29}Si magnetic spinning angle (MAS) using nuclear magnetic resonance (NMR). Microstructural characterization was conducted before and after degradation.

1.4 Thesis outline

Chapter 2 contains a complete literature review that first introduces the areas of interest and subsequently describes the methods and philosophies developed by researchers dealing with nanotechnology incorporation in cement. The fundamental components of the nano and microstructure of cement were also explored in order to provide a comprehensive review on the advancements of OWC incorporating nanotechnology. The experimental methods and procedures from the laboratory experiments that were conducted throughout this research are fully described in Chapter 3. Chapter 4 displays the results from experimentation and uses the nano/microstructural characterization to adequately explain and link together the mechanical behavior attained from macro experimentation. Chapter 5 presents a summary and conclusion of the results and recommends future work to further develop oil well cementing materials.

Chapter 2 Literature Review

2.1 Introduction

Advancements in nanotechnology over the past decade have broken ground for development of innovative material compositions that can significantly enhance properties of concrete and cementitious materials. Nanotechnology is the synthesis, manipulation and utilization of materials, devices, and systems through the control of matter on the nanometer-length scale, that is, at the level of a few atoms or molecular structures [Bhushan, 2007]. The quintessence of nanotechnology is the ability to utilize this length scale to manufacture advanced material compositions with fundamentally enhanced microstructures. These "nanostructures" fashioned from understood early principles, are the smallest synthetic objects, and they exhibit novel physical, chemical and biological properties and phenomena [Roco & Alivisatos, 1999].

Carbon capture and storage (CCS) is an international effort that targets reducing carbon dioxide (CO_2) in the atmosphere by capturing and storing it in deep geological formations [Cailly et al., 2005]. A major concern in the CO_2 sequestration process is to ensure the integrity of existing oil wells and to confirm their ability to confine CO_2 storage. It is well accepted that wellbore integrity is strongly dependent on the quality of the OWC in the annulus and the quality of the bond between this annulus and the rock formation on one side and between the annulus and the steel casing on the other side.

2.2 Nanotechnology in Cement

Nanotechnology has progressively gained recognition, over the past few years, and is presently being implemented in many fields including biomedical, electronic instruments, sensors and nano-modified materials. Beginning in the early 1990s nanotechnology started to gain recognition as a promising evolving technology by various industrial sectors. More recently, efforts have progressed toward utilizing nano-scale integration for the development of innovative material compositions [Bhushan, 2007]. Currently, nanotechnology is established and accepted in numerous areas of science and is rapidly evolving into applications in applied sciences, technological

advancements, most areas of engineering and several applications in material development and construction [Zhu et al., 2004]. In cement composition technology, initial nanotechnology incorporation efforts were focused on understanding the essential phenomena of cement hydration, pore structure and cement degradation mechanisms [Scrivener & Kirkpatrick, 2008]. An abundance of research on nano-modified cements and cements with carbon nano tubes, self-healing cement and other nano-based cementitious materials has been in progress over the last decade [Chaipanich et al., 2010]. Furthermore, nano-characterization of mechanical properties of materials using various techniques has progressively evolved into a significant tool for providing quantitative evaluations of nanomaterial compositions [Ulm et al., 2007]

It has been established by numerous investigations that traditional cement based materials show profoundly enhanced properties when engineered at the nanoscale [Sanchez & Sobolev, 2010]. Nanoparticles such as TiO_2, Z_nO_2, fullerenes, carbon nanotubes, silica, alumina, magnesium, calcium and clays have been examined to improve the strength, stiffness and ductility characteristics of cementitious materials [Li et al., 2006]. These nanoparticles augment the microstructure of cement during the hydration process and fill pore voids to increase strength. Research has shown that the very high surface area of nanoparticles (e.g. nanosilica) plays significance in the augmented hydration chemistry of the material. Research has also shown that nano-Fe_2O_3 exhibits a self-sensing strain capability which can be particularly advantageous in structural health monitoring [Norris et al., 2008].

The 2010 fracture of oil wells in the Gulf of Mexico and the ecological impact coupled with the loss of billions of gallons of oil compels research towards certain areas. In particular the significance of curing regimes, including high pressure and temperature on the microstructure of cement hydration products and the influence of that microstructure on mechanical and fracture resistance of cement. Therefore, there is a major focus on calcium-silicate-hydrate (C-S-H), the major cement hydration product that makes up approximately 67% of hydrated Portland cement paste [Diamond, 1976]. The importance of nanotechnology in OWC slurry originates from the eminent fact that the C-S-H gel consists of nano-structured colloidal layers [Taylor, 1993; Richardson,

1999]. The incorporation of nanoparticles as an enhancement method for OWC slurry is currently a major topic of interest that has yet to be fully explored. Current research has demonstrated that significant potential exists in the development of the mechanical characteristics of cement pastes integrating nanosilica, nanoalumina and carbon nanotubes [Kuo et al., 2006; Li et al. 2006].

In order to provide a comprehensive review on the advancements on OWC technology incorporating nanotechnology to modify cement hydration, it is important to first understand the foremost components of cement nano and microstructure. A complete depiction of cement hydration can be found in major textbooks [Taylor, 1997; Mehta & Monteiro, 2006]. Essentially, the hydration of cement represents the reaction of the four major components in the clinker: C_3S, C_2S, C_3A and C_4AF with water and forming the main hydration products C-S-H gel, calcium hydroxide ($Ca(OH)_2$) also known as Portlandite or CH, calcium sulfoaluminates hydrates (C_4ASH_{18}) known as ettringite forming needle-shaped prismatic crystals which transforms later to monosulfate hydrate (C_4ASH_{18}) of hexagonal plate crystals [Neville 1995; Mehta & Monteiro, 2006]. As mentioned earlier, C-S-H is acknowledged as the foremost hydration product making up approximately 67% of the hydrated Portland cement paste [Diamond, 1976] and consequently it accountable for most of the strength and fracture characteristics of hydrated cement. Furthermore, most of the time-dependent properties of hydrated cement, such as creep, are understood to be controlled by the microstructure of C-S-H [Larbi, 1993; Jennings & Tennis, 1994].

The majority of the scanning electron microscope (SEM) investigations depicted C-S-H to be an amorphous material. This observation is connected to C-S-H formed under ambient pressure and temperature [Jennings, 2000]. C-S-H formed under high pressure and temperature curing is usually moderately crystalline. However, most investigations concluded that C-S-H is a material with a layered composition [Thomas et al., 1998; Allen et al., 2007]. Initial models of the structure of C-S-H include the recognized Feldman-Sereda model [Feldman & Sereda, 1968] which is commonly accepted model capable of explaining the role of water in time-dependent behavior of hydrated cement paste. The Feldman-Sereda model is shown in Figure 2.1.

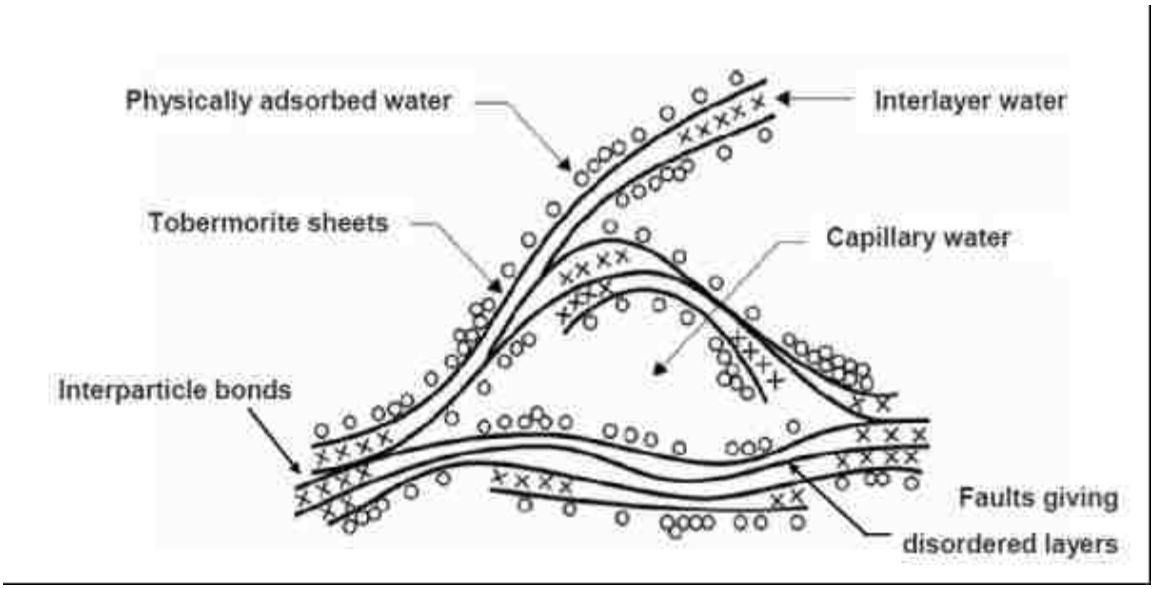

Figure 2.1 Feldman-Sereda model of C-S-H (cf. [Alizadeh, 2009])

Recently, the globules like model developed by Jennings and Thomas [Thomas & Jennings, 2006] has been proposed to describe the physical and chemical nature of C-S-H. Although the Jennings' model was criticized for the inability to characterize the observed fibrous nature of C-S-H, it is well recognized for its ability to describe the process of gel condensation and the significance of drying on cement behavior as described in the figure below [Thomas & Jennings, 2006]. The globules like model is shown in Figure 2.2.

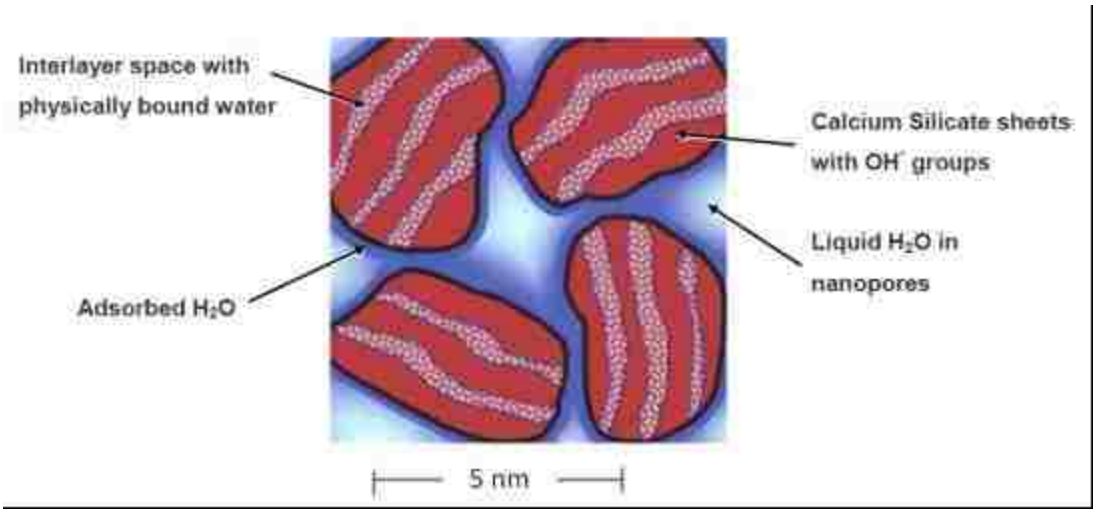

Figure 2.2 The globules like model of C-S-H by Jennings (cf.[Alizadeh, 2009])

The most essential nanostructure feature of C-S-H, that might have profound effects on the mechanical properties, is silicate polymerization in C-S-H. Silicate polymerization is a term used to describe the number of bonds generated by the silicate tetrahedron as shown in Figure 2.3. A silicate tetrahedron having the number of *n* sharing oxygen atoms is expressed as Q^n, where *n* is the number of sharing oxygen atoms up to 4. The description of silicate tetrahedra having various sharing oxygen atoms is shown in Figure 2.3.

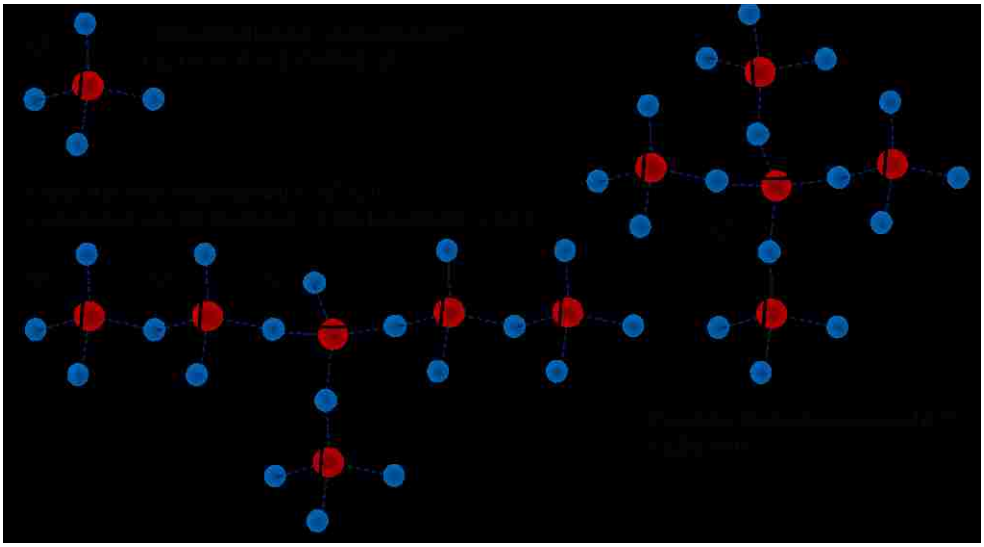

Figure 2.3 Connectivity of silicate tetrahedral showing Q_1 (single connectivity), Q_2 (dual connectivity) and Q_3 (triple connectivity) (triangles represent silicate tetrahedral)

As The Q^0 connection is typically detected in hydrated cement due to the residual tricalcium silicate (C_3S) and dicalcium silicate (C_2S). The Q^1 (end-chain group), Q^2 and Q^3 (middle-chain group) in silicate are normally observed due to the layered structure of C-S-H. The Q^4 connection is representative of the polymerization of quartz and can be detected in silica rich products such as fly ash, silica fume and nanosilica. Silicate polymerization intensifies as the C/S ratio decreases [Taylor, 1986]. A large level of silicate polymerization indicates long mean silicate chain length, an increased distance between the C-S-H layers and more BET surface area [Lea, 1970; Taylor, 1997; Garbev et al., 2007]. A high degree of silicate polymerization in synthetic C-S-H can be developed by increasing hydration temperature [Hirljac et al., 1983], drying [Bentur et al., 1979] and by compaction [Alizadeh et al., 2011]. Fundamentally a high degree of silicate polymerization correlates with an increased stiffness of C-S-H, however this does not hold true for all calcium to silicate (C/S) ratios. Recent investigations have exhibited a decreased modulus of elasticity of C-S-H from C/S ratio of 0.6 to 1.2 and then an increase at C/S ratio of 1.5 as shown in Figure 2.4 [Alizadeh et al., 2011].

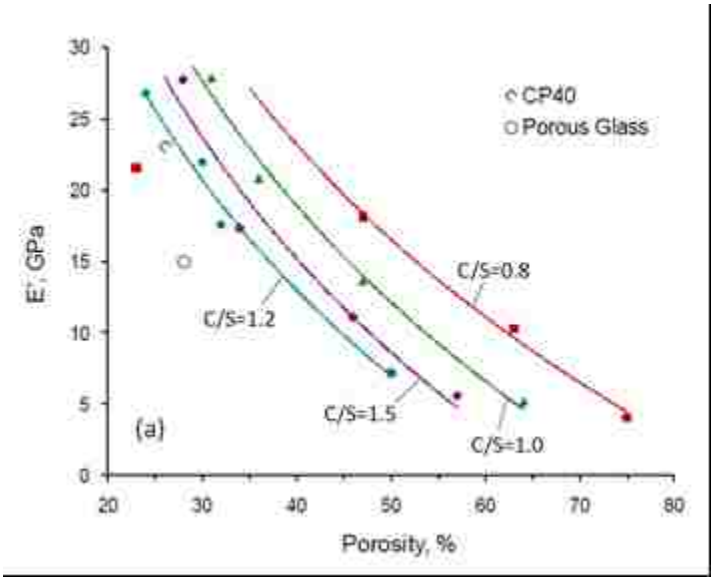

Figure 2.4 DMA results showing the significance of C/S ratio on the modulus of elasticity of C-S-H [Alizadeh, 2009]

Additionally, drying was shown to intensify C-S-H polymerization, but was also shown to decrease it stiffness. These fundamental inconsistencies between the polymerization and mechanical characteristic correlation can be attributed to the fact that the polymerization process does not exclusively control the final C-S-H characteristics due to the colloidal nature of C-S-H [Thomas & Jennings, 2006]. Research has linked most mechanical properties of C-S-H to the characteristics of layered minerals such as jennite and tobermorite, it is apparent that the colloidal nature of C-S-H makes it a unique material. The colloidal properties (gel-like) of cement paste have been accepted since the 1950s [Powers & Brownyard, 1948] Thomas and Jennings [Thomas & Jennings, 2006] generated a colloidal model of the C-S-H in cement paste to explain creep and shrinkage of hardened cement using the *'sol-gel'* process. The important response of the sole-gel process, known as *"condensation"*, is to link hydrolyzed molecules together by liberating a water molecule [Brinker & Scherer, 1990]. Condensation can be divided into reversible and irreversible components as shown in Figure 2.5.

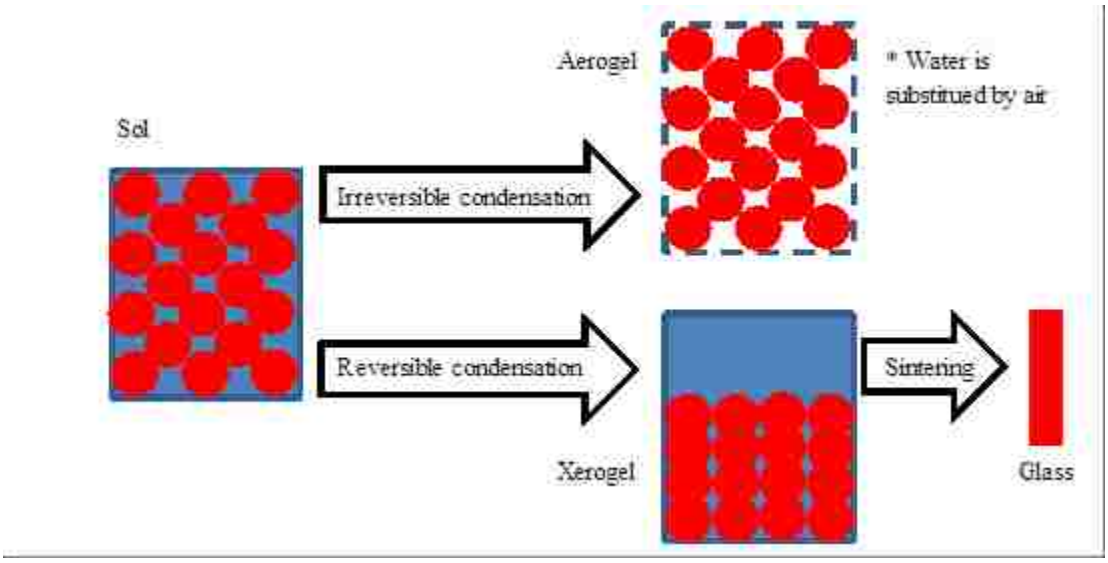

Figure 2.5 Sol-gel process by condensation explaining reversible and irreversible condensation and their significance to C-S-H

The irreversible components of condensation are comparative to a sol-gel process of *'aerogel'* in colloid science while the reversible mechanisms are comparative to the sol-gel process of *'xerogel'*. After water is removed from a sol under supercritical conditions, the resultant colloidal system does not shrink and a material with large pore size distribution in created. This highly porous composition is recognized as an aerogel. Material produced from the xerogel process is a homogeneous product fashioned by drying sol with unobstructed shrinkage (e.g. silica gel). Sintering of a xerogel transforms the silica gel into a dense glass. Aerogel-like C-S-H can be observed when cement is hydrated at elevated temperatures.

The new C-S-H composition contains comparatively large capillary pores and in turn a decreased strength of cement [Thomas & Jennings, 2006]. The layered mineral tobermorite found in cement hydrated with silica rich additives at elevated pressures and temperatures [Saoûta et al., 2006] might be considered as a sintered xerogel-like C-S-H. Taking this into account, pressure and temperature may play a significant part in the morphology of C-S-H. Interlayer water loss on the nanostructure of C-S-H has also been proposed to have significance by numerous researchers. It is consequently essential to take into account the colloidal nature of C-S-H and the polymerization aspect of silicate as dependent components of C-S-H. The silicate polymerization and colloidal nature of C-S-H are two important singularities that dictate the performance of C-S-H. The significance of interlayer water loss on the nanostructure of C-S-H is shown in Figure 2.6.

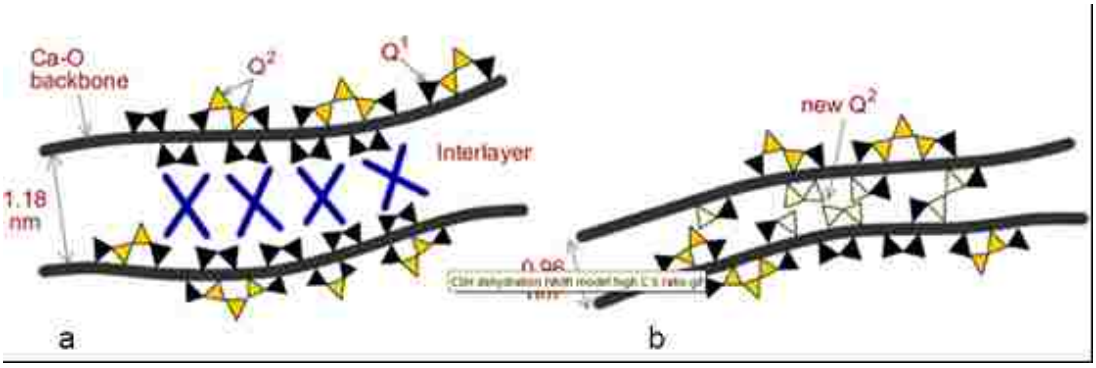

Figure 2.6 Description for interlayer water loss between case "a" and case "b" and its effect of the level of silicate polymerization [Alizadeh, 2009]

As demonstrated above, C-S-H is a complex and unique material. This feature has led to continuous exploration in C-S-H research and modeling. Beaudoin and Feldman first synthesized C-S-H by producing aqueous solutions of sodium metasilicate and calcium oxide at various ratios [Beaudoin & Feldman, 1986]. Six samples were produced with C/S ratios extending between 0.68 and 1.49. The samples were then dried in an acetone and ether bath followed by being subjected to a stream of nitrogen for 4 days. Subsequently, the samples were placed in a nitrogen exposure environment for 1 day. The produced C-S-H was then compacted into discs of diameter 31.8 mm and thickness of around 1.27 mm using pressures ranging from 510 MPa to 1360 MPa. The densities of the samples were particularly equivalent due to the moderately high compaction pressures. Deflection at the midpoint of the C-S-H discs, fixed at three points, was measured in order to acquire the modulus of elasticity of the specimens. Atkins et al. [Atkins et al., 1992] similarly produced C-S-H by combining calcium oxide with either silica fume or silica acid along with distilled water. Samples were produced with C/S rations ranging between 0.9 and 1.7. The samples were then repeatedly filtered and re-dispersed to eliminate impurities. Finally, the samples cured under saturated $CaCl_2$ to a relative humidity of 30%. In this study, the solubility of the C-S-H phase was examined and no mechanical characterization was implemented.

Occurring more recently, Sugiyama [Sugiyama, 2008] produced C-S-H at varying C/S ratios of 0.65, 0.83, 0.9, 1.1, and 1.2 [Sugiyama, 2008]. The C-S-H samples were composed of calcium oxide and amorphous silica mixed with distilled water. The specimens were then hydrated for 7 days and dried in a vacuum chamber over silica gel. The durability of the C-S-H specimens against leaching in sodium chloride was measured. The loss of calcium from the C-S-H was determined from chemical analysis and once again no mechanical characterization testing was implemented. However, Alizadeh and Beaudoin [Alizadah & Beaudoin, 2011] performed mechanical characterization testing of synthetic C-S-H with a variable C/S ratio. Testing was performed using dynamic loading of compacted beam like specimens.

The research described above concentrates on the fundamental characteristics of C-S-H. An abundance of recent has also examined the C-S-H structure and interacting

factors in OWC slurries [Jupe et al., 2005; Jansson et al., 2007; Lal et al., 2009]. Type G OWC cured under 20 ˚C and 0.1 MPa or 80 ˚C and 7 MPa for around a year was examined in order to characterize the chemical composition and structure [Saoût et al., 2006a]. The implication of chemical composition and structure on chemical shrinkage and gas migration of OWC was also investigated in past research [Justens et al., 1995]. The research revealed that the mono-sulfate (ettringite phase) is transformed into Friedel's salt as the chloride ions replace the sulfate particles after a year of 20˚C and 0.1 MPa exposure. Under elevated curing conditions the study showed that the portlandite (CH) dissipates entirely. The study also reported a development of calcite, with a Mohs hardness of 3, and a higher level of polymerization in the C-S-H. Another report showed that Type H OWC did not significantly degrade due to CO_2 infiltration after a year of exposure and elevated oil well simulated curing conditions [Kutchko et al., 2008]. The elevated curing conditions of 80˚C and 7 MPa transformed the ettringite phase of OWC to hydrogrossular, with a Mohs hardness of 7. Low permeability Type G OWC, which includes added silica, experienced amplified pozzolanic reactivity under the elevated curing conditions [Saoût et al., 2006b]. The C-S-H mineral tobermorite, Mohs hardness 2.5, which has a middle chain group (Q^2) and diverging (Q^3) of silicate tetrahedron, was found in specimens cured under elevated oil well simulated conditions. The incorporation of silica into Type H OWC was investigated with a focus on the crystallization of C-S-H using several silica rich materials such as silica fume, silica flour and a silica fume and zeolite combination. [Meller et al., 2007] proposed that a mixture of alumina and silica nanoparticles incorporated into OWC could produce geothermal well sealant capabilities when exposed to oil well conditions.

Many researchers have conducted experiments to simulate OWC degradation due to exposure to saturated carbonated brine (e.g. Huet et al. 2010 and Duguid and Scherer 2009). Zhang and Bachu (2011) explained that the process of carbonation might not be harmful to OWC. While carbonation means the reaction of CO_2 with Calcium Hydroxyl (CH) in hydrated cement, this results in the formation of $CaCO_3$ (Calcite) which might fill the pores of cement and reduce its porosity and thus increase its integrity. Carbonation in and of itself, therefore, is argued not to be dangerous to the quality of

OWC. However, CO_2 bicarbonation, which results in dissolving $CaCO_3$ from cement and leaching out of the cement, is a dangerous mechanism that can significantly affect OWC integrity. This difference was confirmed by field measurements by Crow et al. (2010). The differentiation of these two steps in the degradation process is important. Bicarbonation is dependent on the chemistry of the environment which is strongly dependent on the nature of the rock formation. Degradation testing was implemented here to quantify the specimen's resistance to attack from carbonated brine formed during carbon sequestration following the set-up developed by Duguid and Scherer (2009) with some modifications. This system was designed to simulate the characteristics of geosequestration conditions at a depth a 1 km below ground level (Hitchon 1996). The system simulates sandstone-like conditions of 50 °C and pH 5 at the same depth.

Chapter 3 Experimental Investigation

3.1 Introduction

This chapter defines the macro and nano-microscale experimentation performed for this research. The chapter begins by particularizing the materials used in the OWC paste compositions. Then a depiction of the imperative curing conditions and precise sample preparation is given. Subsequently, a description of each of the performed experiments is presented. On the macroscale, the experiments included axial compression, rapid chloride-ion penetration test (RCPT), nanoindentation and axial degradation/damage progression analysis and quantification after carbonic acid exposure testing. The above experiments were followed by a series of microstructural characterization tests conducted at the nano/micro-scale. The tests include nanoindentation, specific surface area/pore size distribution analysis using the Brunauer-Emmett-Teller (BET) N2 theory and Barrett-Joyner-Halena (BJH) method, X-ray diffraction (XRD) analysis and ^{29}Si magnetic spinning angle (MAS) using nuclear magnetic resonance (NMR). Microstructural characterization was conducted before and after degradation.

Macroscale experiments were executed in order to test the hypothesis that incorporation of nanosilica in OWC pastes results in significantly improving the aforementioned performance requirements of OWC. This includes low viscosity, rapid strength development, low permeability, and enhanced resistance to aggressive fluids such as carbonic acid created during carbon sequestration.

Microstructural characterization experiments were also performed in order to adequately explain the results of the macroscale experiments and reinforce the stated hypothesis.

3.2 Materials

For all OWC paste mixes produced for experimentation, Type G OWC (API Class G) was used as the cementitious material. This material was acquired from the manufacturer and is obtained by grinding clinker, consisting essentially of hydraulic calcium silicates, usually containing one or more forms of calcium sulfate as an interground additive [API, 2009]. Class G OWC is intended for use as a basic well cement and is available in moderate sulfate-resistant (MSR) and high sulfate-resistant (HSR) grades. The nanosilica used is AEREOSIL® 380 from manufacturer Evonik Degussa Products, which is hydrophilic fumed silica with an average BET surface area of 380 m^2/g and an average particle diameter of 7 nm. AEROSIL® 380 is a chemically prepared silicon dioxide powder that is white in color and odorless, and has a melting point of 1700℃ and a density of 2.2 g/cm^3. Only deionized water was used during the mixing process to ensure consistency of results and to prevent potential contamination from tap water.

Figure 3.1 AEROSIL® 380

3.3 Experimental Methods

3.3.1 Mixing Proportions

Water to binder ratio (*w/b*) of 0.45 was used for the neat and nanosilica incorporated OWC paste specimens. The binder weight is the sum of the cement and incorporated nanosilica. Mixing quantities were determined from Table 5 of the American Petroleum Institute's (API) Specification 10A for Cements and Materials for Well Cementing [API, 2009]. This table shows the slurry requirements for Class G OWC as 349±5 g of deionized mixing water and 792±5 g of OWC. Nanosilica was incorporated at levels of 1% and 3% by mass of binder. These incorporation percentages were chosen based on prior research and literature. The exact mixing proportions are presented in Table 3.1. The binder weight was held constant for each mix design in order to maintain the focus of the investigation, which is examining the effects of nanosilica incorporation.

Table 3.1 Exact mixing proportions

Batch	Deionized Water (g)	Type G Cement (g)	Nanosilica (g)	Total Binder (g)
Type G0%	354	790	0	790
Type G1%	354	782.1	7.9	790
Type G3%	354	766.3	23.7	790

3.3.2 Mixing Procedure

A customized combination of ASTM and API standards were used to produce the hydraulic OWC specimens [ASTM, International 2005 & API, 2009]. This modified method produced the best hardened cement samples during trial batching therefore it was further implemented. All mixes were mixed according to these specific procedures in a standard paddle mixer (Figure 3.2). This procedure included:

1. Measuring the temperature of the mix water and the cement 60 seconds prior to mixing to ensure the API standard of 23˚C ± 1˚C
2. Mixing of all dry materials at a rate of 140 ± 5 r/min for 30 seconds to incorporate cement and nanosilica together where applicable
3. Placing the mix water to the bottom of a clean mixing bowl
4. Adding the dry materials to the mix water and allowing 30 seconds for absorption
5. Mixing the combination for 30 seconds at a rate of 140 ± 5 r/min
6. Stopping the mixer for 15 seconds while scraping down the sides of the bowl
7. Final mixing at a speed of 285 ± 5 r/min for a minimum of 1 minute until slurry is incorporated

   *** Total mixing time of approximately 4 minutes*

Figure 3.2 Standard paddle mixer

3.3.3 Fresh Properties

Some fresh properties such as, temperature and pH were measured for all of the freshly batched cement paste slurries. Nanosilica incorporation proved to have no significant effects on the slurries temperature and alkalinity. The flowability of the fresh slurries was then examined using ASTM C1437 Standard Test Method for Flow of Hydraulic Cement [ASTM, International 2005]. The neat slurries flowed off of the flow table immediately after the mold was removed, which indicates 150% flow before the start of the test. The slurries with a 1% addition of nanosilica reached the range of the flow table after seven taps, which also indicates 150% flow (Figure 3.4). Slurries with a 3% addition of nanosilica had a flow of only 34% (Figure 3.5).

Figure 3.3 Flowability mold and table (side and plan view)

Figure 3.4 1% nanosilica incorporation 150% flow

Figure 3.5 3% nanosilica incorporation 34% flow

3.3.4 Specimens and Specimen Preparation

Special molds were fabricated out of hardened plastic to cast 25.4 mm diameter, 50.8 mm tall cylinders. Each mold breaks down into 4 pieces and is capable of making 5 specimens at a time (Figure 3.6). The uncommon specimen size was selected in order to accommodate the restrictive dimensions of the high pressure and temperature curing chamber described in the next section. After completing the mixing procedures, the incorporated slurries were placed into a pastry bag that was then placed under a vacuum desiccator for 5 minutes to remove the air voids. The mold was lightly coated with a release agent and the base plate placed on the bench. The molds were then filled half of the way full to a depth of approximately 1 inch using the pastry bag. A puddling rod with a 3 mm diameter was then used to puddle the slurry in an evenly distributed pattern, 27 times per specimen in accordance with API 10A. The remaining slurry inside of the pastry bag was then stirred with a rubber spatula, in order to minimize segregation, and piped overflowing into the remaining mold depth. The puddling rod process of the previous layer was repeated and a straight edge used to strike off the excess slurry level at the top of the molds. The top cover plate was then placed on top of the mold and the bolts were placed through the holes in the bottom and top plates. The nuts were then placed on the bolts and tightened to a suitable torque to ensure no mold leakage (Figure 3.6). Molds were left in the lab for 24 hours in order to harden. After this initial curing period the hardened specimens were demolded and prepared for the appropriate curing condition.

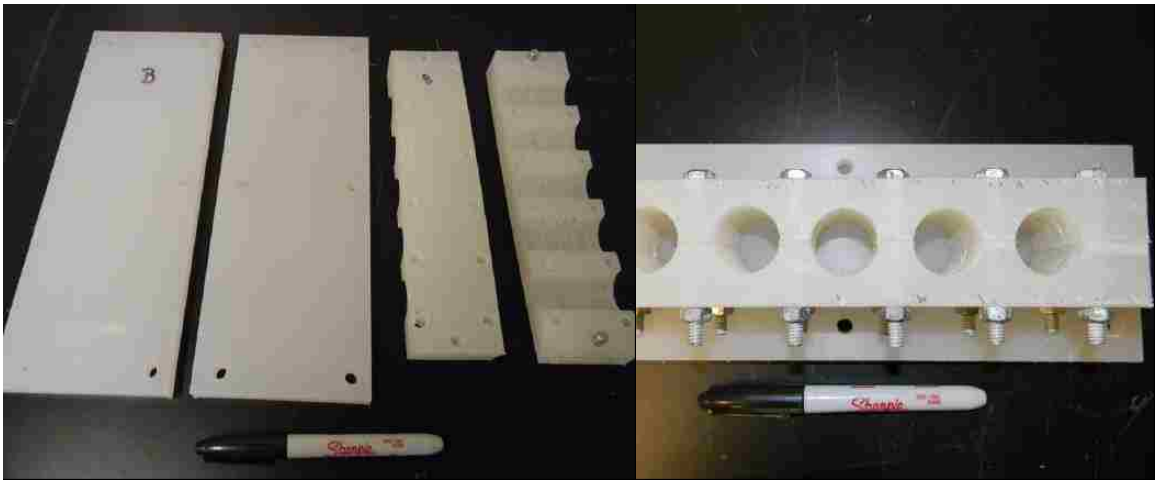

Figure 3.6 Fabricated specimen molds (1” diameter, 2” depth)

Figure 3.7 Hardened specimens after demolding

3.3.5 Curing Set-up

Specimens were cured in a curing room under tap water containing lime with a controlled temperature of 20 ˚C and pressure of 0.1 MPa (1 atm) for ambient curing conditions, while a special set-up for the elevated temperature 80 ˚C and pressure 10 MPa (98.7 atm) curing conditions was prepared as shown in Figure 3.8. The special setup and process were created to simulate an actual OWC curing condition. An enlarged 900 mL pressure vessel was fabricated, using the seating dimensions of the Parr® 450 mL pressure vessel, in order to allow for curing of up to 9 specimens at a time. The vessel was filled with enough tap water to cover the top layer of specimens. 5 grams of lime was added to the curing water in the reactor to prevent leaching of lime from the specimens during the curing process. The pressure flange was applied and tightened onto the vessel and the vessel was placed into the heater base and mount. The pressure line from the compressed nitrogen gas was connected and a pressure of 10 MPa was applied. After assuring that there were no leaks by inspection the heating control was turned on and set to a temperature of 80 ˚C. Monitoring of the pressure in the vessel was required for the first half hour as the increasing temperature also increased the pressure. This was fixed by releasing pressure though the release valve until the temperature stabilized to 80 ˚C. The temperature inside the vessel was measured by thermal couple sensors and digital readout. All specimens were cured under ambient or elevated curing conditions for 28 days with subsequent monitoring of the temperature and pressure.

Figure 3.8 Elevated curing reactor set-up

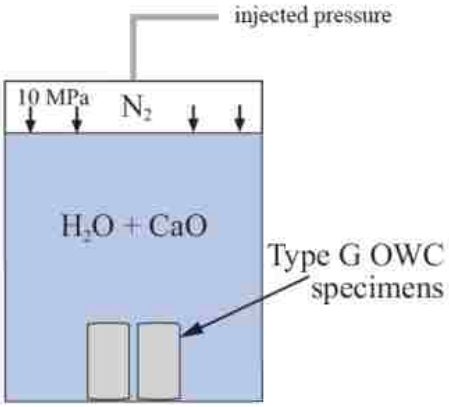

Figure 3.9 Pressure vessel close-up and schematic

3.4 Uniaxial Compression

Uniaxial compression testing was performed in order to determine the compressive strength and static modulus of elasticity of the neat and nanosilica addition specimens, cured under both conditions. Three tests were completed for each specimen type.

3.4.1 Specimen Preparation

After the 28 day curing process the elevated curing reactor was depressurized and removed from the heating element. The specimens were allowed to cool, in the open reactor, for 1 hour and 45 minutes ± 5 minutes prior to compression testing. The specimens curing under ambient conditions were removed from the curing room and cooled for 45 minutes ± 5 minutes prior to compression testing. Only the three best specimens from each batch were chosen for compression testing. This was based on visual inspection of micro voids. The chosen specimens had uneven top ends, from troweling and settlement during initial curing, which needed to be made perfectly perpendicular for proper testing. This was achieved by cutting a 3 mm slice from the top end of the specimens using a Buehler® Isomet low speed saw and Buehler® 152.4 mm diamond wafering blade (Figure 3.10).

Figure 3.10 Cylindrical specimens top end preparation

3.4.2 Test Set-up

A MTS® Bionix servohydraulic test system was used for all uniaxial compression testing. The range and resolution of the system are 25 kN and 0.1 N respectively. The system was used in conjunction with a data acquisition system. A 203.2 mm solid steel base plate with a 63.5 mm protruding circular prism was used for the bottom testing surface. A 63.5 mm by 63.5 mm solid steel block was connected to the hydraulic actuator head to transmit the load to the specimens during testing. In order to minimize any eccentricity produced by misalignment of the loading frame or non-perpendicular specimen ends, two 63.5 mm by 63.5 mm by 6.4 mm steel plates with bearing notch and polished stainless steel bearing were used underneath the actuator block. This system is shown in the subsequent figures.

Figure 3.11 Uniaxial compression test system set-up

3.4.3 Procedure

ASTM C39/C 39M was partially used along with some specifications from API 10A to determine the compressive strength of the specimens at 28 days of age [ASTM, International 2005]. This is due to the lack of proper specifications for the uncommon size cylinders. The prepared specimens were dried and cleared of any debris before being centered on the bottom testing surface. The aforementioned two plate and bearing system was centered on top of the specimen and the loading block was applied to the actuator head. Before the start of the test, the actuator head was lowered until safe contact with the specimen. A force controlled loading rate of 18 kN/min ± 2 kN/min was programed into the testing schedule of the system to be used for all compression testing. Tests were run until failure for an average of 3 minutes with slight variations. A minimum of 3 specimens were tested from each different nanosilica percentage and curing condition.

3.4.4 Analysis of Experimental Data

Testing was completed in order to extract the compressive strength and stress strain relationship for each of the specimens. The compressive strength of the specimens f_c was computed as:

$$f_c = \frac{P_c}{A}, \tag{3.1}$$

P_c: Applied compressive load to failure

A: Area of the cylindrical specimen surface subjected to the applied load (A = 507 mm² for 25.4 mm cylinder diameter)

The stress-strain curves were extracted from the force-displacement data points collected by the data acquisition system during testing. The axial stress was calculated as the applied compressive force, at each time step, divided by the constant cross sectional specimen area. The axial strain, at each time step, was calculated as the change in axial displacement from the system extensometer, divided by the original specimen length of approximately 50.8 mm.

3.5 Rapid Chloride-Ion Penetration Testing (RCPT)

RCPT was executed to examine the resistance to chloride ion penetration for each specimen type, to be used as a macroscale permeability comparison. ASTM C 1202-07 was implemented, with modification due to specimen size and composition, to perform this testing [ASTM, International 2005]. Three specimens from each type were tested.

3.5.1 Specimen Preparation

Subsequent to the 28 day curing process the elevated curing reactor was depressurized and removed from the heating element. The specimens were cooled, in the open reactor, for 1 hour and 45 minutes ± 5 minutes prior to rapid chloride-ion penetration testing. The specimens curing under ambient conditions were removed from the curing room and cooled for 45 minutes ± 5 minutes prior to rapid chloride-ion penetration testing. Three visually similar cylinders were chosen from each batch for RCPT. ASTM C 1202-07 was used as a testing guide with minor differences implemented due to the irregular size cylinders [ASTM, International 2005]. The procedure that was used is a follows:

1. A Buehler® Isomet low speed saw and Buehler® 152.4 mm diamond wafering blade were used to cut 3 mm slices off of each end of the cylinders.
2. Specimens were allowed to air dry for at least an hour.
3. A rapid setting epoxy coating was used to seal the side surface of the specimens.
4. Specimens were allowed to dry until no longer sticky to the touch.
5. Any apparent holes in the coating were touched up and allowed to dry.
6. Specimens were placed in a vacuum desiccator with both ends faces exposed for 3 hours.
7. With the vacuum pressure still being applied, de-aerated water was pulled into the desiccator until coverage of the specimens and run for an additional hour.
8. Vacuum pressure was turned off and disconnected from the lines in order to allow air to re-enter the desiccator.
9. Specimens were soaked in the desiccator for 18 hr ± 2 hr before testing.

3.5.2 Test Set-up

Specimens were removed from the desiccator and the excess water removed before being placed in a sealed container in order to maintain 95 % or higher relative humidity. Two polycarbonate testing cells designed for 101.6 mm diameter specimens were used during RCPT. Therefore, two polycarbonate adapter plates were manufactured and used in order to placate the 25.4 mm diameter specimens. These plates were first attached to the testing cells using a high viscosity specimen-cell sealant (100 % silicone) applied along the cell boundary. The specimen ends were then inserted into the hole in each adapter plate and sealed along the specimen adapter plate interface using the same cell sealant. Sealant was allowed to cure for 24 hours with an impermeable rubber material wrapped around the exposed specimen area to prevent moisture movement. Just prior to the start of testing the negative terminal testing cell was filled with 3.0 % NaCl solution and the positive terminal testing cell was filled with 0.3 N NaOH solution. The completed setup is shown in Figure 3.12.

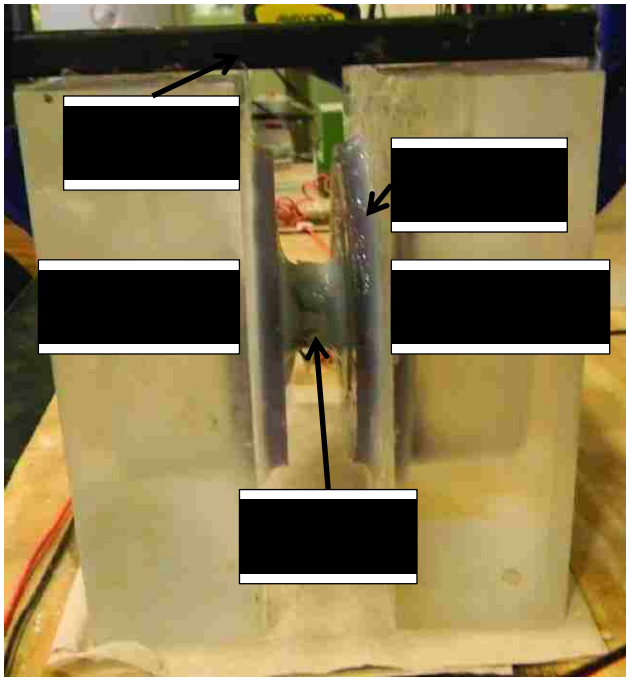

Figure 3.12 RCPT specimen mounted in testing cells

3.5.3 Procedure

Three specimens were run on the testing system at a time. The solution filled and prepared cells and specimens were positioned on the testing system and the wire leads were attached to the cell banana posts appropriate polarity. The power supply of the testing system was turned on and set to 60 V. The testing program was initiated and the electrical current of each of the three specimens was recorded in the system every second for 6 hours. During testing the temperature of the cells and solution was monitored to stay within the requirements of 20 to 25 ˚C. The air temperature around the test system was maintained in the same range. The RCPT setup is shown in Figure 3.13.

Figure 3.13 RCPT complete system setup

3.5.4 Analysis of Experimental Data

The recorded current values (in amperes) were plotted against time (in seconds) through the data for each specimen type. The area beneath the curves was integrated using a Matlab code in order to acquire the ampere-seconds, or coulombs, of charge passed during the 6 hour test period. The Matlab code is supplied in Appendix A.

3.6 Degradation due to Carbonated Brine Exposure

Emergent interest in geologic carbon sequestration has put an emphasis on the need for more data on how well OWC's react to CO_2 exposure. Degradation testing was implemented to quantify the specimen's resistance to attack from an aggressive fluid, such as carbonic acid created during carbon sequestration. The methods described in the International Journal of Greenhouse Gas Control's article *Degradation of oilwell cement due to exposure to carbonated brine* was used as a testing reference and guide [Duguid & Scherer, 2009].

A specialized degradation testing apparatus was contrived to be used throughout the degradation testing process. This system was designed to simulate the characteristics of geosequestration conditions at a depth a 1 km below ground level [Hitchon, 1996]. The system was also intended to simulate sandstone-like conditions of 50 ˚C and pH 5 at the same depth.

3.6.1 Specimen Preparation

After the 28 day curing processes and appropriate cooling techniques, four visually comparable samples from each specimen category were selected for subsequent degradation testing. The uneven top surfaces of the specimens were cut (3 mm slice) and prepared using a Buehler® Isomet low speed saw and Buehler® 152.4 mm diamond wafering blade similar to uniaxial compression testing (Figure 3.10). Specimens were then placed in a 0.5 M NaCl solution in a sealed chamber with a nitrogen induced environment for 28 days of conditioning prior to the start degradation testing. The conditioning setup is shown in Figures 3.14 and 3.15.

Figure 3.14 Degradation testing specimen conditioning setup

Figure 3.15 Degradation testing conditioning chamber open

3.6.2 Test Set-up

A schematic of the set-up and flow through the degradation testing system simulating sandstone-like conditions is shown in Figure 3.16.

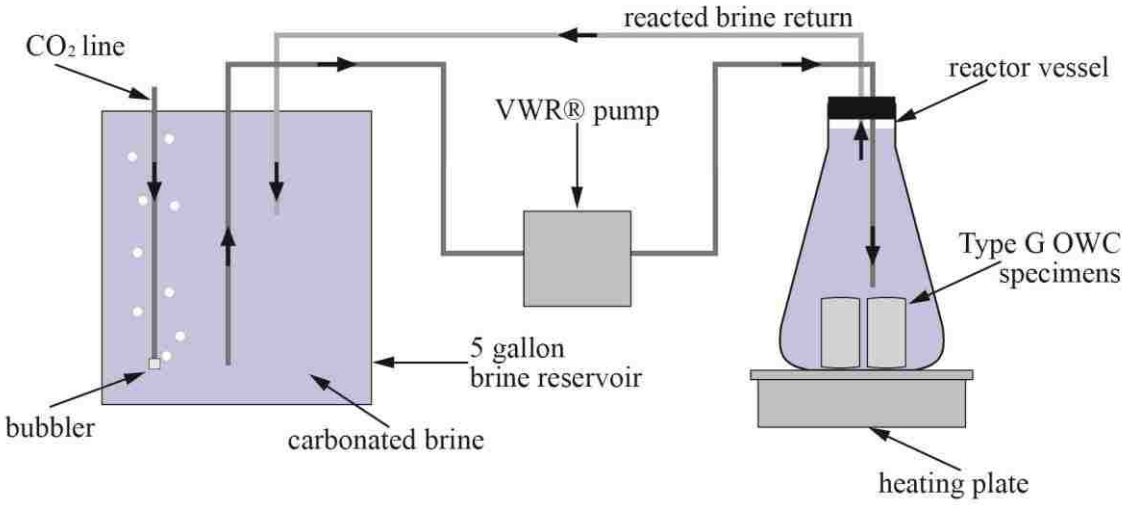

Figure 3.16 Schematic of set-up and flow through degradation testing system

A 5 gallon polyethylene reservoir was insulated and fitted with a heater. A pressure regulator was outfitted to the CO_2 tank and chemical resistant tubing was run from the regulator valve to an inch from the bottom of the reservoir. Additional tubing was run from a depth of 50 mm from the bottom of the reservoir to a VWR® variable flow control mini pump and then from the pump output to the bottom of the reactor. The reactor consisted of a 2000 mL wide mouth Erlenmeyer flask on top of a heating and stirring plate. Tubing was finally run from the top of the reactor through a rubber stopper and back into the original reservoir to complete the cycle. The completed degradation testing setup is shown in Figure 3.17. Before the start of testing the 5 gallon reservoir was filled with a 0.5 M NaCl (brine) solution and heated to 50 ˚C. CO_2 was then bubbled at the bottom of the reservoir at approximately 5-10 psi. The variable flow pump was then set to a rate a 20 mL/min in order to fill the reactor (also heated to 50 ˚C) with the newly

created carbonated brine leaching solution. The setup was allowed to run for 24 hours subsequent to the start of testing in order for system to reach stability.

Figure 3.17 Degradation testing set-up (left) reactor set-up (right)

3.6.3 Procedure

Stability of the system was determined after the 24 hour conditioning period based on a measured temperature of 50 ˚C and a pH of around 5 in the reactor. After stability was achieved the pump was turned off and the specimens were placed inside of the sealed reactor. The variable flow pump was then set to a flow rate of approximately 8 mL/min and turned back on to initiate the start of the testing process. The influent carbonated brine from the reservoir then entered the bottom of the sealed reactor forcing the reacted brine to exit through the return line at the top. This process ensured that the specimens would react with fresh solution throughout the test. The residence time for the reactor was roughly 2 hours and the degradation test was run for 28 days. The degradation testing setup is shown in Figure 3.18.

Figure 3.18 Degradation testing setup

Temperature and pH of the solution in the system was measured frequently throughout the test. The temperature was held stable at 50 ˚C with minor variations of ± 0.2 ˚C. The pH of the system was initially 5.05 but reached a measured value of 4.16 after 28 days of testing.

Samples were collected at specific time intervals staring at the beginning of the test and ending after 28 days. Samples were obtained by cutting small slices, around 5 mm in length, from the cylindrical cement samples in the reactor. This was achieved by using the same Buehler® saw system mentioned earlier. A high resolution scan was taken of each of the samples in order to examine visual degradation. Collected samples were then individually preserved in 0.5 M NaCl in a nitrogen environment until being used for microscopic analysis.

Whole cylinders from each specimen type were also left intact in the reactor for the 28 day time period. These cylinders were used to measure the uniaxial compressive strength and modulus of elasticity of each specimen type subsequent to the degradation process. The degraded cylinders are shown in Figure 3.19.

Figure 3.19 Specimens after degradation testing side view (left) top view (right)

3.6.4 Analysis of Experimental Data

The collected slices from the different time intervals were individually examined to determine the degradation progression for each of the specimen types. Slices approximately 5 mm in height were taken as shown in Figure 3.20.

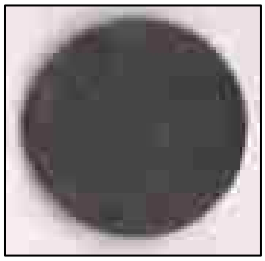

Figure 3.20 Example of slices taken for degradation progression determination

A high resolution scan was taken of each of the samples collected throughout the testing process and the degradation progression was measured from the outer edge of the slice to the inner edge of the visual degradation ring. This measurement was taken in 10 different locations in order to acquire an average value for the degradation advance. An example of the degradation progression and the measurement taken is shown in Figure 3.21.

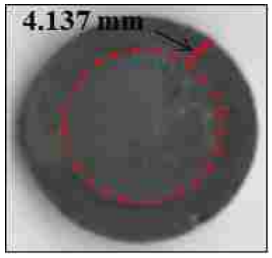

Figure 3.21 Example of degradation progression and measurement taken

The average degradation advancement measurements were plotted against the corresponding time that the slices were taken as demonstrated in section 4.1.3. A linear fit line regression was applied to the data in order to determine the degradation progression in mm/day throughout the entire experimentation as well as advancement over specific time intervals.

3.7 Nanoindentation

Surface probing using depth-sensing indentation (hardness) tests has been used as non-destructive tests for metals for the last 100 years [Hertz, 1881] and it has also been used for decades as a common in-situ test for different types of structures. The objective of nanoindentation is to mechanically characterize the cement paste at the nanoscale. It is of interest to identify both the short term characteristics of cement paste including strength, stiffness and fracture toughness and toughness and the long-term characteristics specifically creep.

3.7.1 Specimen Preparation

Specimens were prepared for nanoindentation by first casting small pieces of each sample type in acrylic to keep the specimens in place and in order to fit them into the nanoindentation holder. The specimens were polished on a Buehler Ecomet® 3 polisher with a Buehler Automet™ 2 power head, which applies a constant pressure to the samples and provides additional spin on the samples for increased polishing efficiency. The steps used during polishing include: 10 minutes with a 125-micron diamond pad, 15 minutes with a 70-micron diamond pad, 15 minutes with a 30-micron diamond pad, 30 minutes with a 9-micron diamond lapping film pad, and 1 hour with a 1-micron diamond lapping film pad. All pads shall be lubricated with lapping oil to keep pads cool and to disperse removed material. Samples are then sonicated in ethanol. The polishing apparatus used is shown in Figure 3.22.

Figure 3.22 Polishing apparatus for preparation on nanoindentation samples

3.7.2 Test Set-up

Polished samples were glued into the nanoindentation holder and mounted in the testing system. The precision of the nanoindentation apparatus is achieved by controlling and recording the time-dependent nanoscale displacement of the indenter tip as it changes with electrical capacitance. Loading is performed by sending an electrical signal to the coil causing the pendulum to rotate about its frictionless pivot, so that the diamond indenter penetrates the sample surface. The indenter tip displacement (penetration) is measured during loading and unloading with a parallel plate capacitor that has sub-nanometer resolution [Fischer-Cripps, 2004]. A schematic of the nanoindentation system with an indentation trace on cement paste and with a schematic representation of loading and unloading cycles are shown in Figure 3.23.

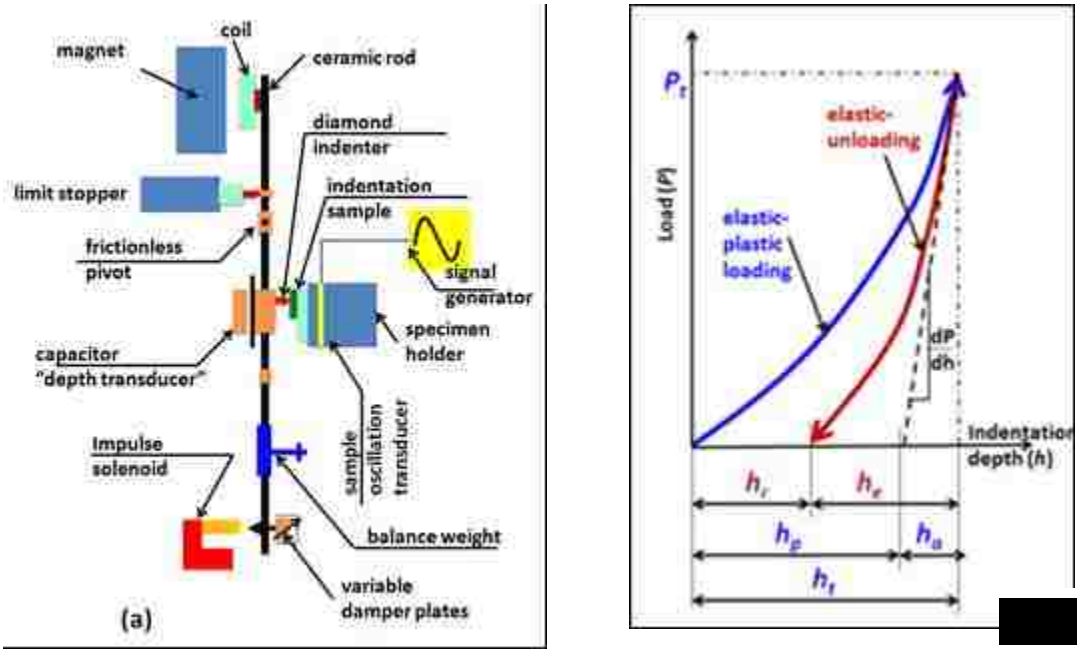

Figure 3.23 (a) Nanoindentation components and (b) loading and unloading during nanoindentation to extract elastic behavior

3.7.3 Procedure

Nanoindentation was then performed using a Berkovich tip and .55 mN loading—.05 mN preloading and .5 mN test loading. A dwell period of 120 seconds was be used at maximum load to account for thermal drift and to enable measuring creep. 50 points were indented on each specimen, in five rows with ten indentations spaced at 200 μm on each row, and their results are analyzed to identify the mechanical characteristics of the microstructural phases of the cement paste.

3.7.4 Analysis of Experimental Data

Extracting elastic modulus using nanoindentation:

Analysis of the nanoindentation data can be performed using the Oliver and Pharr method [Oliver & Pharr, 1992]. This method recognizes the variation of the indented radius with depth. Equation (3.2) defines the total indentation depth h_t as the sum of the plastic depth h_p and the half the elastic displacement leading to

$$h_t = h_p + \frac{h_e}{2} \tag{3.2}$$

[Hertz, 1881] showed that the elastic displacement h_e is defined as

$$h_e = \frac{a^2}{R} \tag{3.3}$$

where a is the radius of the circle of contact at $P = P_t$ and can be calculated as a function of the plastic depth h_p and the indenter radius R_i as described by Equation (3.4) while R is the relative radius of curvature of the residual impression

$$a = \sqrt{2R_i h_p - {h_p}^2} \tag{3.4}$$

The relative radius of curvature R can be based on the radius of curvature of the indenter R_i and the radius of curvature of the residual impression R_r

$$\frac{1}{R} = \frac{1}{R_i} - \frac{1}{R_r} \tag{3.5}$$

The contact area *A* can be calculated from knowing the radius of the circle of contact *a*. Oliver and Pharr [Oliver & Pharr, 1992] recognized that the unloading curve for a majority of materials indented followed a power fit rather than a linear relationship. Therefore, a power function can be fit to top 60% of the unloading curve and the slope of indentation load-depth curve (*dP/dh*) will be calculated as the slope of a line tangent to the power fit relationship or the derivative of the power fit relationship. For the duration of each indentation, the applied load and the displacement of the specimen material are constantly measured, including unloading. The reduced modulus, E^* is calculated as Equation (3.6) [Oliver & Pharr, 1992; Fischer-Cripps, 2004]:

$$E^* = \frac{1}{2\beta}\frac{\sqrt{\pi}}{\sqrt{A}}\frac{dp}{dh} \tag{3.6}$$

where β is a correction factor to account for the non-symmetrical shape of the indenter tip, which is equal to 1.034 for a 3-sided pyramidal (Berkovich) indenter. *A* is the contact area of the indenter, which is found by knowing the geometry of the indenter tip as a function of the depth, and the measured depth. For a Berkovich indenter tip, *A* is equal to Equation (3.7) [Oliver & Pharr, 1992; Fischer-Cripps, 2004]:

$$A = 3\sqrt{3}{h_p}^2 * tan^2\theta \tag{3.7}$$

where h_p is the depth of penetration and θ is the angle the edge of the indenter makes with the vertical. The reduced modulus E_r is used in lieu of Young's modulus to account for the effect of the indenter stiffness on measurements. The reduced modulus E_r is derived from Equation (3.8), where ν is Poisson's ratio and *E* is Young's modulus of the indented phases E' and ν' are values corresponding with the indenter frame used respectively 1141 GPa and 0.07 as reported by the indenter calibration.

$$\frac{1}{E_r} = \frac{1-\nu^2}{E} + \frac{1-\nu'^2}{E'} \tag{3.8}$$

Statistical deconvolution of nanoindentation observations:

When a Berkovich indenter tip is used to test the cement paste, the results of nanoindentation cannot be interpreted without conducting statistical deconvolution analysis. The objective of statistical deconvolution is to decompose the final results observed in nanoindentation (stiffness) into a group of sub-microstructural phases of C-S-H. The analysis starts by determining a suitable bin size. First, the difference between the maximum and minimum data points is divided by the number of data points to find an initial bin size. A histogram is then formed from the data. The bin size can be adjusted until an appropriate histogram is created. A good way to pick the ideal bin size can be done if the number of phases expected to be present in the sample is known. The number of bins required can be calculated as K = 3N-1, where N is the number of phases in the sample.

Using the frequencies of each bin, an experimental density function (EDF) is calculated as (f/K) /N, where f is the frequency, K is the bin size, and N is the number of data points. An EDF point is calculated for each bin. The data is then fit to individual probability density functions (PDFs), where each phase is represented by its own PDF. The PDFs can be calculated as Equation (3.9):

$$p(x_j) = \frac{e^{-\left(\frac{(x_j-u)^2}{2*\sigma^2}\right)*f_i}}{\sigma * \sqrt{2\pi}} \tag{3.9}$$

here, μ is the average value, σ is the standard deviation, and f_i represents the surface fraction occupied by the *i-th* phase on the indentation surface. The standard error R between points of the EDF and points of the PDFs shall be minimized. R can be computed as Equation (3.10):

$$R = \sum_{j=1}^{m} \frac{\left(EDF_j - p(x_j)\right)^2}{m} \tag{3.10}$$

where EDF_j is the value of the experimental density function at the *j-th* bin, $p(x_j)$ is the PDF value for the corresponding value of the *j-th* bin, and *m* is the number of bins used in the construction of the EDF. To properly fit the PDFs to the EDF, *R* shall be minimized. Each PDF is scaled down to its appropriate size by multiplying all points by the volume fraction of the corresponding phase. The mean, standard deviation, and volume fraction values are all iterated until *R* reaches its minimum value. Each PDF is then representative of one of the phases present in the indented specimen.

3.8 Brunauer-Emmett-Teller (BET) N2 & Barrett-Joyner-Halenda (BJH)

The BET N2 method and theory was implemented in order to determine the specific surface area, of each sample type, from nitrogen gas absorption/desorption measurements. The BET N2 method is an analytical pore structure characterization method based on an analytical equation fitted to the isotherm data from which the specific surface area can be extracted [Aligizaki, 2006].

The BJH method and theory was applied in order to acquire a pore size distribution for each sample type, from capillary condensation measurements. The BJH method is an analytical method, applicable to almost all types of porous materials, used to characterize the pore size distribution [Aligizaki, 2006].

3.8.1 Specimen Preparation

Ambient and elevated cured specimens of each type were broken into small pieces and ground to a fine powder using a hardened porcelain mortar and pestle (Figure 3.24) to be used for subsequent microstructural characterization testing.

Figure 3.24 Hardened porcelain mortar and pestle (left) prepared fine powder (right)

3.8.2 Test Set-up

Approximately 100-300 mg of the prepared fine powder was placed in the physisorption tube and consolidated at the tube bulb. The physisorption tube was then attached to the Autosorb-1 testing apparatus by Quantachrome Instruments® and the cold trap was moved into place over the physisorption tube.

3.8.3 Procedure

The system was run under liquid nitrogen temperatures and the saturation pressure was measured initially for reference for the subsequent procedure. The volume of nitrogen being absorbed and the relative pressures were measured for roughly 8-10 hours per test. Finally, the system was outgassed overnight without heating. The test system setup is shown in Figure 3.25.

Figure 3.25 BET N2 physisorption testing system

3.8.4 Analysis of Experimental Data

The extracted values for the volume of nitrogen gas being adsorbed and the corresponding relative pressures were used to produce absorption isotherms. There are six different types of adsorption isotherms that are representative of various materials. Classification of the adsorption isotherm type allows for certain conclusions to be drawn about the characteristics of the material used [Aligizaki, 2006].

The BET equation was then applied to the isotherms and is as follows

$$\frac{P}{V(P_0 - P)} = \frac{1}{V_m C} + \frac{(C-1)P}{V_m C P_0} \tag{3.11}$$

where V is the volume of absorbed vapor at pressure P (m^3 per gram of absorbent), V_m is the volume of nitrogen gas adsorbed when the entire surface is covered by a monomolecular layer (m^3 per gram of adsorbent), C is the BET constant, P is the pressure (N/m^2) and P_0 is the saturation vapor pressure (N/m^2).

A plot of $P/[P_0V\,(1 - P/P_0)]$ vs. P/P_0 commonly provides a straight line in the region of relative pressures near completed monolayers, which is considered the multipoint BET plot [Aligizaki, 2006]. The slope and intercept of the BET plot a given in Equation (3.3). Using these values, the volume of gas adsorbed in a monomolecular, V_m, layer and the BET constant, C, can be determined from Equation (3.4)

$$s = \frac{C-1}{V_m C} \quad i = \frac{1}{V_m C} \tag{3.12}$$

$$V_m = \frac{1}{s+i} \quad C = \frac{s}{i} + 1 \tag{3.13}$$

where s is the slope (g/m^3), i is the intercept (g/m^3), C is the BET constant and V_m is the volume of gas adsorbed when the entire surface is covered by a monomolecular layer (m^3 per gram of adsorbent). Subsequently, after determining V_m, the specific surface area can be calculated as

$$S = \frac{V_m N_A A_m}{V_M} * 10^{-20} \tag{3.14}$$

where S is the specific surface area (m^2/g), V_m is the volume of gas adsorbed when the entire surface is covered by a monomolecular layer (m^3 per gram of adsorbent), A_m is the average area occupied by one molecule of adsorbate in the completed monolayer (m^2/molecule), V_M is the molar volume (m^3/mol) and N_A is the Avogadro constant (molecules/mol).

When nitrogen is used as the adsorbate, as in this case, the specific surface area can be determined by the following equation

$$S = \frac{(6.023 * 10^{23})(16.2 * 10^{-20})V_m}{22.4 * 10^{-3}} \ \ or \ \ S = 4.35V_m * 10^6 \left(\frac{m^2}{g}\right) \tag{3.15}$$

The BJH method was applied to the isotherm to produce a plot of pore volume against pore diameter. The pore volume and pore radius data points were extracted from the adsorption isotherm during testing, using the accompanying physisorption software Autosorb 1.

3.9 X-Ray Diffraction Analysis (XRDA) Testing

X-ray diffraction analysis (XRDA) is a recognized methodology in cement chemistry [Taylor, 1997] used to detect various compounds in a cement paste. XRDA is typically utilized to classify crystalline materials. Bearing in mind that a crystalline structure has numerous repeating atomic planes, as shown in Figure 3.26, the angle between the emitted and diffracted X-ray beams are measured. When the X-ray beams having a wavelength λ are emitted to the atomic planes of a material with an angle of incidence θ, the beams are diffracted of transmitted according to the distance d between the atomic planes. This spacing is often termed as 'd-spacing' or 'basal spacing', of the material. An exclusive spectrum of diffraction angle with respect to the corresponding incident angle (2θ) is identified. The detected spectrum is used to classify the material. Implementing the XRD spectra, several compounds in hydrated cement pastes suck as alite (C_3S), belite (C_2S), ettringite (AF_t), calcium hydroxide (CH, portlandite) and calcium silicate hydrate tobermorite (C-S-H) can be identified. There exists an abundance of information in literature on XRD observations of cement hydration products [Taylor, 1997; Mehta & Monterio, 2006; Diamond, 1976].

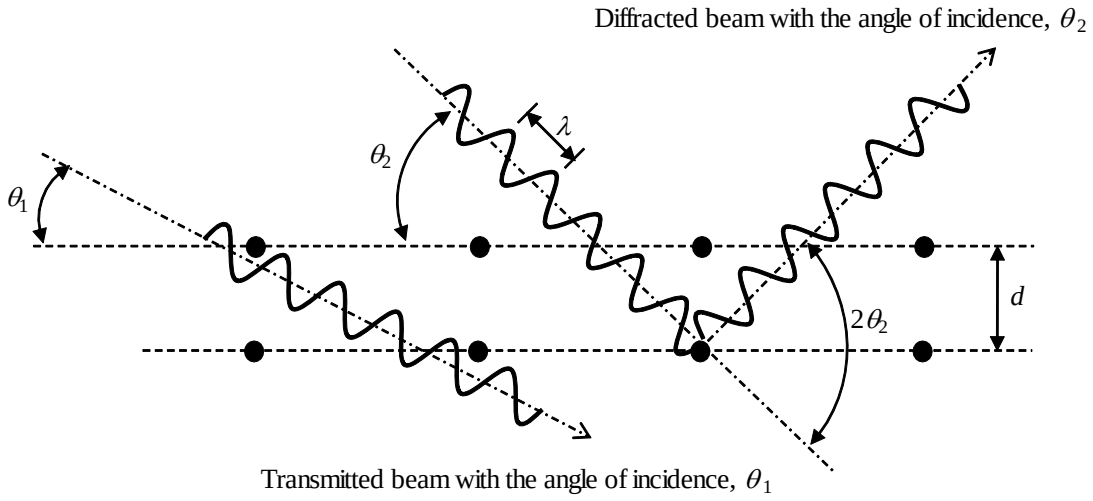

Figure 3.26 Description of XRD technique using Bragg's law

3.9.1 Specimen Preparation

Ground fine powder, from each specimen type, was used for XRD testing and analysis. The fine powder was prepared using the same technique described in section 3.8.1.

3.9.2 Test Set-up

A Rigaku® SmartLab system (Cu K-alpha radiation with wavelength λ = 0.154 nm) was used for all XRD testing. Prepared fine powder, approximately 30 grams, was input in the testing system sample mount before the start of the procedure.

3.9.3 Procedure

The system was operated under an open attenuator run of 40 kV, 40 mA and used a Ni filter at room temperature, with optimization for scattering angles, θ, of $2^\circ < \Theta < 90^\circ$. The XRD spectra were acquired in 10 minutes under a rate of 8˚/min. The XRD testing system is shown in Figure 3.27.

Figure 3.27 Rigaku SmartLab XRD testing system

3.9.4 Analysis of Experimental Data

Equation 3.2 shows the relation between the *d*-spacing, *d*, and the angle of diffraction θ.

$$\lambda = 2dsin\theta \tag{3.16}$$

where λ is the wave length used in nm, *d* is the *d*-spacing between nanoplatelets in nm, and θ is the diffraction angle in degrees.

The calcite phases were determined by an experienced chemist, using MDI Jade 2010 version 2.1.6 and the ICPP Powder Diffraction Database Release 2012, to be used for further examination.

3.9 Nuclear Magnetic Resonance (NMR) Testing

NMR testing and analysis has been proven over the years to be an effective technique for inspection of chemical bonds in different materials [Günther, 1995]. For 29Si solid state NMR testing, the magnetic spinning angle (MAS) method is implemented to avoid large peak augmentations created by numerous nuclear interactions. NMR is helpful in identifying the nanostructure of silicate composites. 29Si NMR has been used to examine the polymerization of a silicate tetrahedron in synthetic calcium silica hydrate (C-S-H) [Lippmma et al., 1980]. Silicate polymerization is representative of the number of bonds produced by the silicate tetrahedron. A silicate tetrahedron having the number of *n* shared oxygen atoms is expressed as Q^n where *n* is the number of oxygen atoms, up to 4. The intensity of the silicate Q connections in hydrated cement can be examined using ^{29}Si MAS NMR. The Q^0 connection is typically detected in hydrated cement due to the residual tricalcium silicate (C_3S) and dicalcium silicate (C_2S). The Q^1 (end-chain group), Q^2 and Q^3 (middle-chain group) in silicate are normally observed due to the layered structure of C-S-H. The Q^4 connection is representative of the polymerization of quartz and can be detected in silica rich products such as fly ash, silica fume and nanosilica.

3.9.1 Specimen Preparation

Ground fine powder, from each specimen type, was used for NMR testing and analysis. The fine powder was prepared using the same technique described in section 3.8.1.

3.9.2 Test Set-up

A 7 mm Bruker® rotor and cryomagnet for NMR spectroscopy (BZH 300/89) was used for all NMR testing. The 7 mm rotor was loosely filled with fine powder and tamped down by striking the bottom of the rotor on a hard surface. After compaction the rotors were approximately two thirds full, before being capped and cleaned subsequent to the start of the procedure.

3.9.3 Procedure

The ^{29}Si standard was initially run, before testing of the sample types, in order to calibrate the testing device and have a comparison reference. Solid state NMR, using the MAS method, was then conducted by spinning the sample at a frequency of 1-35 kHz around an axis oriented 54.7˚ to the magnetic field [Macomber, 1998]. Spinning was stabilized at just under 35 kHz before the TopSpin™ data acquisition software was executed. Each specimen type was spun and tested for a minimum of 6 hours, to ensure adequate and reliable results. The NMR testing system is shown in Figure 3.28.

Figure 3.28 Cryomagnet for NMR spectroscopy

3.9.4 Analysis of Experimental Data

As the neighboring silicate connection of a silicate tetrahedron affects the chemical shifts, the chemical shifts for silicate have significant variations [Wieker et al., 1982; Young, 1988; Grutzeck et al., 1989]. This variation requires execution of statistical deconvolution analysis of ^{29}Si MAS NMR spectra to classify the different chemical shift peaks, representing silica polymerization type Q^0 to Q^4, and their corresponding intensities signifying their existing fraction of C-S-H. Using the calculated intensities of the Q^ns, the average degree of C-S-H connectivity D_c is calculated after Saoût et al. [Saoût et al., 2006] as

$$D_c = \frac{Q^1+2Q^2+3Q^3}{Q^1+Q^2+Q^3} \tag{3.17}$$

High D_c values represent high polymerization of C-S-H. From the numerous studies of the structure of C-S-H by ^{29}Si MAS NMR, it is suggested that the polymerization of C-S-H depends on its compositional calcium-silicate (C/S) ratio (high polymerization for low C/S ratio) and the humidity in the interlayer water (high polymerization for low interlayer water) [Bell et al., 1990; Cong & Kirkpatrick, 1996]. Additionally, the degree of hydration h_c of a hydrated cement paste, defined as the weighted average of the degree of reactivity of the four major cement components, C_3S, C_2S, C_3A and C_4AF [Jennings & Tennis, 1994], can be projected from the de-convoluted intensities of Q^ns. Initially, assessment of the total number of silicate tetrahedrons N_Q is calculated as

$$N_Q = b\left[(1-p_s)\left(\frac{p_{C3S}}{M_{C3S}}+\frac{p_{C2S}}{M_{C2S}}\right)+\frac{p_S}{M_S}\right]N_A \tag{3.18}$$

where N_A is Avogadro's constant. M_{C3S}, M_{C2S} and M_S are molecular weights of C_3S, C_2S and S, which are 0.228 kg/mol 0.172 kg/mol and 0.06 kg/mol [Jennings & Tennis, 1994] respectively. p is the weight of the subscribed components in the cement and nanosilica binder. b is the initial weight of the binder (in grams) per 1 g of cement paste, calculated as

$$b = \frac{1}{1+w/b} \tag{3.19}$$

where, *w/b* is the initial water to binder ratio of cement paste incorporated to nanosilica. Given that Q^0 associates with the unreacted C3S and C2S, and denoting the degree of reactivity of C_3S and C_2S and C_2S as α_{C3S} and α_{C2S}, respectively, the numbers of silicate tetrahedrons having Q^0 connection in the remaining C_3S and C_2S, $N_{Q0,C3S}$ and $N_{Q0,C2S}$, respectively, are calculate as

$$N_{Q0,C3S} = b(1 - p_s)\frac{p_{C3S}(1-\propto_{C3S})}{M_{C3S}}N_A \tag{3.20}$$

$$N_{Q0,C2S} = b(1 - p_s)\frac{p_{C2S}(1-\propto_{C2S})}{M_{C2S}}N_A \tag{3.21}$$

The Q^0 fraction extracted from ^{29}Si MAS NMR is the assessed as

$$Q^0 = \frac{N_{Q0,C3S}+N_{Q0,C2S}}{N_Q} \tag{3.22}$$

To determine the degree of reactivity α_{C3S} and α_{C2S} for a given Q^0 fraction observed from ^{29}Si MAS NMR spectra, an Avramidu-type Equation (3.23) describing the degree of reactivity of the four major cement components [Taylor, 1997].

$$\propto = 1 - exp(-a(t-b)^c) \tag{3.23}$$

The constants *a*, *b* and *c* used in the above equation are representative of the major cement components of C_3S, C_2S, C_3A and C_4AF. These values are presented in Appendix B with the corresponding weight fractions of type G OWC. Substituting equations (3.5), (3.20) and (3.23) into equation (3.22), generates a solution for the time variable *t*. Using the given constants and the calculated time variable *t*, the degree of reactivity of the four major cement components can be determined from equation (3.23). The degree of hydration, h_c, can then be approximated as the weighted average of the degree of reactivity of the four major cement components as

$$h_c = \frac{p_{C3S}\propto_{C3S}+p_{C3S}\propto_{C2S}+p_{C3A}\propto_{C3A}+p_{C4AF}\propto_{C4AF}}{p_{C3S}+p_{C2S}+p_{C3A}+p_{C4AF}} \tag{3.24}$$

The total mass of C-S-H per 1 g of cement paste, m_{CSH}, can be calculated as

$$m_{CSH} = b(1 - p_s)\left(\frac{p_{C3S}\propto_{C3S}}{M_{C3S}} + \frac{p_{C2S}\propto_{C2S}}{M_{C2S}}\right)M_{CSH} \tag{3.25}$$

where M_{CSH} is the molecular weight of C-S-H and 0.188 kg/mol used from the composition of C-S-H as $(C_aO)_{1.7}(SiO_2)(H_2O)_{1.8}$ [Allen et al., 2007]. Tennis and Jennings [Tennis & Jennings, 2000], suggested estimating the ratio of the mass of LD-C-S-H to the total mass of C-S-H denoted *m*, as

$$m_r = 3.017(w/c)h_c - 1.347h_c + 0.538 \tag{3.26}$$

Furthermore, the mass of LD-C-S-H and HD-C-S-H can be calculated as

$$m_{LD} = m_{CSH}m_r, \quad m_{HD} = m_{CSH}(1 - m_r) \tag{3.27}$$

Using the density of LD-C-S-H and HD-C-S-H as 1440 kg/m^3 and 1750 kg/m^3, respectively, when the pores are empty [Sanchez & Frias, 1995], the volumes of LD-C-S-H and HD-C-S-H per 1 g of cement paste, V_{LD} and V_{HD}, can be determined. Additionally, the volume of CH per 1 g of cement paste is calculated as

$$V_{CH} = b(1 - p_s)(0.189 \propto_{C3S} p_{C3S} + 0.058 \propto_{C2S} p_{C2S}) \tag{3.28}$$

The above volumes constitute the volume of cement paste not taking into account pozzolanic reactivity. Therefore, a correction accounting for the increase in C-S-H volume due to pozzolanic activity is required to determine the true volume of C-S-H [Garcia et al., 2007]. The correction can be done by estimating the pozzolanic reactivity of nanosilica, α_{S}, which can be approximated by implementing Q^4 intensity observations from the de-convoluted NMR spectra as

$$\propto_S = 1 - Q^4\frac{N_Q}{N_{Q4,S}} \tag{3.29}$$

where $N_{\mathrm{Q4,S}}$ is the number of silicate tetrahedron in nanosilica as

$$N_{Q4,S} = b\left(\frac{p_S}{M_S}\right)N_A \tag{3.30}$$

Subsequently, the reacted volume of nanosilica per 1 g of cement paste is calculated as

$$V_S = \frac{\propto_S b p_S}{\gamma_S} \tag{3.31}$$

where γ_S is the density of nanosilica as 2230 kg/m^3. The increase of C-S-H volume and the decrease of CH volume by the pozzolanic reactivity of nanosilica can then be determined as $1.35V_S$ and $3.77V_S$ respectively [Garcia et al., 2007]. The relative volume fraction of LD-C-S-H, HD-C-S-H and CH and pozzolanic C-S-H formed can then be calculated as

$$V_t = V_{LD} + V_{HD} + V_{pCSH} + V_{CH} - V_{pCH} \tag{3.32}$$

$$rV_{LD} = \frac{V_{LD}}{V_t}\%,\ rV_{LD} = \frac{V_{LD}}{V_t}\%,\ rV_{LD} = \frac{V_{LD}}{V_t}\%,\ rV_{LD} = \frac{V_{LD}}{V_t}\% \tag{3.33}$$

Chapter 4 Results and Discussion

4.1 Macroscale Characterization

4.1.1 Uniaxial Compression

The extracted uniaxial compressive strength of all the specimens is shown in Figure 4.1 and 4.2. The y-axis of the Figure represents this strength in units of MPa to the extent of 30 MPa.

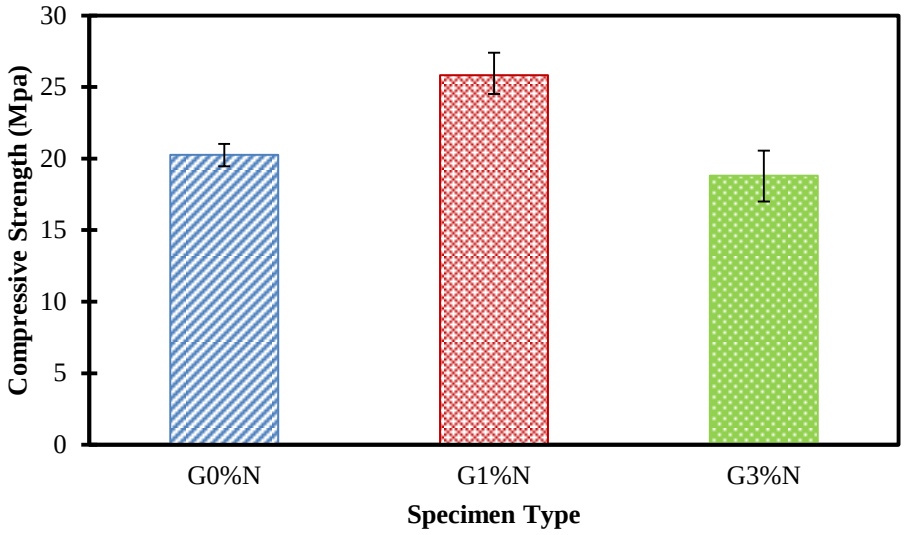

Figure 4.1 Uniaxial compressive strength comparisons (ambient curing)

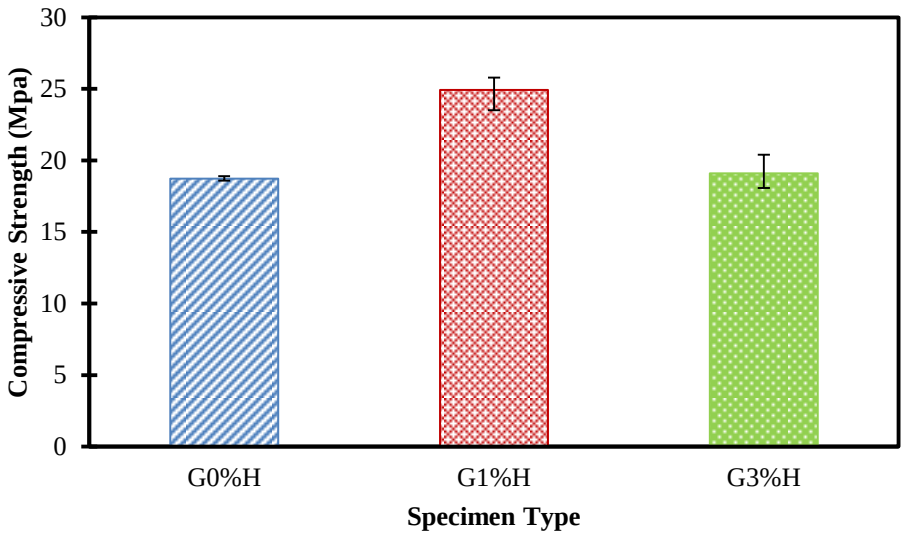

Figure 4.2 Uniaxial compressive strength comparisons (elevated curing)

The neat specimens presented compressive strength values of 20.2 MPa and 18.7 MPa for the ambient and elevated cured specimens. The specimens with the 1% nanosilica addition exhibited the greatest compressive strength with a stress of 25.9 MPa and 24.9 MPa for the ambient and elevated cured specimens respectively. These values represent a statistically significant increase in compressive strengths of 27% and 33% for the respective curing condition, in comparison to the neat specimens. Specimens with the 3% nanosilica addition displayed similar behavior as the neat samples with statistically insignificant variations in the compressive strength in comparison to the neat.

An average of the three extracted stress-strain curves was taken in order to produce an overall stress-strain curve representation for each specimen type. This relationship is illustrated in Figure 4.3.

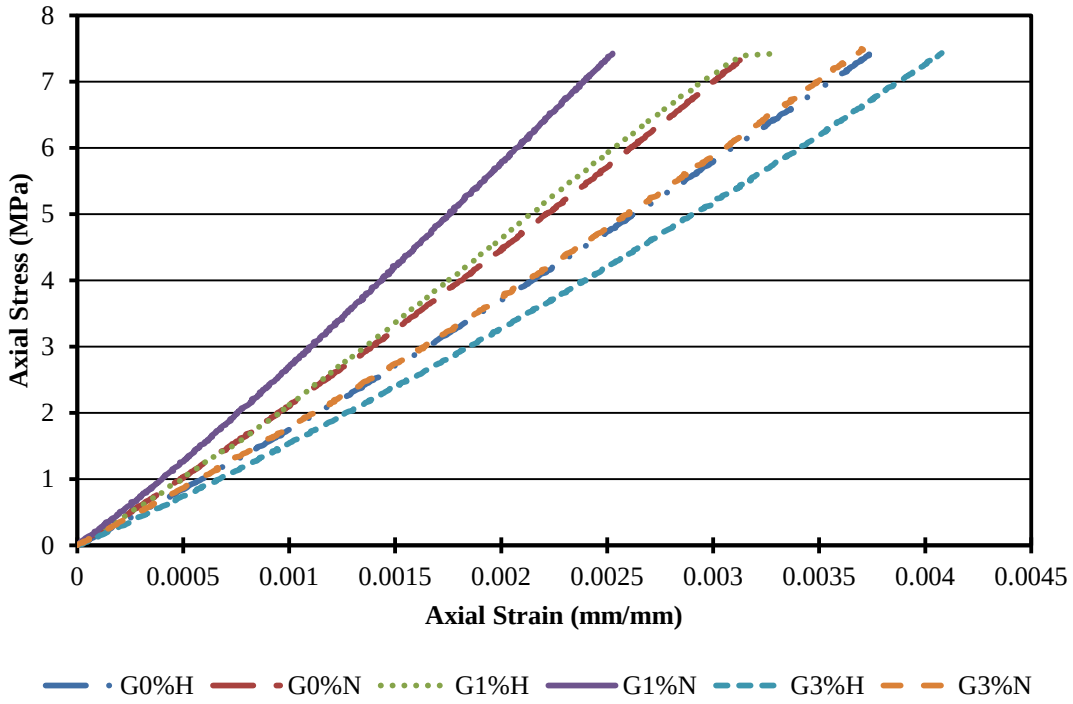

Figure 4.3 Axial stress-axial strain relationships for each specimen type

The curves are shown to the extent of the least axial strain developed in a specimen type for comparison. Each specimen type demonstrated relatively linear initial behavior as demonstrated by the linearity of the curves. For practical comparison purposes, the normal and ambient curing condition cases are further separated as shown in Figure 4.4 and Figure 4.5. In both Figures, the blue line represents the neat specimen type without the incorporation of nanosilica. The red line denotes the specimen category with the 1% nanosilica addition and the blue line the 3% nanosilica addition.

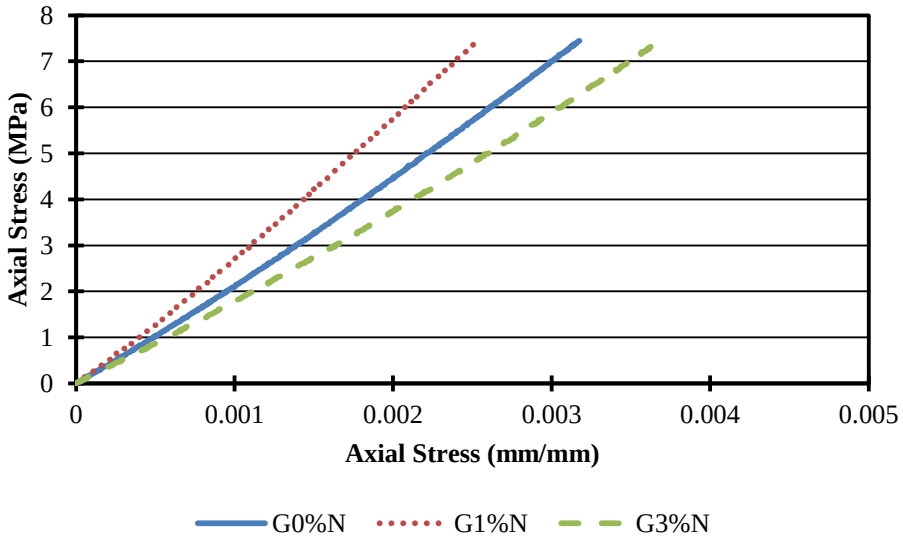

Figure 4.4 Axial stress-axial strain relationships (ambient curing)

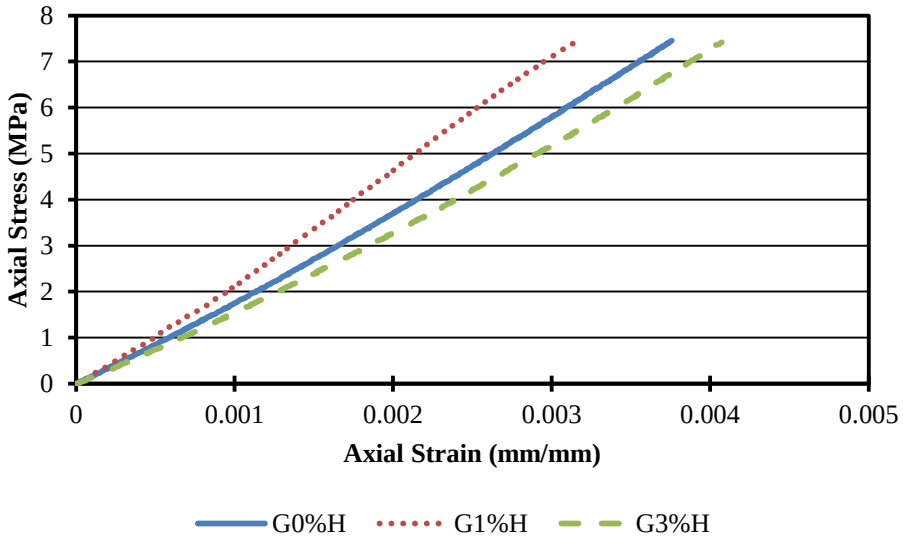

Figure 4.5 Axial stress-axial strain relationships (elevated curing)

The axial stress-strain figures above for ambient and elevated curing conditions demonstrate exceptionally similar behavior. In both cases the 1% nanosilica addition specimen type curve had the greatest slope throughout the test. The slope of the 3% nanosilica specimen type curve was the smallest for both cases and the slope of the neat specimen type curve lied in between the 1% and 3% curves as shown in the figures above.

The slope of the axial stress-strain curves represents the static modulus of elasticity for each specimen type. This modulus was extracted using the initial tangent modulus method for all specimen types (Figure 4.6 and 4.7).

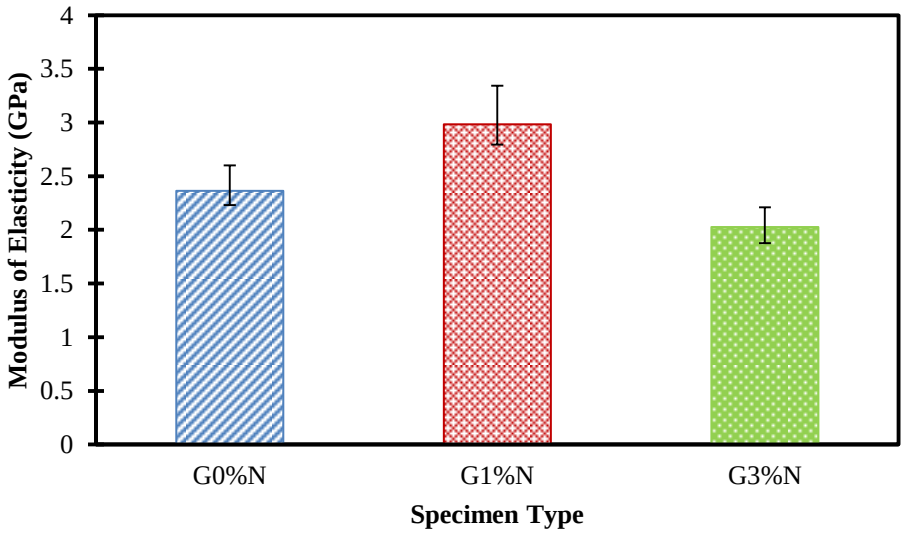

Figure 4.6 Static modulus of elasticity comparison (ambient curing)

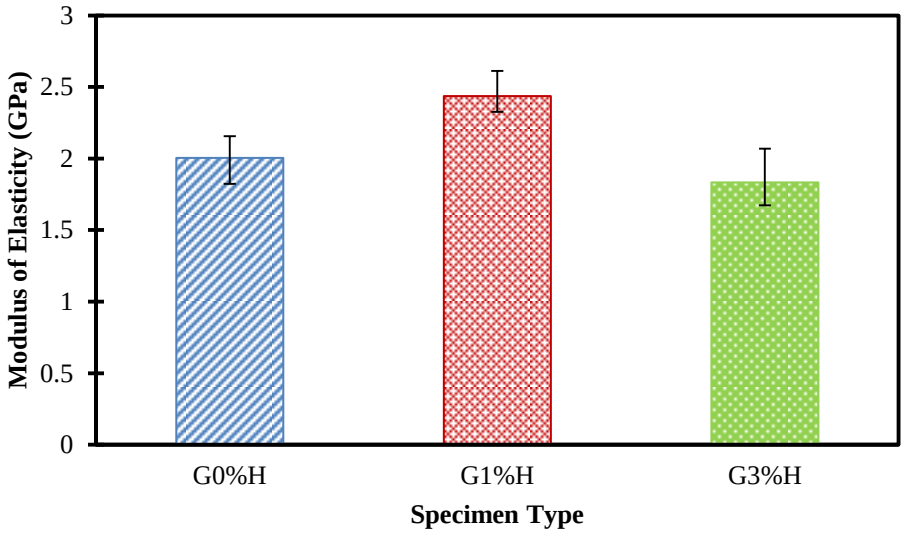

Figure 4.7 Static modulus of elasticity comparison (elevated curing)

The neat specimen type subjected to ambient curing produced a modulus of elasticity of approximately 2.4 GPa. The 1% nanosilica addition produced a modulus increase, of statistical insignificance, of nearly 0.6 GPa to a value of approximately 3 GPa, which represents a 26% increase. The 3% nanosilica addition produced a modulus decrease, of statistical insignificance, of around 0.4 GPa to a value of 2 GPa, which represents a 15% decrease. This comparison is shown above in Figure 4.6 for ambient curing conditions.

Elevated curing conditions produced results very similar to the ambient curing conditions with an overall decrease, as shown in Figure 4.7. The neat specimen type produced a modulus of approximately 2 GPa under the oil well simulated curing conditions. The 1% nanosilica addition increased the modulus by about 0.4 GPa, 22%, to a value of approximately 2.4 GPa in comparison with the neat specimen type. The 3% nanosilica addition decreased the modulus by around 0.2 GPa, 8%, to a value of 1.8 GPa also in comparison with the neat type. The 1% nanosilica addition modulus increase was statistically significant while the 3% addition decrease produced statistical insignificance.

The 1% addition of nanosilica produced statistically significant increases in the compressive strength and modulus of elasticity, under both curing conditions. This is due to the incorporation which is believed to create a denser material by filling voids and transforming the nano/microstructure of the material, before, during and after hydration. The 3% nanosilica addition produced insignificant changes in the compressive strength and modulus of elasticity in contrast with the neat. This is most likely attributed to the low workability of the 3% nanosilica addition which only showed a flow of 34%, in flowability tests, in comparison with 150% flow for the neat and 1% mixes. The low workability entrapped air in the specimens during casting and created an imperfect final product with added voids. Therefore, the 3% nanosilica addition experienced a minor reduction in strength and stiffness in comparison with the neat specimens.

4.1.2 Rapid Chloride-Ion Penetration Testing (RCPT)

Current (in amperes) versus time (in seconds) was plotted for each specimen type. The results are shown in Figure 4.8.

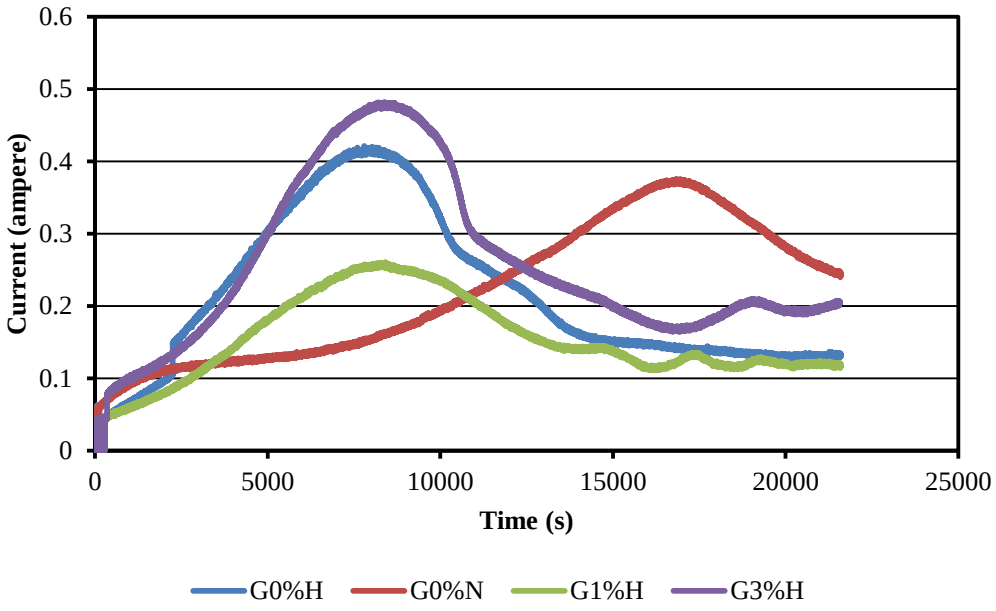

Figure 4.8 Current versus time for each specimen type

The specimens cured under elevated curing conditions exhibited similar behavior with significant differences in the maximum current exposure. These specimens all reached a maximum current exposure during the first 2 hours of the test and then slowly decreased until almost constant forming a somewhat parabolic shape. The specimens cured under ambient conditions showed nearly inverse behavior reaching a maximum current exposure just under the 5 hour mark. The specimen type with the 3 % nanosilica addition reached a maximum current of approximately 0.5 amperes during testing. The specimen type with the 1 % nanosilica addition reached a maximum current of roughly 0.25 amperes and the neat specimen type reached a maximum current of 0.37 and 0.42 amperes for ambient and elevated curing respectively. The greater maximum creates a larger derived area underneath the curve which directly relates to an increased charge passing through the specimen, therefore high porosity and low resistance to the penetration of chloride ions. The charge passing (in coulombs) is represented for each specimen type in Figure 4.9.

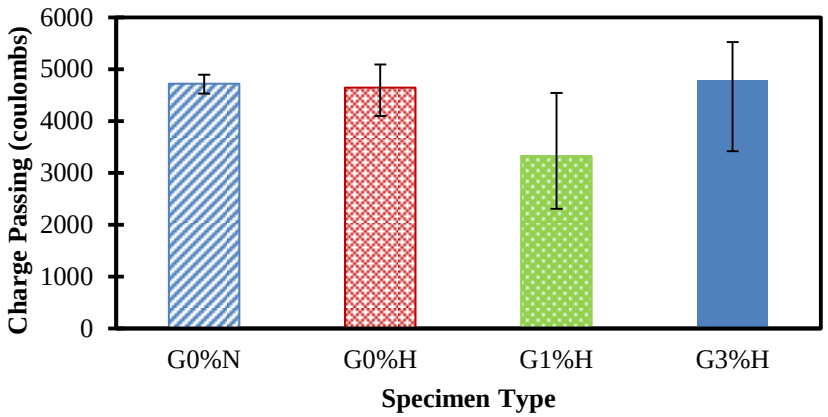

Figure 4.9 Charge passing per specimen type

The neat specimens produced relatively similar values of 4720 and 4645 coulombs passing for the ambient and elevated curing conditions respectively. The 1 % nanosilica specimens generated the lowest charge passing with the average being 3325 coulombs. The 3 % nanosilica addition specimen type produced the highest passing charge of 5486 coulombs. The above values are relative to each other and not absolute due to their uncommonly small size. The 1 % nanosilica addition has statistical significance in the resistance to the penetration of chloride ions, on the order of 28 % in comparison to the neat case. The 3% nanosilica addition produced a decrease in penetration resistance of a statistically insignificant 3%. The aforementioned ASTM has a table for interpretation of the range of results for a standard 101.6 mm diameter concrete cylinder. This table indicates that a charge passing (in coulombs) greater than 4,000 is classified as “high” chloride ion penetrability. The table also designates a subsequent “moderate” classification with a range of 2,000 to 4,000 coulombs. The 1 % nanosilica addition improved the classification of the specimens to “moderate” from the original “high” classification of the neat samples.

The 1% nanosilica addition again enhanced the specimen’s performance requirements in regards to permeability and the 3% nanosilica addition made the specimens slightly more permeable. These results are in agreement with the compressive strength testing results and they further reaffirm that the 1% nanosilica addition creates a denser material composition with diminished voids and the 3% addition does the contrary.

4.1.3 Degradation due to Carbonated Brine Exposure

The extracted uniaxial compressive strength of the specimen types subsequent to degradation testing is shown in Figure 4.10. A comparison between the uniaxial compressive strength before degradation testing is shown in Figure 4.11.

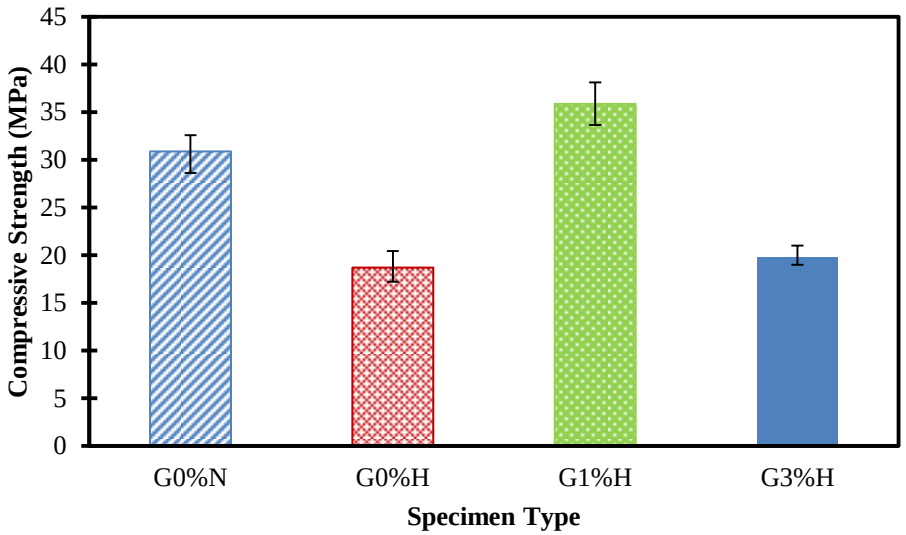

Figure 4.10 Uniaxial compressive strengths after degradation testing

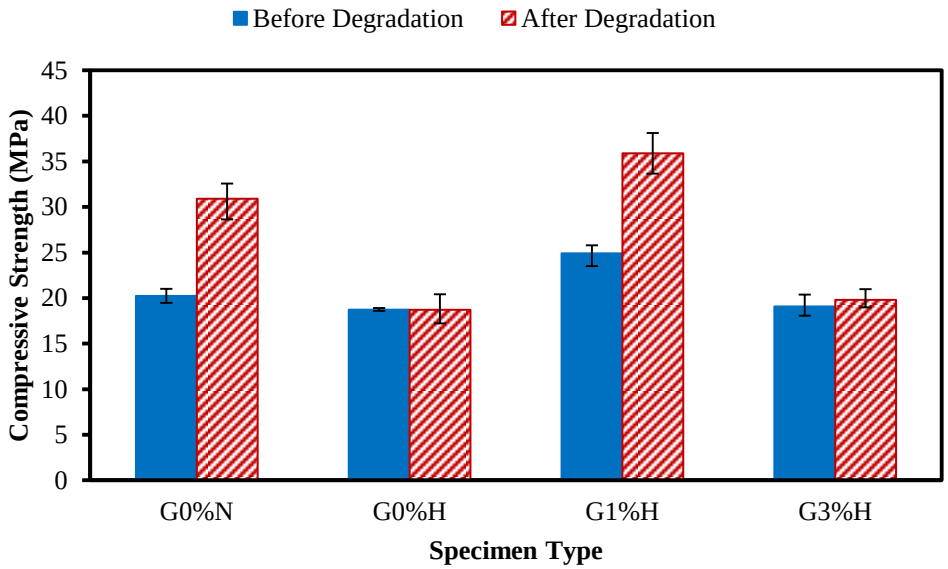

Figure 4.11 Uniaxial compressive strengths before and after degradation testing

The compressive strength of the neat specimens cured under elevated conditions stayed relatively similar after degradation testing. Neat specimens cured under ambient conditions showed a compressive strength increase of around 53 %. The 1 % nanosilica addition specimen type cured under elevated conditions revealed a statistically significant compressive strength increase of 44 %. The 3 % nanosilica addition specimen type cured under elevated conditions produced a statistically insignificant increase in the compressive strength of just over 3 %.

The extracted stress-strain curves, after degradation testing, are shown to the tests extents in Figure 4.12. The static modulus of elasticity was once again taken from the curves using the initial tangent modulus method. A comparison of the static modulus before and after degradation testing is shown in Figure 4.13.

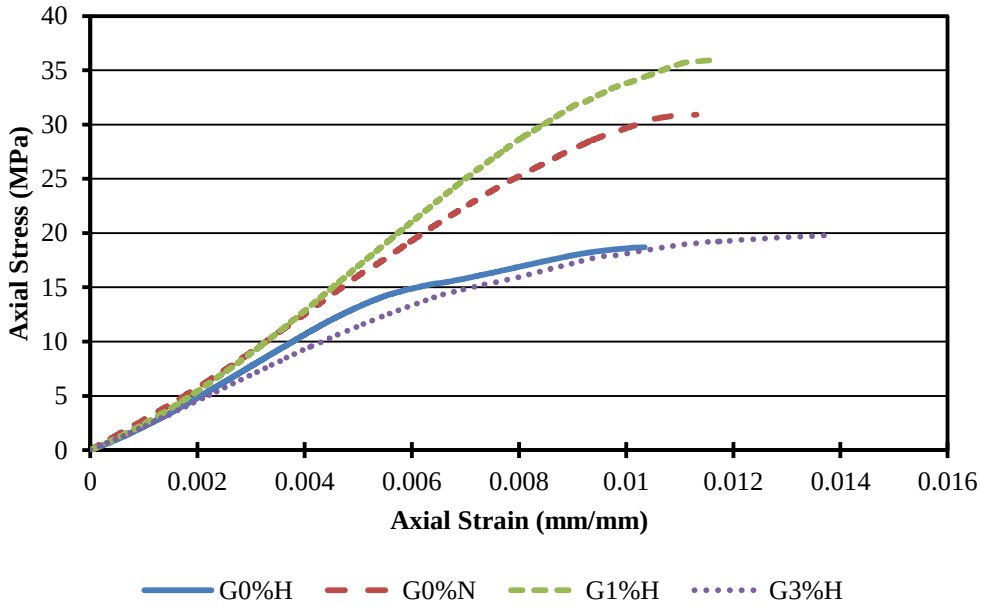

Figure 4.12 Stress-strain curves after degradation

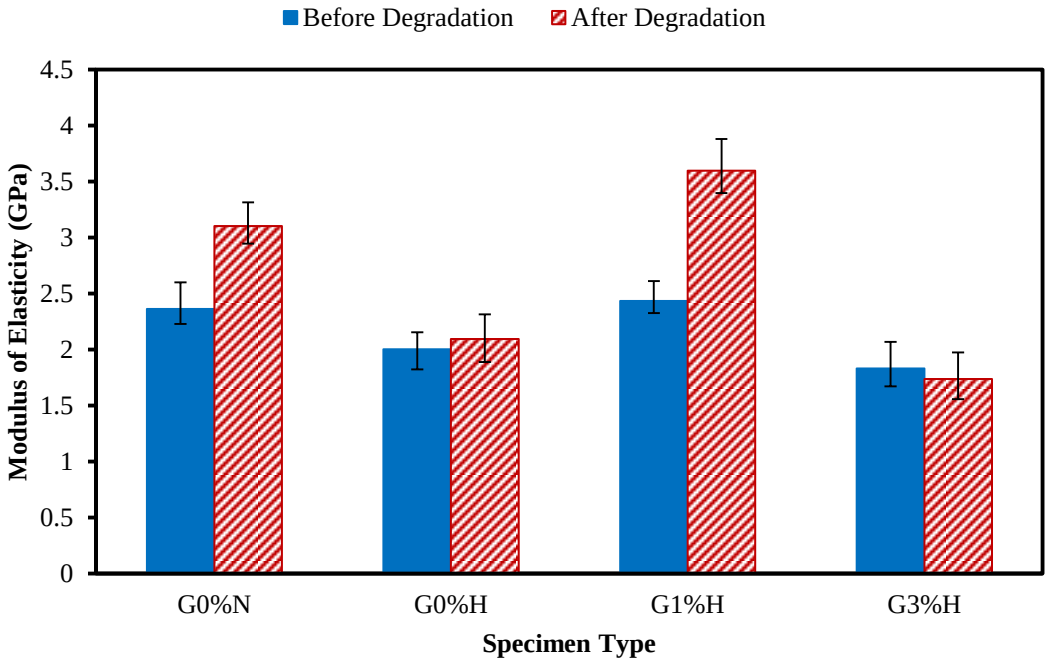

Figure 4.13 Static modulus of elasticity comparison before and after degradation

Neat specimens cured under ambient conditions had a statistically significant increase in modulus of about 31 %. The neat specimen type cured under elevated conditions showed a very slight statistically insignificant increase, less than 5 %, in static modulus of elasticity after degradation testing. Specimens with the 1 % nanosilica addition produced a statistically significant increase in modulus of almost 50 %. Specimens with the 3 % nanosilica addition exhibited a statistically insignificant decrease in modulus of just over 5 %.

Slices of the specimens taken throughout the experiment showed that a dark grey degradation ring formed and progressed inward for the neat specimen type cured under both conditions. However, specimens incorporating 1% and 3% nanosilica displayed no visual degradation or degradation progression. This comparison is presented in Figure 4.14 with the top row being 2-day degradation and the bottom 28-day degradation.

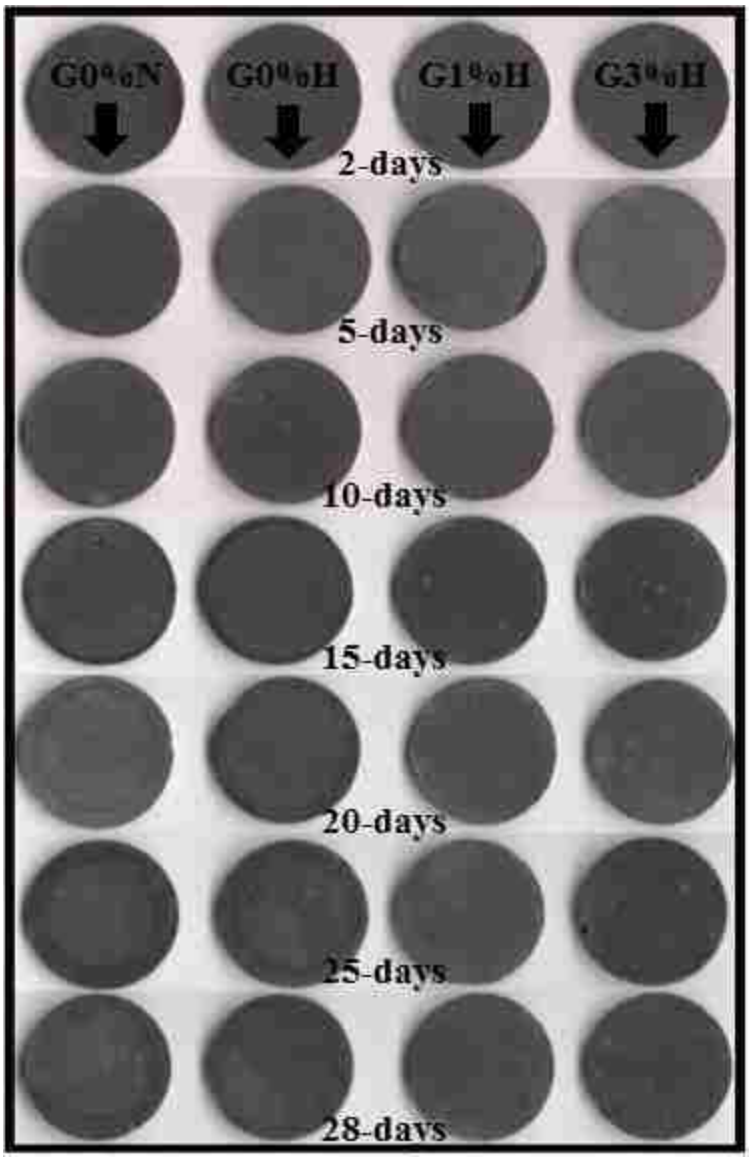

Figure 4.14 Degradation progression comparisons

The rate of degradation advance was calculated from plots of the degradation reaction depth versus time by fitting a straight line to the data; Figure 4.15. The neat specimen type cured under ambient conditions exhibited a degradation advance rate of 0.173 mm/day throughout the entire experiment and the neat specimen type cured under elevated conditions displayed a slightly higher rate of 0.198 mm/day. Both specimen types showed no visual degradation advance until day 10 of the experimentation and then exhibited rapid degradation advance until day 15 at a rate of 0.469 and 0.458 mm/day for the ambient and elevated cured conditions respectively. From day 15 to day 28 the rate

slowed considerably to 0.072 and 0.118 mm/day for the ambient and elevated curing conditions. Specimens incorporating nanosilica are shown as a solid line at the zero mark in the figure as they showed no sign of degradation.

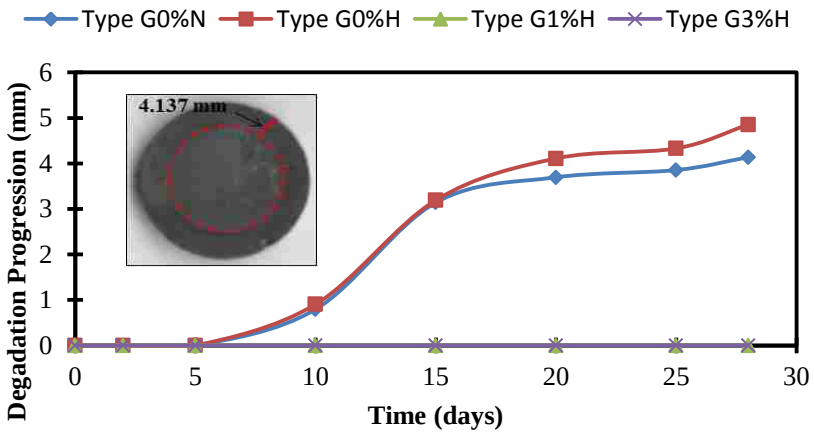

Figure 4.15 Degradation progression for the specimen types

Once again, the 1% nanosilica addition proved to be optimal incorporation percentage. Specimens incorporating 1% nanosilica addition produced a statistically significant increase in modulus of elasticity of almost 50%. Specimens incorporating 3% nanosilica addition exhibited a statistically insignificant decrease in modulus of just over 5%. The increase in the modulus of elasticity can be attributed to the exposure of OWC specimens to a relatively high temperature (50 °C ± 0.2 °C) during carbonated brine degradation. This is explained by the ability of high temperatures to stimulate further cement hydration. The combined observation of damage progression at the surface and the increase in modulus of elasticity might be explained by considering two interacting mechanisms occurring simultaneously: a degradation mechanism that quickly affects the surface and an elevated temperature curing effect that further strengthens the core by producing calcium carbonate. While the above hypothesis might explain the significant increase in modulus of elasticity of the OWC cured under ambient conditions without nanosilica, it cannot explain the increase in OWC specimens including 1% nanosilica and/or cured at high temperature and pressure. Consequently, a microstructural investigation had to be completed in order to further explain the strength, permeability and degradation observations.

4.2 Microstructural Characterization

4.2.1 Nanoindentation

An example loading and unloading rate of the cement paste using the Berkovich indenter is shown in Figure 4.16. The analysis and results are modeled after [Kim et al., 2013]

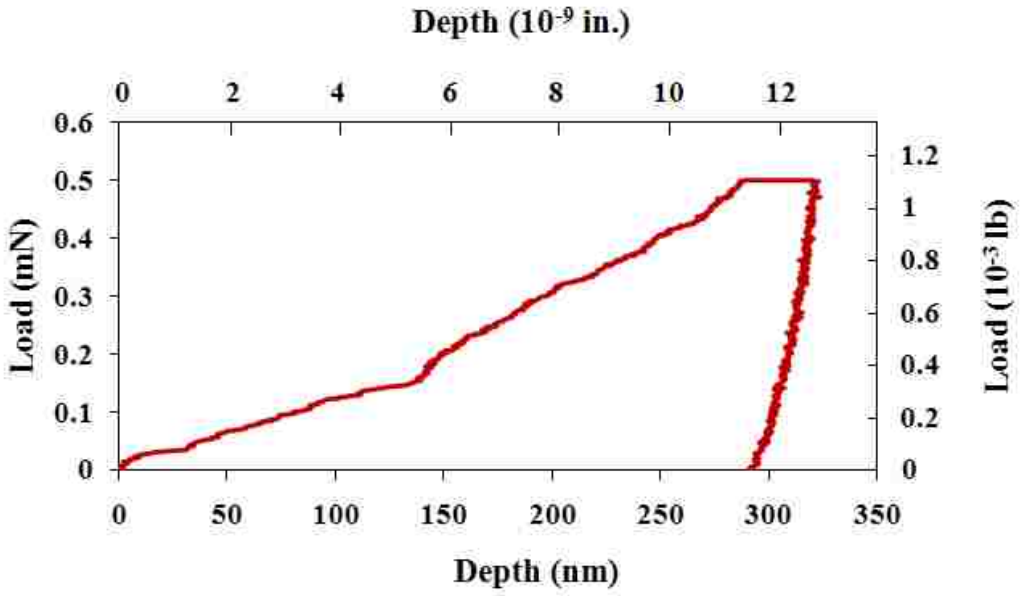

Figure 4.16 Loading-indentation depth of cement paste showing creep during dwell period. Experiments showing kinking at intermediate loading (0.18 mN) which can be used to determine the toughness of cement paste [Reinhart et al., 2010]

The distribution of the modulus of elasticity is deconvoluted using the method described above (Equations (3.2) to (3.10)) and the results are summarized in Table 4.1. The degree of hydration was calculated based on the identified volume fraction of unhydrated cement particles. While microstructural phases identified from our nanoindentation experiments were reported by other researchers [Velez et al., 2001; Ulm et al., 2007; Mondal et al., 2008], the analysis indicated one unknown relatively stiff phase that was not reported in the literature before. This unknown phase appeared only in the cement paste incorporating nanosilica cured under elevated curing conditions as shown in Table 4.1. When this relatively stiff 'new phase' in Table 4.1 is considered, the

degree of hydration calculated from nanoindentation results agrees well with that extracted from the subsequent ^{29}Si MAS NMR. This observation suggests that there might be more sub-microstructural phases than those reported in the literature to be realized using nanoindentation for cement pastes incorporating nanosilica and cured under high temperature and pressure curing conditions.

Table 4.1 Microstructural phase fractions from deconvolution on nanoindentation results

Phases	Ettringite	LD-CSH	HD-CSH	CH	New Phase	Unhydrated cement particle 1	Unhydrated cement particle 2
E range (GPa)	4~6	18~21	28~31	39~43	52~59	53~62	82~119
G0%N	2%	23%	15%	18%	-	34%	8%
G1%N	4%	20%	25%	20%	-	23%	8%
G3%N	2%	16%	20%	21%	-	33%	8%
G0%H	2%	39%	18%	21%	-	14%	6%
G1%H	4%	8%	12%	24%	26%	-	26%
G3%H	4%	14%	20%	28%	8%	-	26%

For the cement pastes cured in elevated conditions for 7 days, LD-C-S-H occupies close to half of the hydration products of the cement paste without nanosilica (G0%H in Table 4.1) while the LD-C-S-H fraction in hydration products of the cement paste incorporating nanosilica decreases significantly and a stiff 'new phase' appears (G1%H and G3%H in Table 4.1). Nanoindentation experiments [Constantinides & Ulm, 2007] elucidated the relationship between packing density and modulus of elasticity of C-S-H. Considering this relationship and colloidal interpretation of C-S-H [Thomas & Jennings, 2006; Powers & Brownyard, 1948], it can be hypothesized that the microstructural phases such as LD-C-S-H (packing density 0.63) can be condensed to HD-C-S-H (packing density 0.76) or very high density (packing density over 0.76) C-S-H under high temperature and pressure curing conditions and with the presence of a rich silica environment (i.e. high content of nanosilica). This might explain the formation of the relatively stiff 'new phase' under these conditions. Further research is warranted at the macroscale to identify the significance of such high levels of silicate connectivity and relatively stiff microstructural phases on the strength and fracture toughness of hydrated cement pastes with nanosilica and elevated curing conditions.

4.2.2 Brunauer-Emmett-Teller (BET) N2 & Barrett-Joyner-Halenda (BJH)

An example of the adsorption/desorption isotherms extracted from each specimen type tested are presented in the subsequent figure along with an example of the corresponding multipoint BET plot. Each specimen type isotherm and corresponding BET plot are displayed in Appendix C. These isotherms show the volume of nitrogen gas, in cm^3/g, being adsorbed and then desorbed in the specimens against the relative pressure observed throughout the experimentation process. The corresponding multipoint BET plots were produced using data points from the appropriate range and then used to determine the *s* and *i* constants, which were then used to calculate the volume of gas adsorbed when the entire surface is covered by a monomolecular layer and finally the specific surface area as described in section 3.8.4.

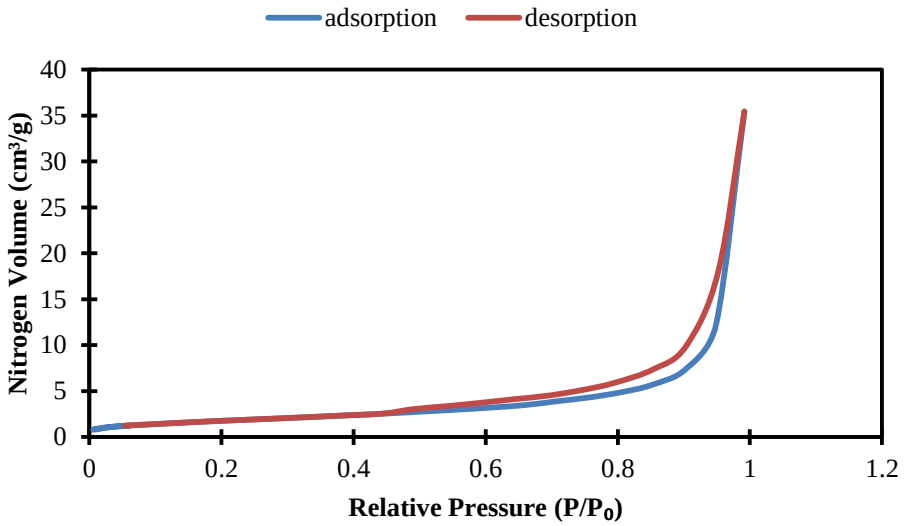

Figure 4.17 Nitrogen adsorption/desorption isotherm neat specimen type (ambient curing)

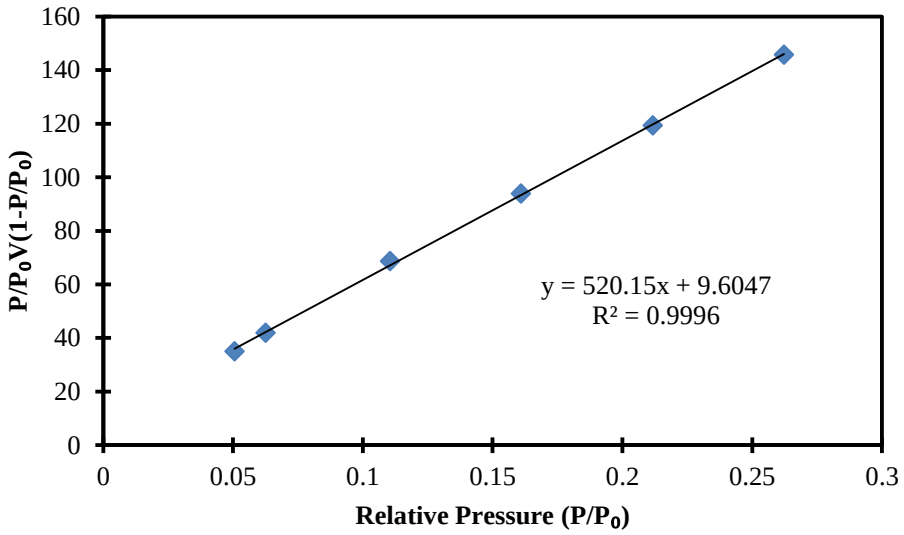

Figure 4.18 BET N2 plot neat specimen type (ambient curing)

The results indicate a type IV isotherm classification for all isotherms produced for the varying specimen types, according to IUPAC recommendations. Type IV isotherms are characteristic of solids having mesopores (2-50 nm) and macropores (> 50 nm) [Aligizaki, 2006]. The sub classification is type H3 which has been reported to describe the case of mesopores structure with very wide capillaries having narrow openings and an interstice between the parallel plates. This sub classification type is also found in adsorption isotherms of many crystalline metal oxide aggregates of sheet-like shape.

The calculated specific surface areas, in m^2/g, for each specimen type are shown in Figure 4.19 to the extent of 1.8 m^2/g.

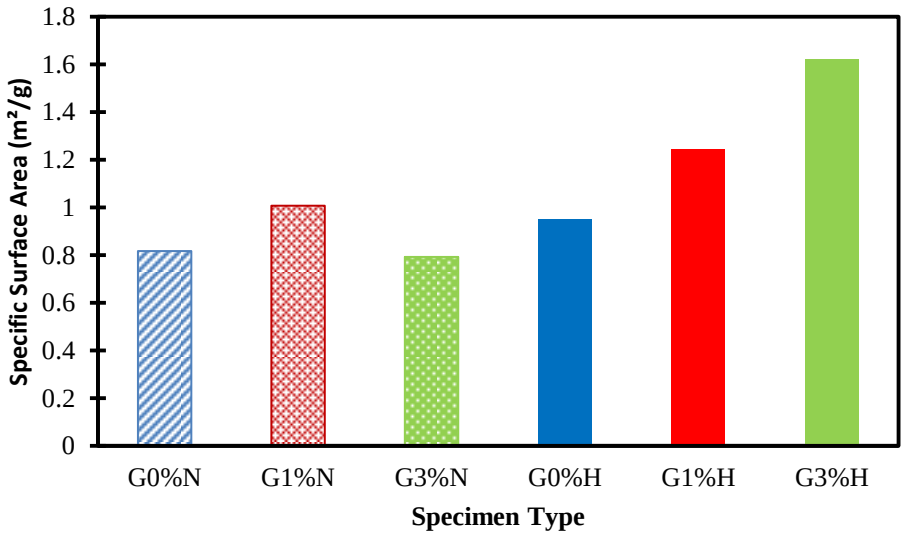

Figure 4.19 Calculated specific surface area for each specimen type

Addition of the nanosilica under ambient curing conditions seems to produce no significant difference, due to the similarity of the results. However, there is a significant trend of significant increase in specific surface area, under elevated curing conditions, with the increasing addition of nanosilica. This directly relates to increased porosity with the increasing addition of nanosilica.

The extracted pore size distribution plots, for each specimen type, are presented in Figure 4.20. The vertical axis is representative of the pore volume, in cm^3/g, and the horizontal axis is the pore diameter in nm. Comparison of the porosity observations showed a decrease in pore volume and peak pore size (pore volume = 0.028 cm^3/g at d_{peak} = 310 nm) for the 1% nanosilica specimens when compared with the OWC without nanosilica cured under elevated conditions (pore volume = 0.053 cm^3/g at d_{peak} = 321 nm). However, specimens incorporating 3% nanosilica exhibited an increase in porosity (pore volume = 0.078 cm^3/g at d_{peak} = 328 nm).

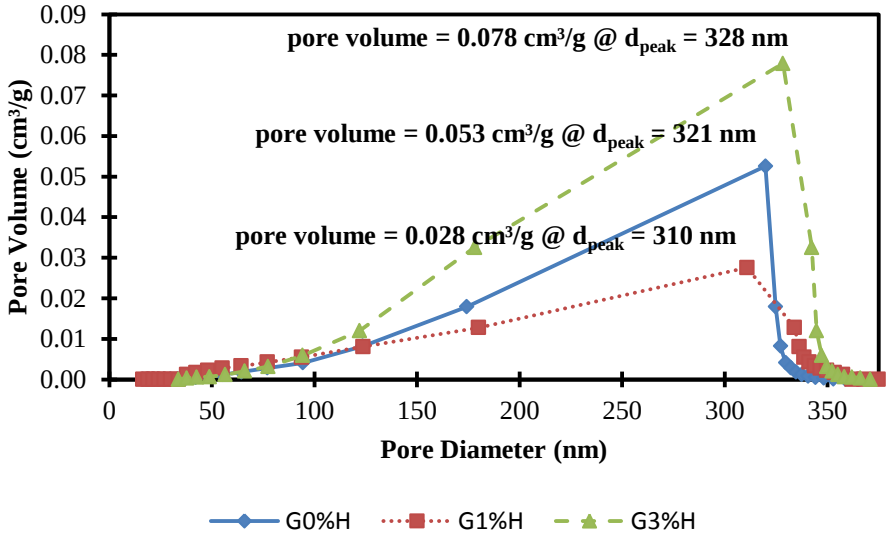

Figure 4.20 Pore size distribution for each specimen type

The BET results revealed that the specific surface area, essentially the total porosity, increased as the nanosilica percentage increased. This response agrees with the 3% nanosilica addition specimen's behavior in the macro experimentation, as demonstrated by the reduced strength and stiffness as well as increased permeability in comparison with the neat specimen type. However, the BET results are contrary for the 1% nanosilica addition specimen type, which excelled in all parts of the macro experimentation. Consequently, it was necessary to produce a pore size distribution for each sample type in order to gain a better understanding of the pore structure characteristics. The pore size distribution revealed that the 1% nanosilica addition specimens had the smallest pore volume and peak pore size in comparison with the neat

and 3% addition, with 3% being the greatest. This means that even though the 1% specimens have a greater total porosity than the neat, the pores are comprised of a reduced distribution of gel and capillary pores that are smaller in total size and volume. The size of the C-S-H gel pores and capillary pores plays an important role and is responsible for the strength and microstructure of cement pastes [Aligizaki, 2006; Thomas & Jennings, 2006]. These results show that nanosilica, in correct incorporation amounts, can significantly enhance the pore microstructure and other corresponding and non-corresponding characteristics of central importance in OWC as further described.

4.2.3 X-Ray Diffraction Analysis (XRDA)

The effects of nanosilica content and altered curing conditions on the cement hydration and pozzolanic activity were examined using XRD analysis. Each resulted XRD spectra was processed using a Fast Fourier Transform (FFT) filter. The differences in the microstructural composition of the Type G OWC pastes, according to the nanosilica content, are compared Figure 4.21 and 4.22 for ambient curing conditions and Figure 4.23 and 4.24 for elevated curing conditions.

As shown in Figure 4.21, more alite (C_3S) and belite (C_2S known as a contributor for late strength of cement pastes) are consumed in hydrated cement pastes incorporating nanosilica under ambient conditions as alite peaks at 32.9˚ (2Θ) and belite peaks at 31˚ (2Θ) decrease in specimens cured under this condition. As shown in Figure 4.22, an intense portlandite (CH) peak at 18.2˚ (2Θ) is apparent in the XRD spectrum of hydrated cement pastes incorporating nanosilica under elevated curing conditions. A comparison of the XRD spectra of 1% and 3% nanosilica incorporated specimens cured under ambient conditions revealed that the quartz (nanosilica) peaks at 25.7˚(2θ) form in the XRD spectrum of the specimens with the 3% addition, while the peaks do not form in specimens with the 1% addition as displayed in Figure 4.22. These results indicate that under ambient curing conditions nanosilica incorporation exceeding 1% do not contribute to the hydration process and consequently remain unreacted. This coincides with the conclusion drawn by other researchers who reported on the necessity to consider a threshold of nanosilica contents to enhance hydrated cement paste properties by

pozzolanic reaction [Kim et al., 2010; Mondal et al., 2010]. A comparison of the XRD spectrum of the 1% and 3% nanosilica incorporated specimens cured under elevated conditions showed that the quartz (nanosilica) peaks are not apparent in both cases. This indicates that the elevated curing environment consumes most of the nanosilica particles. It is also apparent that under elevated curing conditions more alite is consumed for the case of the 3% nanosilica addition. This aspect is represented by the decrease in the alite XRD peaks at 29.2 ˚(2θ) and 32.9 ˚(2θ) for the 3% nanosilica addition in comparison with the 1% as demonstrated in Figure 4.24.

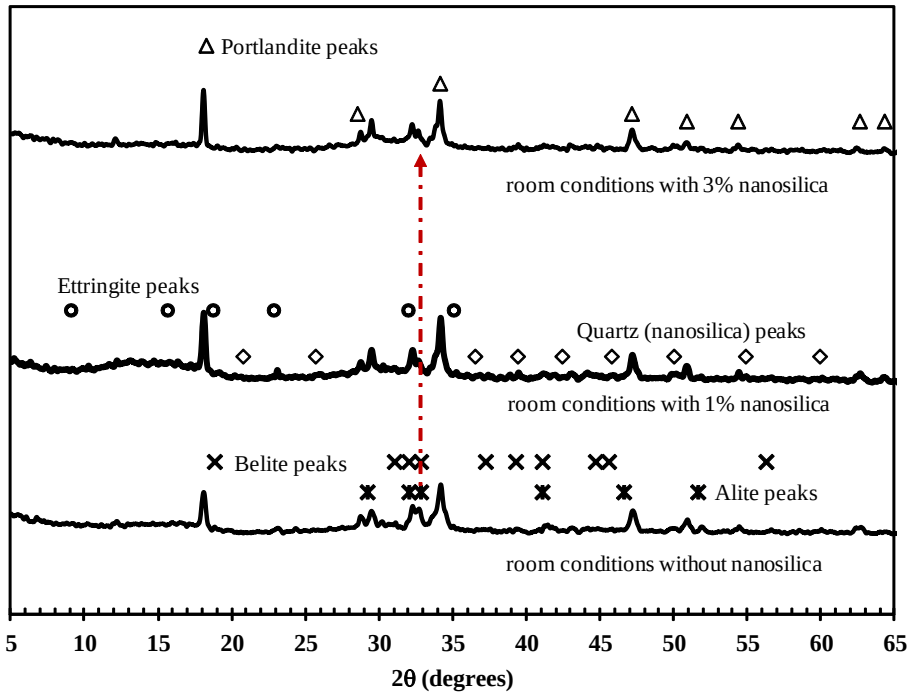

Figure 4.21 Comparison of XRD Spectra of the Hardened Cement Pastes Incorporating 0%, 1% and 3% Nanosilica (Ambient Curing)

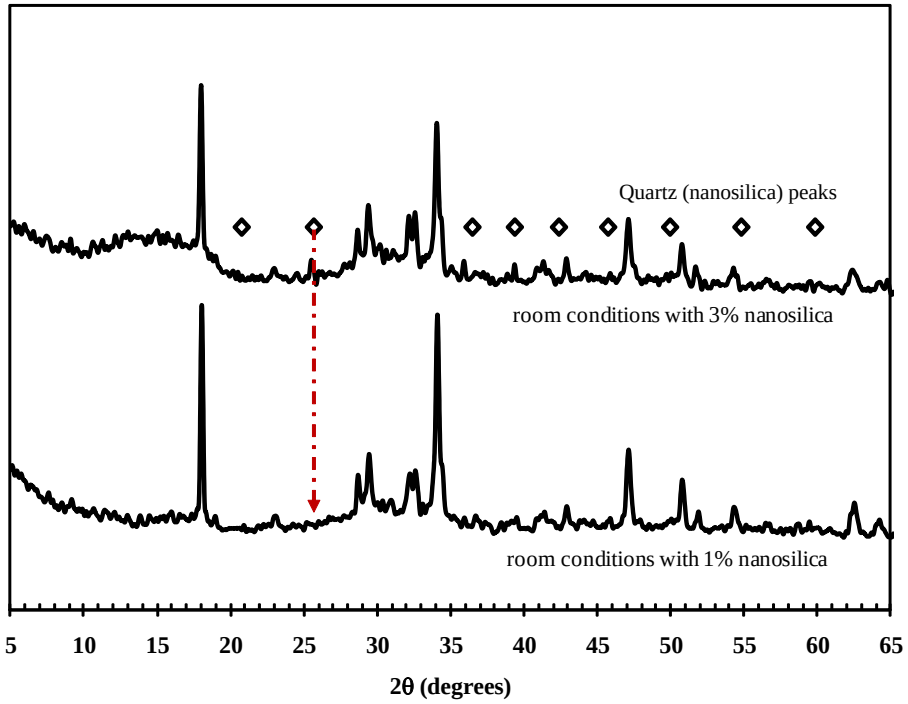

Figure 4.22 Comparison of XRD Spectra of the Hardened Cement Pastes Incorporating 1% and 3% Nanosilica (Ambient Curing)

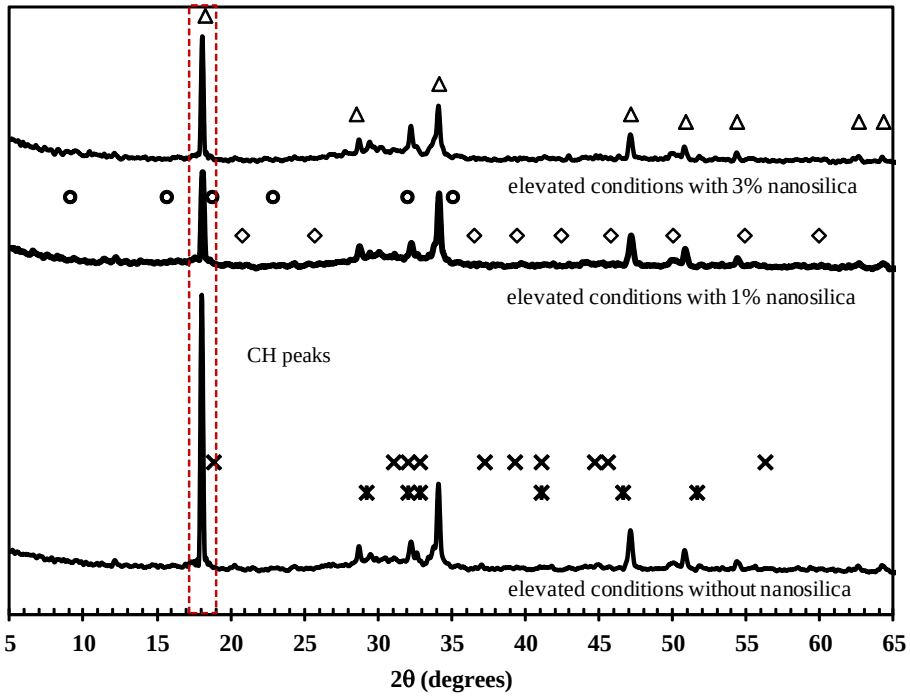

Figure 4.23 Comparison of XRD Spectra of the Hardened Cement Pastes Incorporating 0%, 1% and 3% Nanosilica (Elevated Curing)

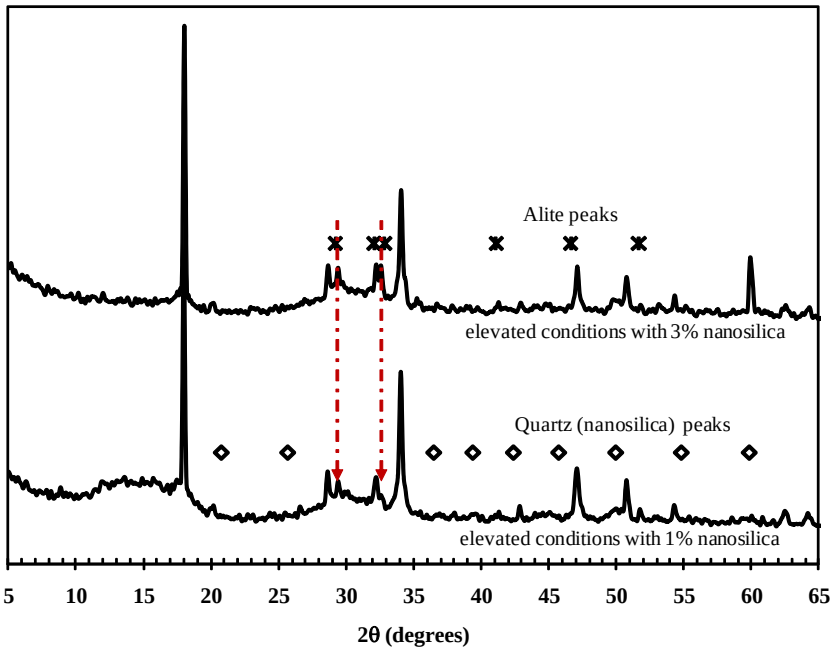

Figure 4.24 Comparison of XRD Spectra of the Hardened Cement Pastes Incorporating 1% and 3% Nanosilica (Elevated Curing)

The effects of curing conditions on the microstructural compositions of the hardened type G OWC without and with the addition of 1% and 3% nanosilica are observed using the corresponding XRD spectra's in Figure 4.25 to 4.27. It is apparent that more alite (C_3S) is consumed under elevated curing conditions as alite peaks at 29.2˚ and 32.9˚ (2Θ) decline in XRD spectra's under the elevated curing conditions. Also, a significantly increased CH peak intensity is observed at 18.2˚ (2Θ) XRD spectra under elevated curing conditions, which is representative of increased hydration and consumption of alite and belite

In Figure 4.27 for specimens incorporating 3% nanosilica, an increase in pozzolanic activity can be observed under elevated curing conditions. This is apparent due to the absence of the 3 quartz (nanosilica) peaks at 25.7˚, 36.5˚ and 45.8˚ (2Θ) from the XRD spectrum of the 3% nanosilica addition specimen type cured under elevated conditions. There is also indication of increased consumption of alite and belite in the

elevated curing conditions, as demonstrated by the disappearance of peaks at 29.2˚ and 31˚ (2Ɵ) respectively.

The results above confirm that the threshold of nanosilica content for effective pozzolanic reactivity appears to increase as the specimens are cured under elevated conditions in comparison with ambient curing conditions. Furthermore, the observed significant increase in the consumption of alite and belite and the higher intensity of CH proves that the hydration of cement is accelerated and augmented when exposed to elevated conditions.

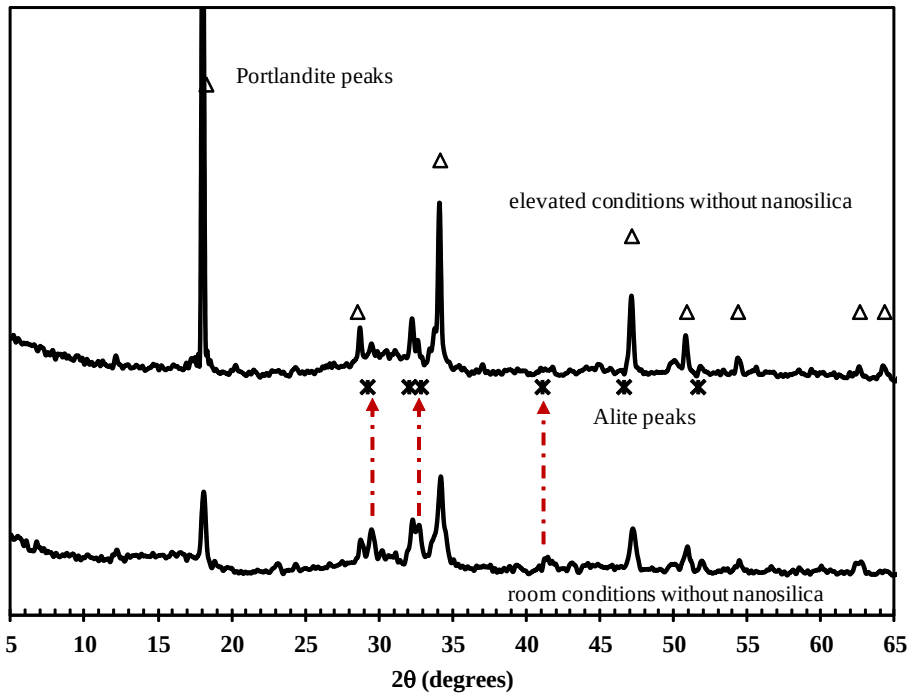

Figure 4.25 Effects of Curing Conditions on Microstructural Compositions by XRD Spectra of the Hardened Cement Pastes without Nanosilica

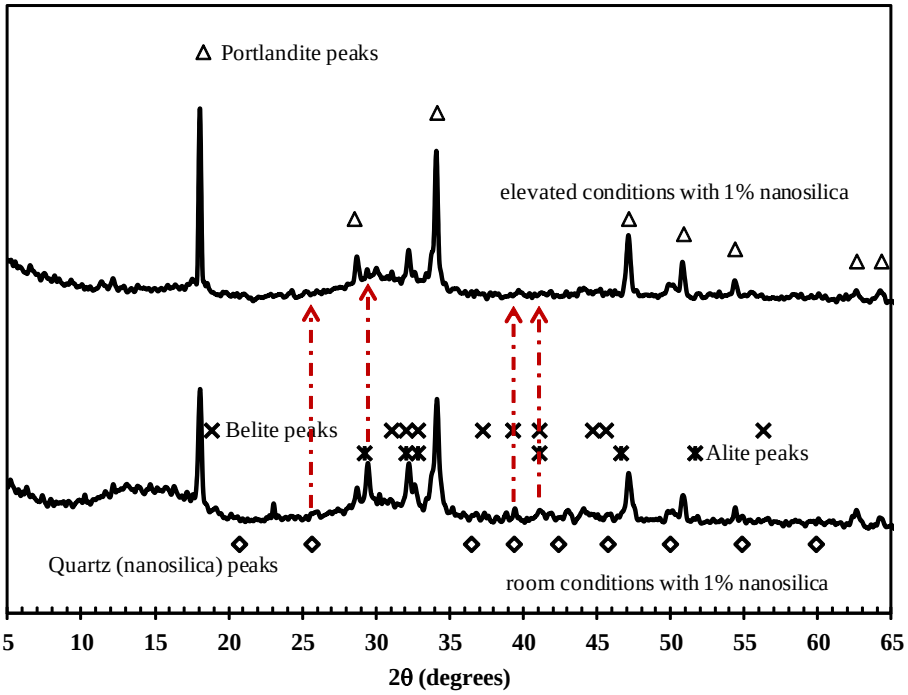

Figure 4.26 Effects of Curing Conditions on Microstructural Compositions by XRD Spectra of the Hardened Cement Pastes Incorporating 1% Nanosilica

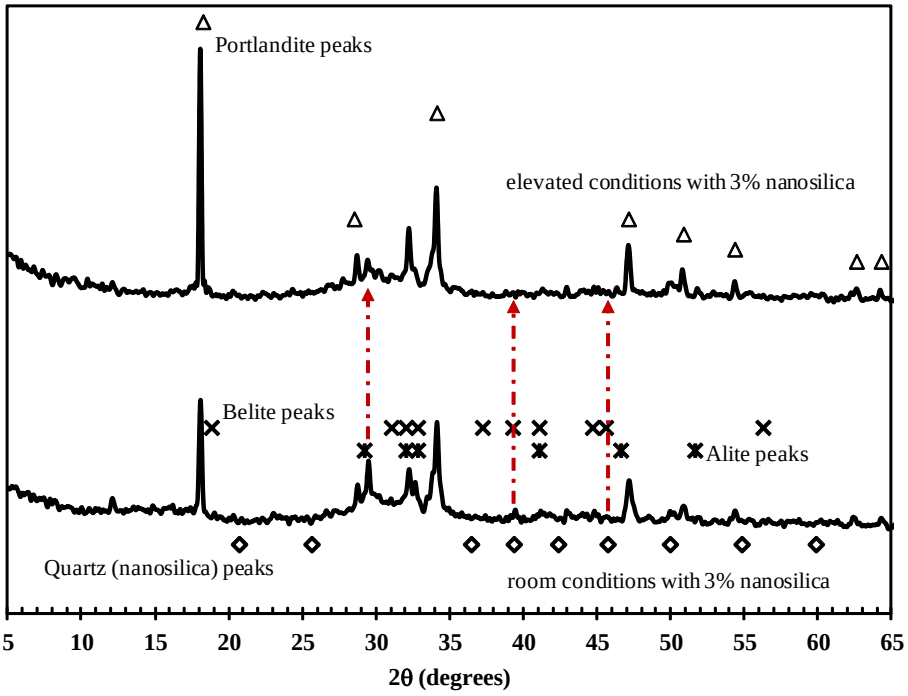

Figure 4.27 Effects of Curing Conditions on Microstructural Compositions by XRD Spectra of the Hardened Cement Pastes Incorporating 3% Nanosilica

XRDA results, after CO_2 exposure, are shown in Figure 4.28. It can be observed that calcium carbonate ($CaCO_3$) peaks at $2\theta = 23^o$ are only distinct in OWC specimens without nanosilica. Peaks located at $2\theta = 23^o$ for specimens incorporating nanosilica were also identified to be for Hatrurite and Brownmillerite as shown in Figure 4.28. The relatively low amount of $CaCO_3$ in OWC with nanosilica can be explained by the low permeability of OWC incorporating nanosilica and the lack of free lime (CH crystals) consumed by nanosilica. It is therefore evident that using nanosilica significantly reduced the carbonation mechanism. The significant increase in modulus of elasticity of OWC specimens without nanosilica cured under ambient conditions can partly be explained by the $CaCO_3$ formation as a result of CO_2 reaction with CH. $CaCO_3$ has a higher modulus of elasticity than CH and CSH. With the relatively low amount of $CaCO_3$, the risk of bicarbonation is significantly reduced when nanosilica is used.

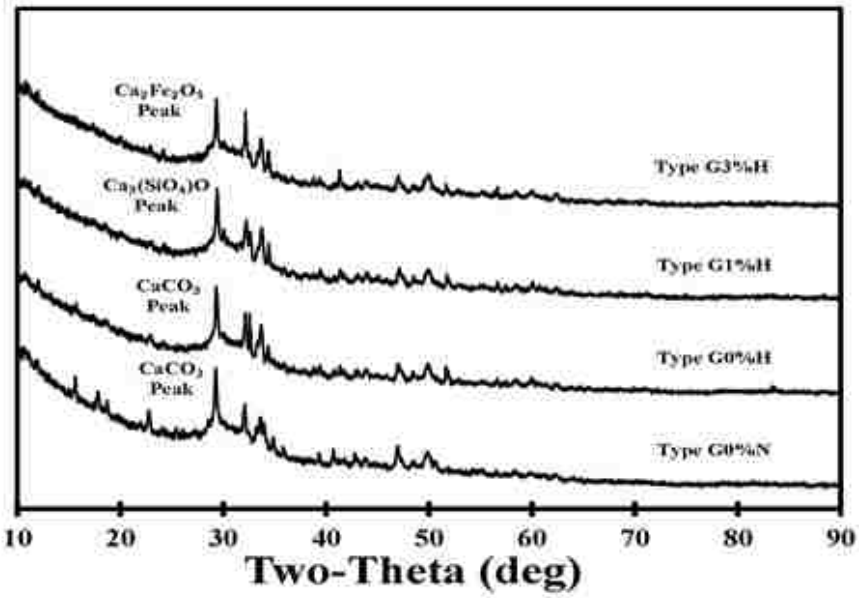

Figure 4.28 XRDA of OWC specimens after carbonated brine exposure

4.2.4 Nuclear Magnetic Resonance (NMR)

The results of ^{29}Si MAS NMR spectra for hardened type G OWC under ambient and elevated conditions, before degradation testing, are presented in Figure 4.29 (a) and (b) respectively. It can be observed that the shape of the chemical shift spectra for the hardened cements hydrated under elevated curing conditions in Figure 4.29 (b) are skewed toward the right side, when compared to that of hardened cements hydrated under ambient curing conditions in Figure 4.29 (a). Consequently, it is apparent that there exists a higher order of silicate polymerization of C-S-H in the hardened cements hydrated under elevated curing conditions in comparison with those hydrated under ambient curing conditions.

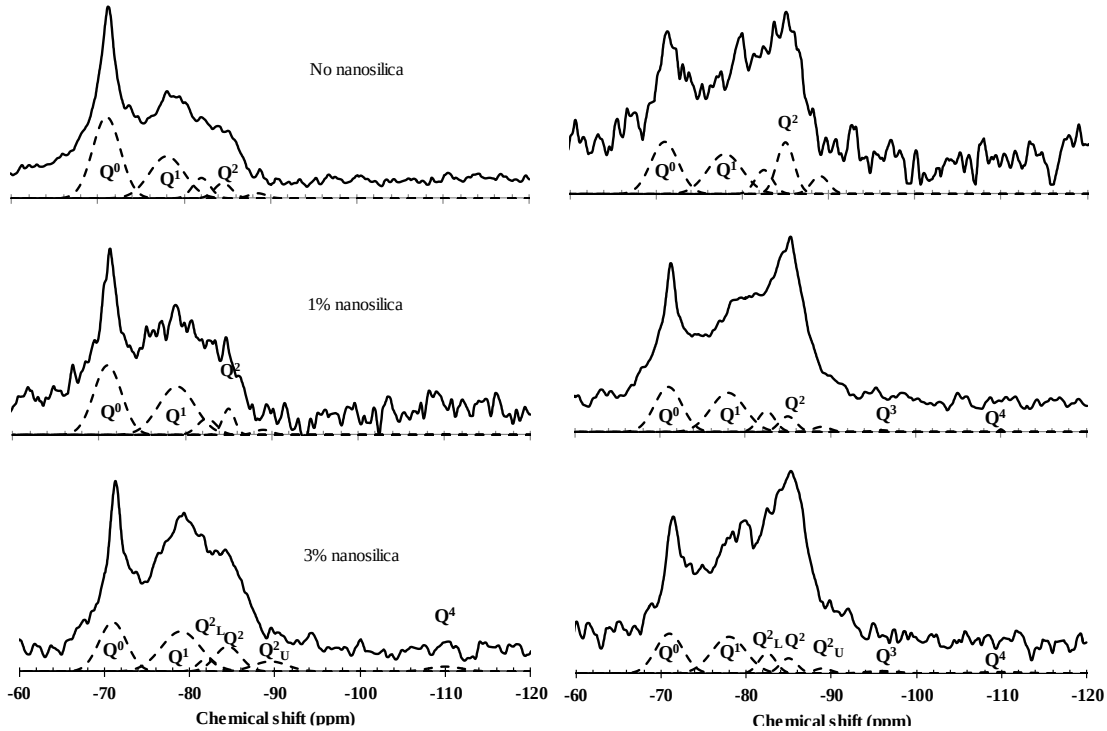

(a) Ambient Condition (b) Elevated Condition

Figure 4.29 ^{29}Si MAS NMR spectra of hardened cement without nanosilica and incorporating 1 % and 3 % nanosilica cured under (a) ambient curing conditions and (b) elevated curing conditions

The integration results of the Q^n intensities by the presented statistical deconvolution are presented in Table 4.2. A slight amount of Q^3 level of polymerization was found in the hardened cements with the 1 % and 3 % nanosilica addition hydrated under elevated conditions for 28 days. This level of polymerization in typically found in the minerals tobermorite and jennite. A slight amount of Q^4 level of polymerization was also found in the hardened cements with 1 % and 3 % nanosilica addition hydrated under both conditions. This is usually representative of the polymerization of quartz which creates a stronger material, as seen in the 1 % nanosilica addition case. The degree of silicate connectivity D_c, the degree of hydration h_c and the degree of pozzolanic reactivity α_s as shown in Table 4.2 were determined using equations (3.17) to (3.33).

Table 4.2 Integration of Q^n intensities by deconvolution of ^{29}Si MAS NMR

Curing	Nanosilica	Q^n (%)					D_c	h_c (%)	α_s (%)
		Q^0	Q^1	Q^2	Q^3	Q^4			
Ambient	0	51.0	33.0	16.0	-	-	1.327	49.4	-
	1%	43.6	39.9	16.2	-	0.3	1.289	55.5	92.9
	3%	31.4	36.7	28.0	-	3.9	1.433	66.6	67.2
Elevated	0	32.3	31.0	36.7	-	-	1.542	70.3	-
	1%	27.6	30.0	41.6	0.7	0.1	1.595	74.3	97.6
	3%	25.1	28.9	42.4	1.9	1.7	1.631	74.7	85.7

The D_c, h_c and α_s of the hardened cement hydrated under elevated curing conditions were higher than those of the hardened cement hydrated under ambient curing conditions. The results show that the elevated curing conditions accelerate the hydration process and pozzolanic reactivity of the cement pastes significantly. Whereas increasing nanosilica percentage increased the degree of silicate connectivity D_c under elevated curing conditions, it did not increase D_c under ambient conditions. This is due to the higher percentage of Q_1 intensity compared to the percentage of Q_2 intensity in the 1 % nanosilica addition specimens cured under ambient conditions. The degree of hydration h_c observed increased as the percentage of nanosilica content increased under ambient and elevated conditions. It is known that silica rich materials, such as fly ash, diminish the heat of hydration due to their low initial activity [Alizadeh & Beaudoin, 2011], though, the pozzolanic reaction is considered an exothermic reaction [Tennis & Jennings, 2000]. The activity of nanosilica is also greater than that of other pozzolanic materials

due to its extremely high surface area in comparison [Kim et al., 2010]. Therefore, the increase in the degree of hydration according to the increase in nanosilica content may be attributed to the increased heat of hydration from the pozzolanic reaction which may accelerate the degree of reactivity of the different cement components.

Furthermore, ^{29}Si MAS NMR was used to examine the polymerization of a silicate tetrahedron in synthetic C-S-H [Lippmma et al., 1980]. The results of 29Si MAS NMR spectra for all specimens before and after degradation were deconvoluted after Saoût et al. (2006). Figure 4.30 compares the NMR spectra and silicate polymerization fraction Q^n [Taylor, 1997] for all OWC specimens before and after degradation. From the figures, it can be observed that Q^0 fraction, which is observed typically in alite (C_3S) and belite (C_2S), decreased significantly after exposure to carbonated brine. Therefore, it is evident that the unhydrated cement components in hydrated cement pastes react with CO_2 and produce calcium carbonate. One can also observe an increase of Q^2 (the middle chain of C-S-H layer) over Q^1 (the end chain of C-S-H) fractions after carbonated brine exposure. This increase is observed in all OWC specimens with and without nanosilica. The formation of Q^2 might occur due to CO_2 reaction with C-S-H forming calcium carbonates and thus connecting two C-S-H layers. There is a slight in Q^3 and Q^4 as well. High level polymerization can happen due to combining multi layers in C-S-H.

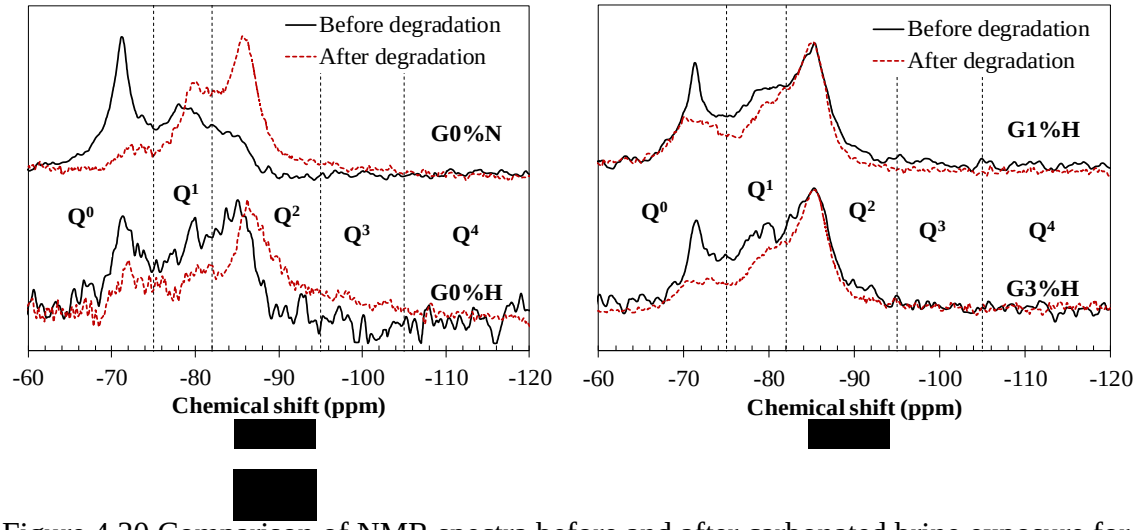

Figure 4.30 Comparison of NMR spectra before and after carbonated brine exposure for OWC specimens (a) G0%N vs. G0%H (b) G1%H and G3%H

NMR observations indicate that carbonated brine exposure of OWC can lead to forming high degree of silicate polymerization Q^2 and typically non-observed Q^3 and Q^4 in OWC specimens. The change of Q^0 to high order polymerized silicate might be able to explain the increase in the modulus of elasticity of OWC specimens incorporating 1% nanosilica. The significance of increasing polymerized silicate with Q^2, Q^3 and Q^4 content compared with Q^0 and Q^1 on the modulus of elasticity of cement needs to be further investigated. It is important to note that increasing silicate polymerization increases brittleness and thus the chance of cracking under thermal stress fluctuation in deep oil wells. The significant increase in porosity of OWC specimens incorporating 3% nanosilica might explain the limited change in its modulus of elasticity in spite the increase in its silicate polymerization.

Chapter 5 Recommendations & Conclusions

5.1 Summary

Compression testing showed that the 1% addition of nanosilica produced statistically significant increases in the compressive strength and modulus of elasticity, under both curing conditions. The 3% nanosilica addition produced insignificant changes in the compressive strength and modulus of elasticity in contrast with the neat. This is most likely attributed to the low workability of the 3% nanosilica addition which only showed a flow of 34%, in flowability tests, in comparison with 150% flow for the neat and 1% mixes. The low workability entrapped air in the specimens during casting and created an imperfect final product with added voids. Therefore, the 3% nanosilica addition experienced a minor reduction in strength and stiffness in comparison with the neat specimens.

Rapid chloride-ion penetration test (RCPT) results revealed that the 1% nanosilica addition again enhanced the specimen's performance requirements in regards to permeability and the 3% nanosilica addition made the specimens slightly more permeable. These results are in agreement with the compressive strength testing results and they further reaffirm that the 1% nanosilica addition creates a denser material composition with diminished voids and the 3% addition does the contrary.

Strength and stiffness and degradation progression testing after degradation due to exposure to CO_2 showed that the 1% nanosilica addition proved to be optimal incorporation percentage. Specimens incorporating the 1% nanosilica addition produced a statistically significant increase in modulus of elasticity. Specimens incorporating 3% nanosilica addition exhibited a statistically insignificant decrease in modulus. The increase in the modulus of elasticity can be attributed to the exposure of oil well cement (OWC) specimens to a relatively high temperature (50 °C ± 0.2 °C) during carbonated brine degradation. This is explained by the ability of high temperatures to stimulate further cement hydration. The combined observation of damage progression at the surface and the increase in modulus of elasticity might be explained by considering two interacting mechanisms occurring simultaneously: a degradation mechanism that quickly

affects the surface and an elevated temperature curing effect that further strengthens the core by producing calcium carbonate. While the above hypothesis might explain the significant increase in modulus of elasticity of the OWC cured under ambient conditions without nanosilica, it cannot explain the increase in OWC specimens including 1% nanosilica and/or cured at high temperature and pressure. Consequently, a microstructural investigation had to be completed in order to further explain the strength, permeability and degradation observations.

The Brunauer-Emmett-Teller (BET) results revealed that the specific surface area, essentially the total porosity, increased as the nanosilica percentage increased. This response agrees with the 3% nanosilica addition specimen's behavior in the macro experimentation, as demonstrated by the reduced strength and stiffness as well as increased permeability in comparison with the neat specimen type. However, the BET results are contrary for the 1% nanosilica addition specimen type, which excelled in all parts of the macro experimentation. Consequently, it was necessary to produce a pore size distribution for each sample type in order to gain a better understanding of the pore structure characteristics. The pore size distribution revealed that the 1% nanosilica addition specimens had the smallest pore volume and peak pore size in comparison with the neat and 3% addition, with 3% being the greatest. This means that even though the 1% specimens have a greater total porosity than the neat, the pores are comprised of a reduced distribution of gel and capillary pores that are smaller in total size and volume. The size of the calcium silicate hydrate (C-S-H) gel pores and capillary pores plays an important role and is responsible for the strength and microstructure of cement pastes [Aligizaki, 2006; Thomas & Jennings, 2006].

The X-ray diffraction analysis (XRDA) results indicate that under ambient curing conditions, nanosilica incorporation exceeding 1% does not contribute to the hydration process and consequently remains unreacted. This coincides with the conclusion drawn by other researchers who reported on the necessity to consider a threshold of nanosilica contents to enhance hydrated cement paste properties by pozzolanic reaction [Kim et al., 2010; Mondal et al., 2010]. A comparison of the XRD spectrum of the 1% and 3% nanosilica incorporated specimens cured under elevated conditions showed that the

quartz (nanosilica) peaks are not apparent in both cases. This indicates that the elevated curing environment consumes most of the nanosilica particles. It is also apparent that under elevated curing conditions more alite is consumed for the case of the 3% nanosilica addition. This aspect is represented by the decrease in the alite XRD peaks for the 3% nanosilica addition in comparison with the 1%. The XRDA results also confirmed that the threshold of nanosilica content for effective pozzolanic reactivity appears to increase as the specimens are cured under elevated conditions in comparison with ambient curing conditions. Furthermore, the observed significant increase in the consumption of alite and belite and the higher intensity of calcium hydroxide (CH) proves that the hydration of cement is accelerated and augmented when exposed to elevated conditions.

The XRDA results, after CO_2 exposure, showed that the calcium carbonate ($CaCO_3$) peaks are only distinct in OWC specimens without nanosilica. The relatively low amount of $CaCO_3$ in OWC with nanosilica can be explained by the low permeability of OWC incorporating nanosilica and the lack of free lime (CH crystals) consumed by nanosilica. It is therefore evident that using nanosilica significantly reduced the carbonation mechanism. The significant increase in modulus of elasticity of OWC specimens without nanosilica cured under ambient conditions can partly be explained by the $CaCO_3$ formation as a result of CO_2 reaction with CH. $CaCO_3$ has a higher modulus of elasticity than CH and CSH. With the relatively low amount of $CaCO_3$, the risk of bicarbonation is significantly reduced when nanosilica is used.

The nuclear magnetic resonance (NMR) results revealed that the D_c, h_c and α_s of the hardened cement hydrated under elevated curing conditions were higher than those of the hardened cement hydrated under ambient curing conditions. The results showed that the elevated curing conditions accelerate the hydration process and pozzolanic reactivity of the cement pastes significantly. Whereas increasing nanosilica percentage increased the degree of silicate connectivity D_c under elevated curing conditions, it did not increase D_c under ambient conditions. This is due to the higher percentage of Q_1 intensity compared to the percentage of Q_2 intensity in the 1% nanosilica addition specimens cured under ambient conditions. The degree of hydration h_c observed increased as the percentage of nanosilica content increased under ambient and elevated conditions. It is

known that silica rich materials, such as fly ash, diminish the heat of hydration due to their low initial activity [Alizadeh & Beaudoin, 2011], though, the pozzolanic reaction is considered an exothermic reaction [Tennis & Jennings, 2000]. The activity of nanosilica is also greater than that of other pozzolanic materials due to its extremely high surface area in comparison [Kim et al., 2010]. Therefore, the increase in the degree of hydration according to the increase in nanosilica content may be attributed to the increased heat of hydration from the pozzolanic reaction which may accelerate the degree of reactivity of the different cement components.

The NMR observations, after CO_2 exposure, indicated that carbonated brine exposure of OWC can lead to forming a high degree of silicate polymerization Q^2 and typically non-observed Q^3 and Q^4 in OWC specimens. The change of Q^0 to high order polymerized silicate might be able to explain the increase in the modulus of elasticity of OWC specimens incorporating 1% nanosilica. The significance of increasing polymerized silicate with Q^2, Q^3 and Q^4 content compared with Q^0 and Q^1 on the modulus of elasticity of cement needs to be further investigated. It is important to note that increasing silicate polymerization increases brittleness and thus the chance of cracking under thermal stress fluctuation in deep oil wells. The significant increase in porosity of OWC specimens incorporating 3% nanosilica might explain the limited change in its modulus of elasticity in spite the increase in its silicate polymerization.

5.2 Conclusions

Taking all of the above summarized results into account, one can begin to draw conclusions about the effects on nanosilica integration in OWC. All of the macroscale experimentation results showed that nanosilica incorporation in Type G OWC had adverse effects of significance, in regards to the stringent performance requirements established in the industry. The incorporation of 1% nanosilica proved to be ideal throughout macroscale experimentation, as increases in strength, stiffness, resistance to chloride penetration, degradation penetration resistance and degradation strength and stiffness were observed. While conversely, the 3% nanosilica addition exhibited contrasting undesirable effects. This aspect agrees with the hypothesis that the

incorporation of nanosilica in OWC can provide significant enhancements in regards to the performance, when incorporated at appropriate levels.

In order to explain the enhancements produced in the 1% nanosilica incorporated specimens, the pore structure of each specimen type was analyzed. The results revealed that the 1% nanosilica addition created a reduced pore size distribution and an improved pore structure. The results from the 3% nanosilica addition produced a composition with an enlarged pore size distribution and pore structure. As described in the text, pore structure and size distribution plays a vital role in the strength and microstructure of cementitious materials. This is evident from the macroscale results which show that the specimens with the 1% nanosilica incorporation have the smallest pore size distribution, but have the greatest strength, stiffness and resistance to degradation. Whereas the specimens with the 3% nanosilica addition have the largest pore size distribution and least amount of strength, stiffness and permeability resistance.

Furthermore, microstructural characterization experimentation was implemented to explain how nanosilica transformed the pore structure and attributing factors of importance in the OWC samples. It was also used to further explain the results of the degradation due to CO_2 exposure testing.

The XRDA results showed that when nanosilica was incorporated at 1% it fully reacts and contributes to the hydration process. The 3% nanosilica addition exhibited unreacted nanosilica that did contribute to the hydration process. The results also showed that the threshold of nanosilica content for effective pozzolanic reactivity appears to increase as the specimens are cured under elevated conditions in comparison with ambient curing conditions. The XRDA results, after CO_2 exposure, showed that calcium carbonate peaks are only present in specimens without nanosilica. The relatively low amount of $CaCO_3$ found in OWC with nanosilica can be explained by the low permeability of OWC incorporating nanosilica and the lack of free lime (CH crystals) consumed by the nanosilica. It is therefore apparent that using nanosilica significantly reduced the carbonation mechanism. With the relatively low amount of $CaCO_3$, the risk of bicarbonation is significantly reduced when nanosilica is used. The above summarized

results agree with the pore structure characterization and the macroscale experimentation results. When nanosilica is incorporated at the appropriate level, in this case 1%, it contributes to the hydration process and pozzolanic reactivity. This incorporation modifies the hydration byproduct by fully reacting with the Type G OWC to form a dense composition with an enhanced pore structure and performance as demonstrated above. Nanosilica incorporation also produced a resistance to degradation by CH consumption that produced a reduced risk of bicarbonation.

The NMR results showed that the elevated curing conditions accelerate the hydration process and pozzolanic reactivity of the cement pastes significantly. Whereas increasing nanosilica percentage increased the degree of silicate connectivity under elevated curing conditions, it did not under ambient conditions. The degree of hydration observed increased as the percentage of nanosilica content increased under ambient and elevated conditions. The increase in the degree of hydration according to the increase in nanosilica content may be attributed to the increased heat of hydration from the pozzolanic reaction which may accelerate the degree of reactivity of the different cement components. The NMR results, after CO_2 exposure, revealed that carbonated brine exposure of OWC can lead to the formation of a high degree of silicate polymerization. The change of Q^0 to a high order polymerized silicate might explain the increase in the modulus of elasticity of OWC specimens incorporating 1% nanosilica.

5.3 Recommendations

To conclude, the incorporation of nanosilica in Type G OWC, at the appropriate levels, transforms the microstructure and hydration process and is recommended to be incorporated in industrial applications. This manufactured composition demonstrated improvements in strength and stiffness, permeability and resistance to degradation due to CO_2 exposure. The composition remains comparably flowable and exceeds the industries performance requirements. Further research is necessary to determine the ideal incorporation percentage and to investigate alternative nano materials currently being used in research.

Appendix A – RCPT Analysis Matlab Code

A-1. Example No. 1

```
% This M-file evaluates the cache data for Lincoln log structures
% to find a proper solution for a specific case

clear all
close all
clc

Data1=[0 0 0 0];

files = dir('*.dat');

for i=1:length(files)
    %eval(['load ' files(i).name ' -ascii']);
    %eval(['import ' files(i).name '.*' ]);
    %eval(['importdata ' files(i).name]);
    Data2=importdata(files(i).name);
    Data1=[Data1; Data2];
end

Data3=Data1.*(5/2^16);
f=length(Data3)/21600;
Data4=Data3(1:f:length(Data3),:);

for j=1:4
Results(j)=sum(Data4(:,j));
end

plot(Data4);
```

Appendix B – Constants (Taylor 1987)

Table B-1. Constants (Taylor 1987) and proportions of cement components for Type G oil well cement (OWC).

Components	*A*	*b*	*c*	*p*
C_3S	0.25	0.9	0.70	0.512
C_2S	0.46	0	0.12	0.27
C_3A	0.28	0.9	0.77	0.023
C_4AF	0.26	0.9	0.55	0.144

Appendix C – Isotherms & Corresponding BET Plots

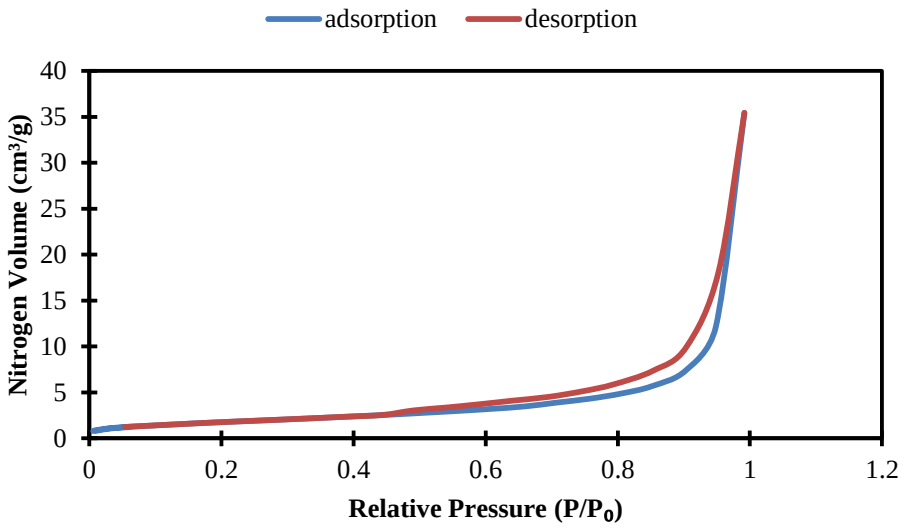

Figure C-1 Nitrogen adsorption/desorption isotherm neat specimen type (ambient curing)

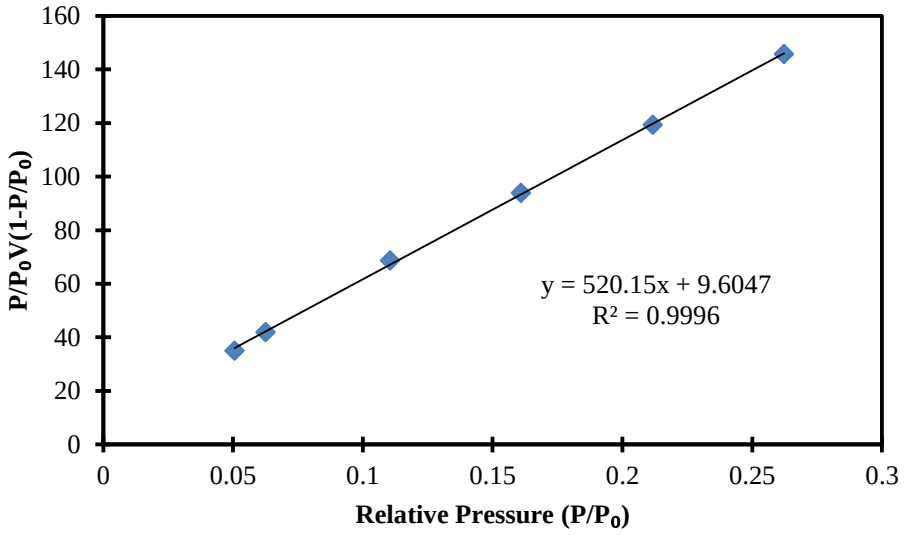

Figure C-2 BET N2 plot neat specimen type (ambient curing)

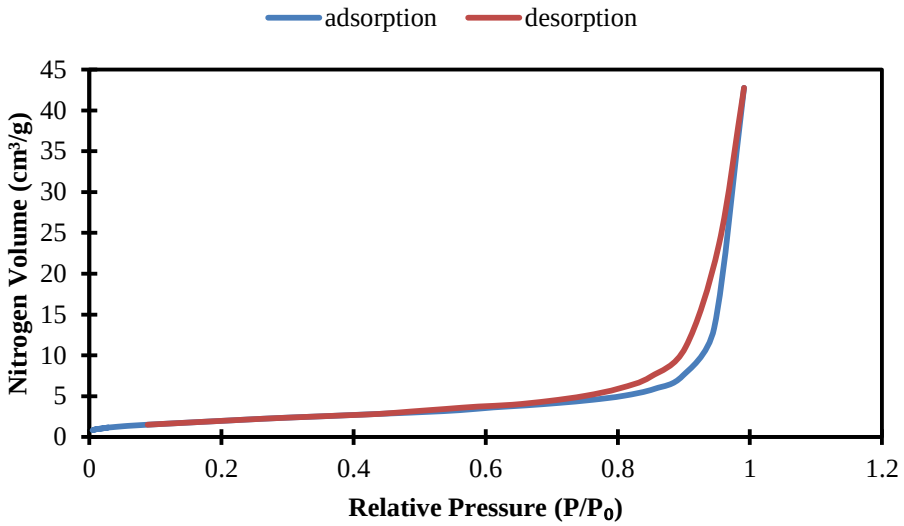

Figure C-3 Nitrogen adsorption/desorption isotherm neat specimen type (elevated)

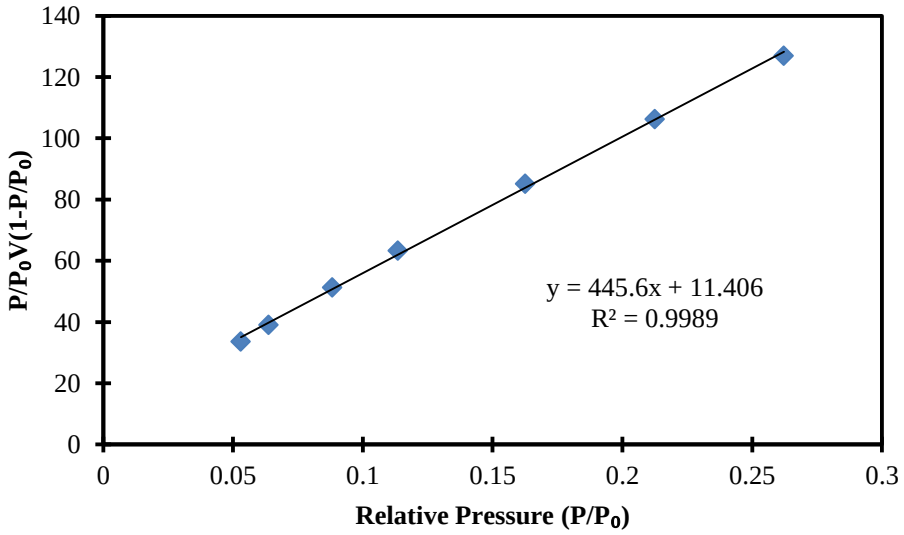

Figure C-4 BET N2 plot neat specimen type (elevated curing)

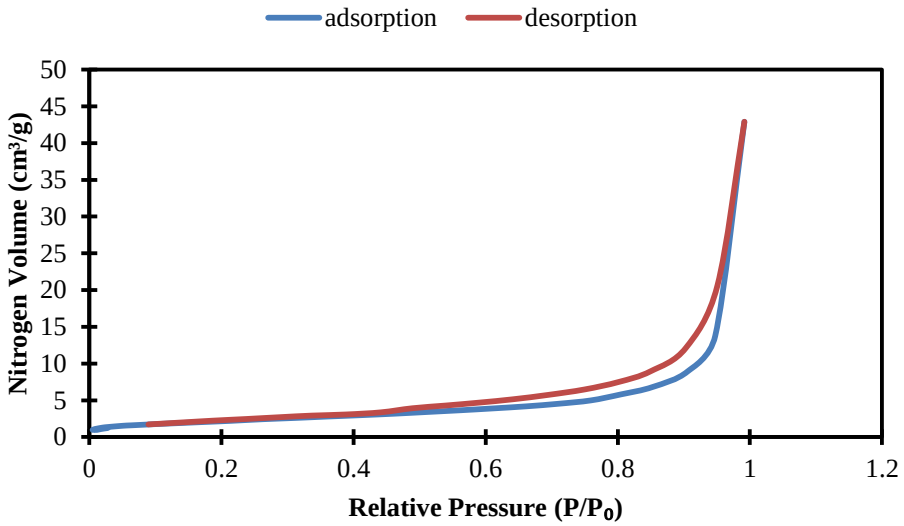

Figure C-5 Nitrogen adsorption/desorption isotherm 1% addition (ambient curing)

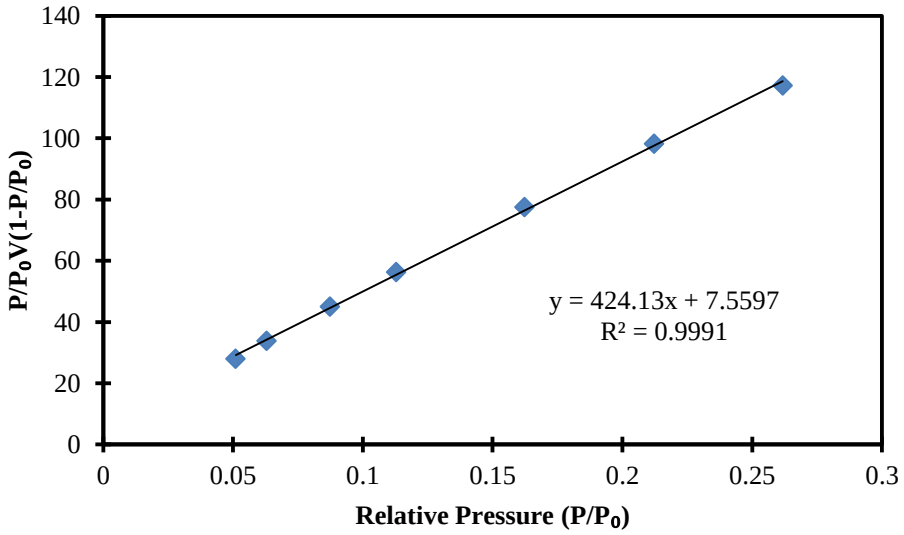

Figure C-6 BET N2 plot 1% nanosilica addition (ambient curing)

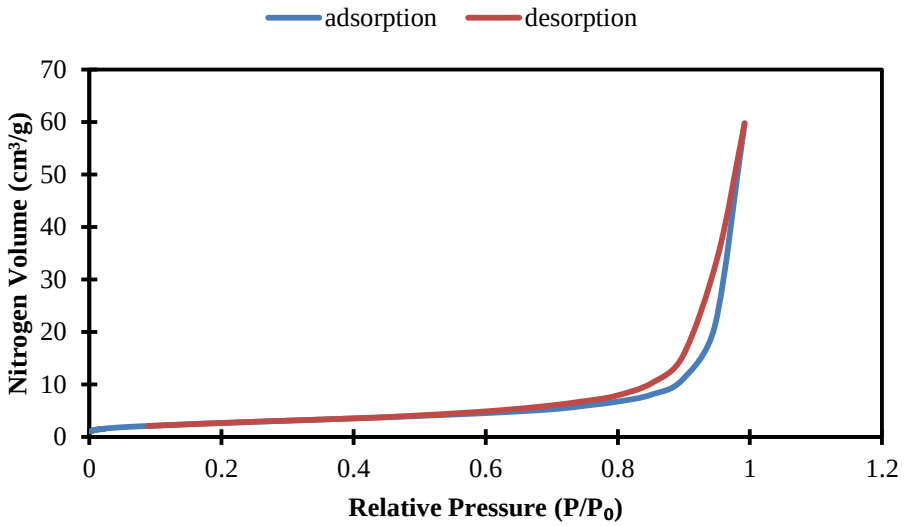

Figure C-7 Nitrogen adsorption/desorption isotherm 1% addition (elevated curing)

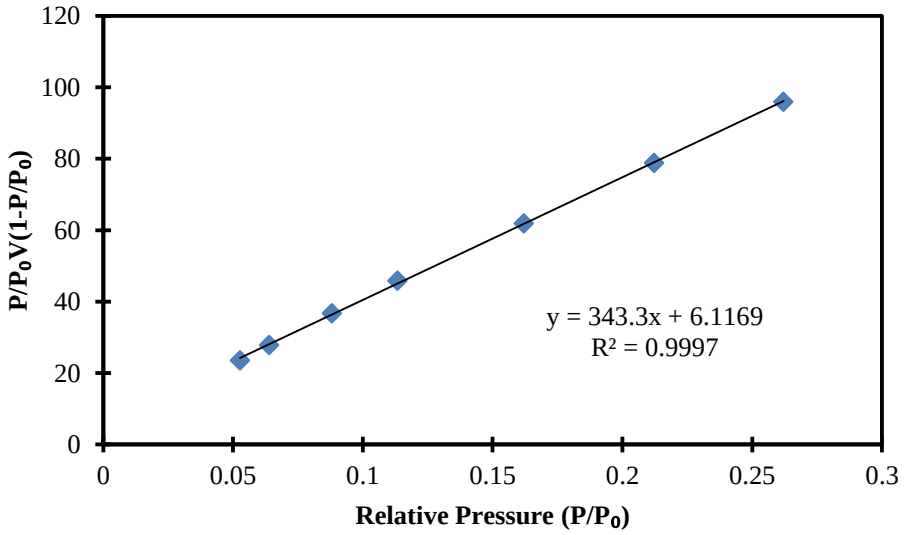

Figure C-8 BET N2 plot 1% nanosilica addition (elevated curing)

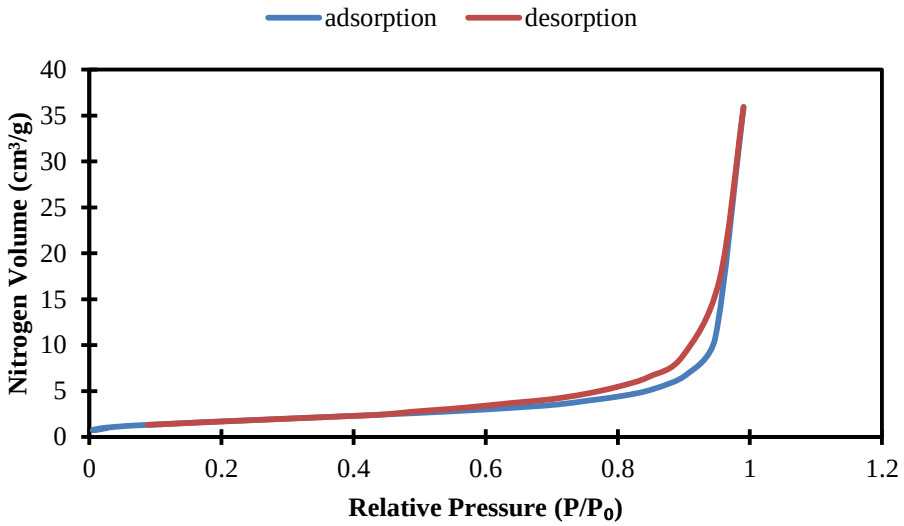

Figure C-9 Nitrogen adsorption/desorption isotherm 3% addition (ambient curing)

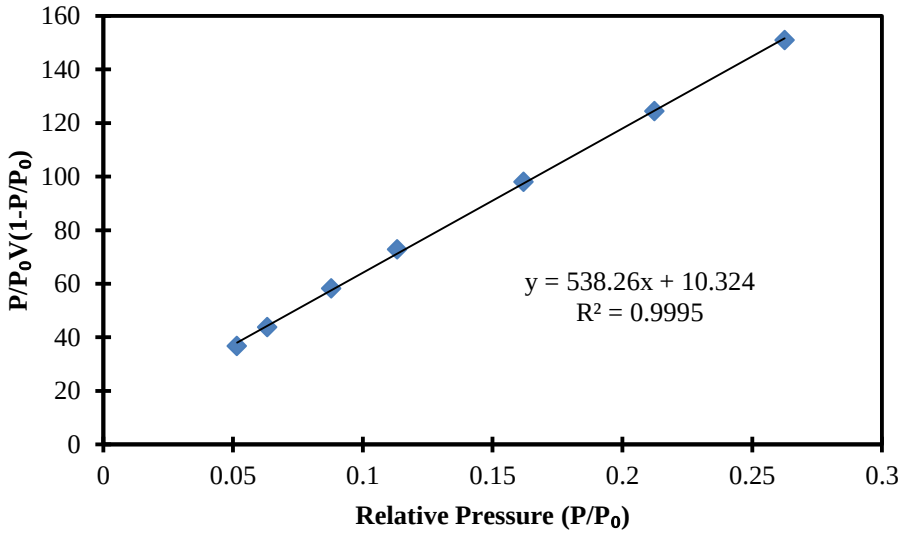

Figure C-10 BET N2 plot 3% nanosilica addition (ambient curing)

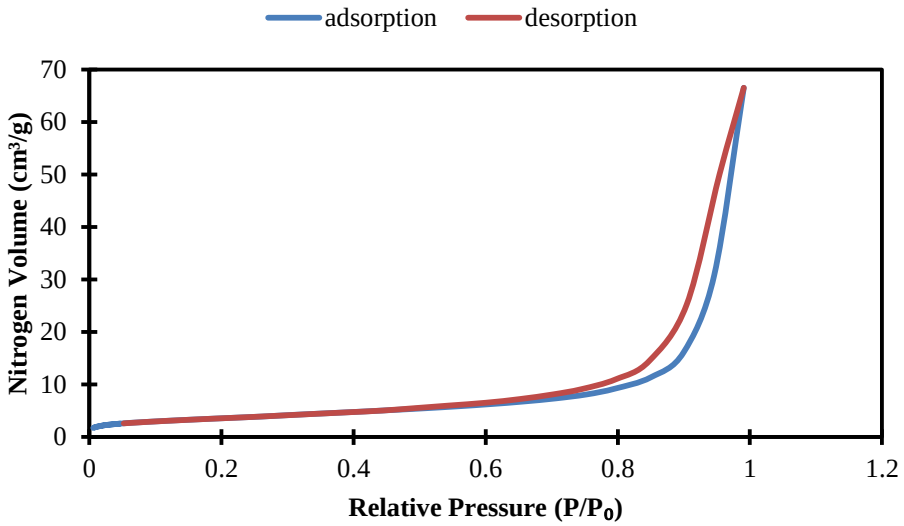

Figure C-11 Nitrogen adsorption/desorption isotherm 3% addition (elevated curing)

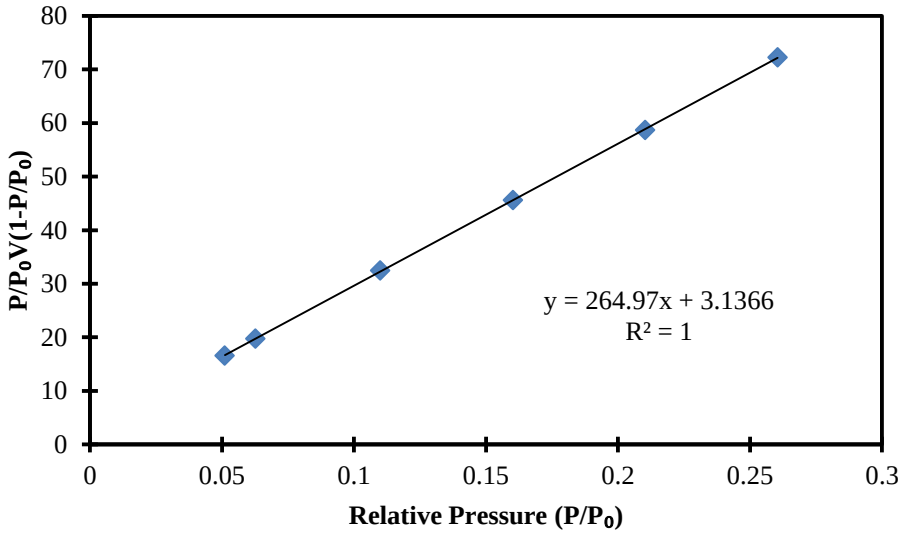

Figure C-12 BET N2 plot 3% nanosilica addition (elevated curing)

References

Aligizaki, K.K. (2006). *Pore Structure of Cement Based Materials*: Taylor & Francis, New York, NY.

Alizadeh, R. (2009). "Nanostructure and engineering properties of basic and modified calcium-silicate-hydrate systems." *Department of Civil Engineering*. Ottawa, University of Ottawa. Doctor of Philosophy in Civil Engineering: 231.

Alizadeh, R., and Beaudoin, J.J. (2011). "Mechanical properties of calcium silicate hydrates." *Materials and Structures*, 44: 13–28.

Alizadeh, R., J.J. Beaudoin, et al. (2011). "Mechanical properties of calcium silicate hydrates." *Materials and Structures*, 44: 13-28.

Allen, A.A., Thomas, J.J., and Jennings, H.M. (2007) "Composition and density of nanoscale calcium-silicate-hydrate in cement/" *Nature Materials*, 6: 311–316.

API, A.P.I. (2009). "Specification for Cements and Materials for Well Cementing." *API Specification 10A*: American Petroleum Institute, Washington, DC.

ASTM, ASTM C1202-07. (2005). "Standard Test Method for Electrical Indication of Concrete's Ability to Resist Chloride Ion Penetration." *ASTM International 2005*: West Conshohocken, PA.

ASTM, ASTM C1437-07. (2005). "Standard Test Method for Flow of Hydraulic Cement." *ASTM International 2005*: West Conshohocken, PA.

ASTM, ASTM C150. (2005). "Standard Specification for Portland Cement." *ASTM 2005*: USA.

ASTM, ASTM C305. (2005). "Standard Practice for Mechanical Mixing of Hydraulic Cement Pastes and Mortars of Plastic Consistency." *ASTM International 2005*: West Conshohocken, PA.

ASTM, ASTM C39/C39M-05. (2005). "Standard Test Method for Compressive Strength of Cylindrical Concrete Specimens." *ASTM International 2005*: West Conshohocken, PA.

Atkins, M., F. Glasser, et al. (1992). "Cement hydrate phases: Solubility at 25C." *Cement and Concrete Research*, 22(1): 6.

Beaudoin, J., and Feldman, R. (1986). "Dependence of degree of silica polymerization and intrinsic mechanical properties of C-S-H on C/S ratio." *8th International Conference on the Chemistry of Cement*. Rio de Jaeiro, Brazil, National Research Council Canada**:** 337-342.

Bell, G.M.M., Benstedm, J., Glasser, F.P., Lachowski, E.E., Roberts, D.R., and Taylor, M.J. (1990). "Study of calcium silicate hydrates by solid state high resolution 29Si nuclear magnetic resonance." *Advancements in Cement Research,* 3**:** 23–37.

Bentur, A., Berger, R.L., Jr., F.V.L., Milestone, N.B., Mindess, S., and Young, J.F. (1979). "Creep and drying shrinkage of calcium silicate pastes: III. A hypothesis of irreversible strains." *Cement and Concrete Research*, 9: 83–96.

Bhushan, B. (2007). *Handbook of Nanotechnology*, Springer.

Brinker, C. J., and Scherer, G.W. (1990). *Sol-Gel Science*. New York, Academic Press.

Cailly, B., Le Thiez, P., Egermann, P., Audibert, A., Vidal-Gilbert, S., and Longaygue, X. (2005). "Geological storage of CO2: A state-of-the-art of injection processes and technologies." *Oil & Gas Science and Technology*, 60(3): 517–525.

Chaipanich A., Nochaiyaa T., Wongkeoa W., and Torkittikul P. (2010). "Compressive strength and microstructure of carbon nanotubes next term–fly ash previous term cement next term composites." *Materials Science and Engineering: A*, 527(4-5): 1063–1067.

Cong, X., and Kirkpatrick, R.J. (1996) "29Si MAS NMR study of the structure of calcium silicate hydrate." *Advanced Cement Based Materials*, 3: 144–156.

Constantinides G., Ulm F. (2007). "The nanogranular nature of C-S-H." *Journal of Mechanics and Physics of Solids*, 55: 64-90.

Crow, W., Carey, J.W., Gasda, S., Williams, D.B., and Celia, M. (2010) "Wellbore integrity analysis of a natural CO_2 producer." *International Journal of Greenhouse Gas Control*, 4(2): 186–197.

Diamond, S. (1976). *Cement paste microstructure--an overview at several levels*. Hydraulic cement pastes; their structure and properties, Tapton Hall, University of Sheffield.

Duguid, A, and Scherer, G.W. (2009). "Degradation of oilwell cement due to exposure to carbonated brine." *International Jounal of Greenhouse Gas Control*, 4: 546-560.

Feldman, R.F., and Sereda, P.J. (1968). "A model for hydrated Portland cement paste as deduced from sorption-length change and mechanical properties." *Matériaux et Construction*, 1(6): 509-520.

Fisher-Cripps, A.C. (2004). "Nanoindentation." *Springer Science+Business Media LLC*., New York, New York.

Garbev, K., Stemmermann, P., Black, L., Breen, C., Yarwood, J., and Gasharova, B. (2007). “Structural features of C–S–H(I) and its carbonation in air- A Raman spectroscopic study. Part I: Fresh phases.” *Journal of American Ceramic Society*, 90(3): 900–907.

Garcia de Lomas, M., Sanchez de Rojas, M.I., and Frias M. (2007). “Pozzolanic reaction of a spent fluid catalytic cracking catalyst in FCC-cement mortars.” *J. of Thermal Anal. and Calorimetry*, 90**:** 443–447.

Grutzeck, M., Benesi, A., and Fanning, B. (1989) “Silicon-29 magic-angle spinning nuclear magnetic resonance study of calcium silicate hydrates.” *American Ceramic Society*, 72: 665–668.

Günther, H. (1995). *NMR Spectroscopy: Basic Principles, Concepts, and Applications in Chemistry*: John Wiley & Sons, Chichester, UK.

Hertz, H. (1881). “On the Contact of Elastic Solids.” *Journal Reine Agnew Math*, 92: 156-171.

Hirljac, J., Wu, J.Q., and Young, J.F. (1983). “Silicate polymerization during the hydration of alite.” *Cement and Concrete Research*, 13: 877–886.

Hitchon, B. (1996). “Acquifer Disposal of Carbon Dioxide.” *Geoscience Publishing Ltd.*: Sherwood Park, Alberta Canada.

Huet, B.M., Prevost, J.H., and Scherer, G.W. (2010) “Quantitative reactive transport modelling of Portland cement in CO_2 saturated water.” *International Journal of Greenhouse Gas Control*, 4(3): 561–574.

Jansson I., Skarp U., and Bigley, C.H. (2007). “The value of colloidal silica for enhanced durability in high fluidity cement based mixes.” *Fifth International Symposium on Self-Compacting Concrete*, Ghent, Belgium.

Jennings, H.M. (2000). "A model for the microstructure of calcium silicate hydrate in cement paste." *Cement and Concrete Research*, 30: 101-116.

Jennings, H.M., and Tennis, P.D. (1994). "Model for the developing microstructure in portland cement pastes." *Journal of the American Ceramic Society*, 77(12): 3161-3172.

Jupe A.C., Wilkinson A.P., Luke K., and Funkhouser, G.P. (2005). “Class H Oil well cement hydration at elevated temperature in the presence of retarding agents: An in situ high-rnergy X-ray diffraction study.” *Industrial Engineering Chemical Research*; 44: 5579–5584.

Justens, H., D. van Loo, et al. (1995). "Chemical shrinkage of oil well cement slurries." *Advancements in Cement Research*, 7(26): 85-90.

Kim, J.J., Fan, T. and Reda, T.M.M. (2010). "Homogenization model examining the effect of nanosilica on concrete strength and stiffness." *Trans. Res. Rec*, 2141**:** 28–35.

Kim, J.J., Griffin, A., Rahman, M.K., and Taha, M.M.R. (2012). "Microstructural composition of oil well cement pastes including nanosilica and cured under high temperature and pressure." *Materials & Design* in Review.

Kim, J.J., Rahman, M.K., Al-Majed, A.A., Al-Zahrani, M.M., and Taha, M.M.R. (2011). "Nanosilica Effects on Composition and Silicate Polymerization in Hardened Cement Paste Cured Under High Temperature and Pressure." *Materials & Design* in Review.

Kim, J.J., Rahman, M.K., Al-Majed, A.A., Al-Zahrani, M.M., Mesfer, M., and Taha, M.M.R. (2013). "Nanosilica Effects on Composition and Silicate Polymerization in Hardened Cement Paste Cured Under High Temperature and Pressure." *Materials & Design* in Review.

Kuo W.-Y., Huang J.-S., and Lin C.-S. (2006). "Effects of organo-modified montmorillonite on strengths and permeability of cement mortars." *Cement and Concrete Research*, 36: 886–895.

Kutchko, B.G., B.R. Strazisar, et al. (2008). "Rate of CO2 attack on hydrated class H Well cement under geologic sequestration conditions." *Environmental Science Journal*, 42: 6237-6242.

Lal K., Meher R.K., Rautela R.S., and Dasgupta, D. (2009). "Pozzolans – Portland Cement: An alternate to API oil well cement." *PetroTech*. New Delhi, India.

Larbi, J.A. (1993). "Microstructure of the Interfacial Zone Around Aggregate Particles in Concrete." *Heron*, 38(1): 1-69.

Lea, F.M. (1970). *The Chemistry of Cement and Concrete*, Arnold Limited.

Li Z., Wang H., He S., Lu Y., and Wang M. (2006). "Investigations on the preparation and mechanical properties of the nano-alumina reinforced cement composite." *Materials Letters*, 60: 356–359.

Lippmaa E., Mägi M., Samoson A., Engelhardt G., and Grimmer A.R. (1980). "Structural studies of silicates by solid-state high-resolution 29Si NMR." *American Chemical Society*, 102: 4889–4893.

Macomber, R.S. (1998). *A Complete Introduction to Modern NMR Spectroscopy*: John Wiley & Sons, New York, NY.

Mehta, P.K., and Monteiro, P.J.M. (2006). *Concrete Microstructure, Properties, and Materials*. McGraw-Hill.

Meller, N., C. Hall, et al. (2007). "Synthesis of cement based CaO-AL2O3-SiO2-H2O (CASH) hydroceramics at 200 and 250 oC: Ex-situ and in-situ diffraction." *Cement & Concrete Composites,* 37: 823-833.

Mondal, P., S.P. Shah, et al. (2010). "Comparative study of the effects of microsilica and nanosilica in concrete." *Journal of the Transportation Research Board:Nanotechnology in Cement and Concrete*, 1(2141): 6-9.

Mondal, P., S.P. Shah, et al. (2008). "Nanoscale characterization of cementitious materials."*ACI Materials Journal*, 105(2): 174-179.

Neville, A.M. (1995). *Properties of Concrete*. Harlow, England, Pearsons/Prentice Hall.

Norris, A., Saafi, M., and Romine, P. (2008). "Temperature and moisture monitoring in concrete structures using embedded nanotechnology/microelectromechanical systems (MEMS) sensors." *Construction & Building Materials*, 22: 111-120.

Oliver, W., Pharr, G. (1992). "An improved technique for determining hardness and elastic modulus using load and displacement sensing indentation experiments." *Journal of Materials Research*, 7(6): 1564-1583.

Powers, T.C., and Brownyard, T.L. (1948). "Studies of the physical properties of hardened Portland cement paste." *PCA Bull*.

Richardson, I.G. (1999). "The Nature of C-S-H in Hardened Cements." *Cement and Concrete Research*, 29(8): 1131-1147.

Roco, M.C. and Alivisatos, W.P. (1999). *Nanotechnology Research Directions: IWGN Workshop Report: Vision for Nanotechnology Research and Development in the Next Decade*, US National Science and Technology Council (NSTC), Committee on Technology (CT), The Interagency Working Group on Nanoscience, Engineering and Technology (IWGN).

Sanchez de Rojas, M.I., and Frias M. (1995). "The influence of silica fume on the heat of hydration of Portland cement", *Fifth CANMET/ACI Intern. Conf. on Fly Ash, Silica Fume, Slag and Natural Pozzolans in Concrete*, Milwaukee, WI, 2: 829.

Sanchez, F. and, Sobolev, K. (2010). "Nanotechnology in concrete - A Review." *Construction and Building Materials,* 24(11): 2060-2071.

Saoût, G.L., Le´colier, E., Rivereau, A., and Zanni, H. (2006). "Chemical structure of cement aged at normal and elevated temperatures and pressures, Part II: Low permeability class G oilwell cement." *Cement and Concrete Research*, 36**:** 428–433.

Saoût, G.L., Le´colier, E., Rivereau, A., and Zanni, H. (2006a). “Chemical structure of cement aged at normal and elevated temperatures and pressures, Part I: Class G oilwell cement.” *Cement and Concrete Research*, 36**:** 71-78.

Saoût, G.L., Le´colier, E., Rivereau, A., and Zanni, H. (2006b). “Chemical structure of cement aged at normal and elevated temperatures and pressures, Part II: Low permeability class G oilwell cement.” *Cement and Concrete Research*, 36**:** 428–433.

Scrivener, K., and Kirkpatrick, R.J. (2008). "Innovation in use and research on cementitious material." *Cement and Concrete Research*, 38: 128-136.

Sugiyama, D. (2008). "Chemical alteration of calcium silicate hydrate (C-S-H) in sodium chloride solution." *Cement and Concrete Research*, 38: 1270-1275.

Taylor, H. (1986). "Proposed structure for calcium silicate hydrate gel." *Journal of the American Ceramic Society*, 69(6): 464-467.

Taylor, H. (1993). "Nanostructure of C-S-H: Current Status." *Advanced Cement Based Materials*, 1: 38-46.

Taylor, H.F.W. (1997). *Cement Chemistry*, London, Thomas Telford Publishing.

Tennis, P.D., and Jennings, H.M. (2000). “A model for two types of calcium silicate hydrate in the microstructure of Portland cement pastes.” *Cement and Concrete Research*, 30: 855–863.

Thomas, J., H. Jennings, et al. (1998). "The surface area of cement paste as measured by neutron-scattering-Evidence for two C-S-H morphologies." *Cement and Concrete Research*, 28(6): 897-905.

Thomas, J.J., and Jennings, H.M. (2006). "A colloidal interpretation of chemical aging of the C-S-H gel and its effects on the properties of cement paste." *Cement and Concrete Research*, 36: 30-38.

Ulm F.-J., Vandamme M., Bobko C., Ortega J.A., Tai K., and Ortiz C. (2007). “Statistical indentation techniques for hydrated nanocomposites: concrete, bone, shale.” *Journal of the American Ceramic Society*, 90(9): 2677–2692.

Velez K., Maximilien S., et al. (2001). “Determination by nanoindentation of elastic modulus and hardness of pure constitutes of Portland cement clinker.” *Cement and Concrete Research*, 31: 555-561.

Wieker, W., Grimmer, A.-R., Winkler, A., Mägi, M., Tarmak, M., and Lippmaa, E. (1982). “Solid-state high-resolution 29Si NMR spectroscopy of synthetic 14Å, 11and 9Å tobermorites.” *Cement and Concrete Research*, 12: 333–339.

Wong, R.C.K., and Yeung, K.C. (2006) "Structural integrity of casing and cement annulus in a thermal well under steam stimulation." *Journal of Canadian Pet. Tech.*, 45(12): 6–9.

Young, J.F. (1988). "Investigations of calcium silicate hydrate structure using silicon-29 nuclear magnetic resonance spectroscopy." *American Ceramic Society*, 71(3): C118–C120.

Zhang, M., and Bachu, S. (2011) "Review of integrity of existing wells in relation to CO2 geological storage: what do we know?" *International Journal of Greenhouse Gas Control*, 5: 825–840.

Zhu W., Hughes J., Bicanic N. and Pearce, C. (2007). "Nanoindentation mapping of mechanical properties of cement paste and natural rocks." *Materials Characterization*, 58 (11–12): 1189–1198.